

A Local Data Assimilation Method (Local DA v1.0) and its Application in a Simulated Typhoon Case

Shizhang Wang¹, Xiaoshi Qiao¹

¹ Nanjing Joint Institute for Atmospheric Sciences, Nanjing, 210000, China

5 Correspondence to: Shizhang Wang (164293231@qq.com)

Abstract. Integrating the hybrid and multiscale analyses and the parallel computation is necessary for current data assimilation schemes. A local data assimilation method, Local DA, is ~~introduced.~~ The proposed designed to fulfill these needs. This algorithm ~~aims to perform hybrid and multiscale analyses simultaneously yet independently for each~~ follows the grid, ~~vertical column or column group and aims to flexibly perform analyses with or without~~ independent framework of the local ensemble ~~perturbations.~~ To achieve these goals, transform Kalman filter (LETKF) and is more flexible in hybrid analysis than the LETKF. Local DA employs an ~~error sample matrix is constructed by~~ explicitly ~~computing the localized~~ computed background error correlation matrix of model variables ~~that are projected onto observation associated grids (e.g., radar velocity) or mapped to observed grid points/columns (e.g., precipitable water vapor).~~ This error sample. This matrix allows Local DA to ~~apply the~~ calculate static covariance with a preset correlation function. It also allows using the conjugate gradient (CG) method to solve the cost function and ~~to perform~~ allows performing localization in ~~the~~ model-variable space, ~~the~~ observation-variable space, or both spaces (double-space localization). ~~To assess the~~ The Local DA performance, ~~a typhoon case is evaluated with a simulated,~~ and a multiscale observation network ~~comprising~~ that includes sounding, wind profiler, precipitable water vapor, and radar ~~data is built; additionally, a~~ observations. In the presence of a small-size time-lagged ensemble ~~is employed.~~ The results show that experiments using the, Local DA can produce a small analysis error by combining multiscale hybrid covariance and double-space localization ~~yield smaller analysis errors than experiments without the static covariance and experiments without double space.~~ The multiscale covariance is computed using error samples decomposed into several scales and independently assigning the localization. ~~Moreover, the hybrid covariance plays a more important role than does localization when a poor time lagged ensemble radius for each scale.~~ Multiscale covariance is used conducive to error reduction, especially at a small scale. The results further indicate that applying the CG method for each local analysis does not result in a discontinuity issue, ~~and the.~~ The wall clock time of Local DA implemented in parallel is halved as the number of cores doubles, indicating a reasonable parallel computational efficiency of Local DA.

1 Introduction

Data assimilation (DA), which estimates the atmospheric state by ingesting information from model predictions, observations, and background error covariances, ~~has been shown to be~~ crucial for the success of numerical weather prediction (Bonavita et al., 2017). Therefore, many previous studies on DA have focused primarily on how to utilize observations and how to estimate background error covariances (e.g., Huang et al., 2021; Wang et al., 2021; Lei et al., 2021; Zhang et al., 2009; Huang et al., 2021; Wang et al., 2021; Lei et al., 2021; Zhang et al., 2009; Brousseau et al., 2011, 2012; Wang et al., 2013; Wang et al., 2012; Kalnay and Yang, 2008; Wang et al., 2013a; Wang et al., 2012; Kalnay and Yang, 2008; Buehner and Shlyueva, 2015). At present, there are two prevailing ~~approaches~~ research orientations of DA: hybrid analysis, which concerns the background error covariance, and multiscale analysis, which often addresses the difference in observation scales.

~~Hybrid analysis was originally proposed to combine the advantages of two kinds of DA methods, namely, stand-alone ensemble-based DA and stand-alone variational DA. The former uses short-term ensemble forecasts as error samples (dynamic samples) to estimate the error covariance (Evensen, 1994), while the latter uses the statistical information extracted from historical forecasts, such as the scale of correlation extracted from the differences between monthly 12- and 24-h forecasts (e.g., the NMC method, Parrish and Derber, 1992). Using both dynamic and static error covariances leverages the advantages of flow-dependent error information and prevents the analysis from degenerating as a result of large sampling errors arising from a limited ensemble size (Wang et al., 2009; Etherton and Bishop, 2004).~~

~~Many approaches are applied to conduct hybrid analyses. A widely used approach is to add an ensemble-associated control variable to a variational DA framework (Lorenc, 2003; Wang et al., 2008). An alternative is to explicitly combine the dynamic and static covariances (Hamill and Snyder, 2000). However, these two approaches are equivalent (Wang et al., 2007). Another method is to average the analyses yielded by the ensemble Kalman filter (EnKF) and the variational method (Bonavita et al., 2017; Penny, 2014). Recently, a hybrid scheme based on the EnKF framework was developed (Lei et al., 2021) that uses a large ensemble size (=800) to simulate the static error covariance. Nevertheless, given the variety of hybrid approaches available, how to conduct hybrid DA is still a matter of debate. In this study, a hybrid scheme is implemented following Hamill and Snyder (2000), though the proposed scheme differs in regard to the details.~~

~~The multiscale DA aims to properly~~ The hybrid analysis aims to utilize both the ensemble and static covariances to leverage the advantages of flow-dependent error information and prevents the analysis from degrading due to a limited ensemble size (Wang et al., 2009; Etherton and Bishop, 2004). A widely used hybrid approach is to add an ensemble-associated control variable to a variational DA framework (Lorenc, 2003; Wang et al., 2008). An alternative combines the ensemble and static covariances (Hamill and Snyder, 2000). These two approaches are equivalent (Wang et al., 2007). Another hybrid method averages the analyses yielded by the ensemble Kalman filter (EnKF) and the variational method (Bonavita et al., 2017; Penny, 2014). Recently, a hybrid scheme based on the EnKF framework was developed (Lei et al., 2021) that uses a large ensemble size (=800) to simulate the static error covariance. Nevertheless, given the variety of hybrid approaches available,

95 how to conduct hybrid DA is still a matter of debate. In this study, a hybrid scheme is implemented following Hamill and Snyder (2000), although the proposed scheme differs regarding the details.

Multiscale DA is designed to utilize observations on a variety of at different scales. A fundamental component of and performs multiscale DA is performing scale-dependent localization: in either the model or observation space. Localization is inevitable due to sampling errors (e.g., distant spurious correlations) in ensemble-based DA, including in hybrid DA (e.g.,

100 Huang et al., 2021; Wang et al., 2021)(e.g., Huang et al., 2021; Wang et al., 2021). There are two ways to localize the covariance, either explicitly or implicitly. The explicit multiscale DA often performs localization in observation space or model observation space. The local ensemble transform Kalman filter (LETKF, Hunt et al., 2007) is the algorithm that performs localization in observation space. In model observation space, the multiscale localization is often done sequentially. Varying the localization radius for observations according to the observation scale or density is a

105 straightforward method; examples include the assimilation of synoptic-scale observations with a large localization radius and then performing radar DA with a small radius of influence (e.g., Zhang et al., 2009; Johnson et al., 2015)(e.g., Zhang et al., 2009; Johnson et al., 2015). In comparison, the implicit method An alternative is done to perform multiscale localization in model variable space, requiring error samples that apply several scalesthe scale decomposition of localization to the ensemble members (Buehner and Shlyayeva, 2015). With the implicit method, The model space localization allows ingesting

110 all observations on different scales can be ingested simultaneously. Recent studies have shown that multiscale DA outperforms DA with fixed localization (Caron and Buehner, 2018; Caron et al., 2019; Huang et al., 2021).

In addition to the analysis quality of the hybrid or multiscale DA analysis, the computational efficiency should also be considered (Bonavita et al., 2017). A highly parallelized DA scheme is preferable due to the continuously increasing model resolution and the number of available observations. One DA scheme that can be highly parallelized is the LETKF

115 algorithm, local ensemble transform Kalman filter (LETKF, Hunt et al., 2007), whose analysis is grid-independent.

In brief, both hybrid DA and multiscale DA are necessary, and the parallel computation efficiency of the LETKF is attractive. Thus, it is desirable to utilize all their advantages. A straightforward idea for achieving the hybrid DA with the LETKF is to use a large-size static ensemble, similar to the EnKF-based hybrid scheme proposed by Lei et al. (2024) Lei et al. (2021). However, due to the limited availability of computational and storage resources, a large static ensemble (≥ 800)

120 is not always feasible, because of the limited computational and storage resources. The LETKF, however, performs the analysis in the ensemble space, which implies that a static ensemble is necessary. In this situation, a grid-independent analysis scheme is needed that can be flexibly run with or without a large static ensemble. Motivated by this necessity, we propose it is desirable to design a flexible DA scheme that follows the grid-independent analysis of the LETKF and can perform both hybrid and multiscale analysis with or without static ensemble members, similar to other variational-based

125 hybrid schemes. The scheme is named Local DA hereinafter hereafter.

Compared with other hybrid schemes, the LETKF, Local DA has two features. First, the proposed scheme constructs an error sample matrix that replaces the ensemble perturbation in the LETKF. To construct this matrix, Local DA explicitly computes the linear combination of columns of a local background error correlation matrix of rather than the combination of ensemble

members. The local background error correlation matrix is in model space, but the model variables that are projected onto the observation associated interpolated to observed grid points/columns. In other words, Local DA works on unstructured grids (for scalar assimilating integrated observations) and/or columns (for observations that measure an integrated quantity of the atmosphere, such as precipitable precipitation water vapor (PWV)). The explicit approach, because vertical localization can be performed in model grid space. Explicitly computing the error correlation matrix requires much more memory than the LETKF, but we will show that allows Local DA to calculate the static background error correlation with a preset correlation function, such as the distant correlation function. Moreover, the computational cost of the matrix is acceptable if observations are appropriately thinned.

Since the error correlation matrix is explicitly constructed, we can determine how to compute the matrix components (in terms of using an ensemble or not) according to the need. Moreover, we can straightforwardly realize the hybrid DA according to the idea of Hamill and Snyder (2000) that Hamill and Snyder (2000). This approach is often utilized with a simple model (Kleist and Ide, 2015; Penny, 2014; Kleist and Ide, 2015; Penny, 2014; Etherton and Bishop, 2004; Lei et al., 2021) because it explicitly computes and directly combines the background error covariance matrices. In this study, we attempt to evaluate the hybrid idea of Hamill and Snyder (2000) in a realistic complicated scenario; this is a secondary goal of this study.

Second, Another feature of Local DA is the ability to perform the multiscale analysis in the model-variable space, the observation-variable space, or in both spaces (double-space localization). In the model-variable space, Local DA adopts a scale-aware localization approach for the multiscale analysis that applies a bandpass filter to create filtered decompose samples and individually performs localization for each waveband. In this approach, the localization radius increases as the wavelength increases, and we attempt to retain the long distance covariances of large scale errors while constraining the small scale covariances within a smaller radius. covariance is considered in current Local DA. A similar idea (i.e., lacking cross-waveband scale covariance) is the scale-dependent localization technique proposed by Buehner (2012). Although the use of cross-waveband scale covariance is likely to further improve the multiscale analysis, but the relative performance depends on ensemble size (Caron et al., 2019). To simplify this study, we leave this issue to be addressed in future work. In contrast, in the observation

Local DA can perform observation-variable space, the localization method is similar to the LETKF. The, which magnifies the observation error as the distance between the observation and model variables increases. For the multiscale analysis in the observation space, the localization radius varies according to increases as the scale of an observation large increases. Compared with radar data, the scale observations are assigned of sounding data is larger so that a large larger radius, while small scale observations are assigned a small radius.

Because model-variable space localization and observation-variable space localization are employed conducted for the background error covariance and observation error covariance, respectively covariances in different spaces, it is possible to perform localization in both spaces localizations synchronously. Although double-space localization may result in a double penalty, it would be interesting to note the localization performances of both hybrid and multiscale DA. Note that the

LETKF of Wang et al. (2021) performance. Note that the LETKF of Wang et al. (2021) can also realize double-space localization, but this application has not yet been investigated.

As the first paper to report on Local DA, this study focuses on the following main issues: i) how to ~~realize both locally~~ conduct the hybrid and multiscale ~~local~~ analysis, ii) the spatial continuity of local analysis, iii) the impact of the hybrid covariance, and multiscale localization on Local DA ~~on the subsequent forecast, and~~ iv) the ~~sensitivity of Local DA to~~ localization (either in the model space or performance of Local DA on cycling DA. Since Local DA is designed to be a more flexible hybrid scheme than LETKF, we do not expect Local DA to outperform LETKF in all scenarios. The comparison of both methods only focuses on i) if they yield similar results in the case of using observation space) localization and to the ensemble size, covariance only and v) comparing ii) if Local DA with the LETKF in terms of single deterministic analysis and forecasting. Updating the hybrid covariance outperforms the LETKF with a poor ensemble perturbation is important for the ensemble forecast and cycling DA, but we plan to investigate this issue in future work. To

Observing system simulation experiments (OSSEs) are adopted to avoid issues associated with the quality control of observations ~~when evaluating the performance of Local DA, we adopt observing system simulation experiments (OSSEs).~~ The simulated multiscale observing system consists of sounding, wind profiler, PWV, and radar (radial velocity and reflectivity) observations ~~on~~; the scales varying of these observations vary from the synoptic scale to the convective scale. A simulated typhoon case is selected for the evaluation.

The remainder of this paper is organized as follows. In Sect. 2, Local DA and its associated multiscale localization technique are described, including the formula, workflow, and other details. Sect. 3 describes the numerical experiments, and Sect. 4 discusses the results. A summary and conclusions are given in Sect. 5.

2 Method

2.1 The Local DA scheme

As mentioned above, Local DA is implemented performs analysis in the LETKF framework and comprises three steps. In the first step, Local DA maps the model state space, but it needs to map model variables to the observation associated grids or onto observed grid points/columns; these variables include before the analysis. All DA methods conduct the mapping, but Local DA updates the mapped model variables. Both the background model state (\mathbf{x}^f) and the ensemble perturbations (\mathbf{X}). The observation prior can be written as $h(\mathbf{H}_i \mathbf{x}^f)$, where \mathbf{H}_i is an operator that interpolates model variables) are mapped according to the observation associated grids or columns \mathbf{H}_i , the vector of interpolation operators. The mapped model state and perturbations are denoted by \mathbf{x}_o^f and h is \mathbf{X}_o , respectively, where the subscript “o” represents the observation operator that converts model variables into observation variables. Similarly, the tangent linear of $h(\mathbf{H}_i \mathbf{x}^f)$ can be written as $\mathbf{H}_o \mathbf{H}_i \mathbf{X}$, where \mathbf{H}_o is the linear operator of h . observed grid points/columns. Note that Local DA only stores \mathbf{x}_o^f and \mathbf{X}_o for a local

analysis rather than the whole forecast domain. An example of the spatial distribution of variables involved in Local DA is shown in Figure 1.

The cost function of Local DA is written in the space of $\mathbf{H}_0\mathbf{x}^f$ and $\mathbf{H}_0\mathbf{X}$. In this space, the size of the local background error correlation matrix is much smaller than that in the model-grid space, which allows us to explicitly compute the correlation matrix as

In the second step, Local DA computes the minimization of the cost function

$$J = \frac{1}{2} \mathbf{v}_o^T \mathbf{v}_o + \frac{1}{2} (\mathbf{H}_0 \hat{\mathbf{X}}_o \mathbf{v}_o - \mathbf{d})^T \mathbf{R}^{-1} (\mathbf{H}_0 \hat{\mathbf{X}}_o \mathbf{v}_o - \mathbf{d}) \quad J = \frac{1}{2} \mathbf{v}_o^T \mathbf{v}_o + \frac{1}{2} (\mathbf{H}_0 \hat{\mathbf{X}}_o \mathbf{v}_o - \mathbf{d})^T \mathbf{R}^{-1} (\mathbf{H}_0 \hat{\mathbf{X}}_o \mathbf{v}_o - \mathbf{d}), \quad (1)$$

where \mathbf{v}_o is the control variable (or a combination of error samples in the LETKF), the observation error covariance is denoted by \mathbf{R} , which is a diagonal matrix in this study, \mathbf{H}_0 is the linear operator of h that converts the model variables into observation variables, and \mathbf{d} is the observation innovation vector. $\hat{\mathbf{X}}_o \hat{\mathbf{X}}_o^T (= \alpha \mathbf{S}_o \mathbf{C}_{oo})$ represents a constructed error-sample matrix, where \mathbf{C}_{oo} is the local background error correlation matrix (its dynamic part is computed using $\mathbf{H}_0\mathbf{X}$, while its static part is computed with a distance correlation function in the current version of Local DA), \mathbf{S}_o stores the standard deviations (STDs) of the model variables, and α is a parameter that adjusts the trace of \mathbf{C}_{oo} . We will discuss \mathbf{C}_{oo} and α later.

In the third step, Local DA computes Once \mathbf{v}_o is obtained, the model state increment \mathbf{x}_m^i on the model grids according to the linear combination can be computed in terms of $\hat{\mathbf{X}}_{mo}$ such that

$$\mathbf{x}_m = \hat{\mathbf{X}}_{mo} \mathbf{v}_o, \quad \mathbf{x}_m^i = \hat{\mathbf{X}}_{mo}^i \mathbf{v}_o, \quad (2)$$

where $\hat{\mathbf{X}}_{mo} = \alpha \mathbf{S}_m \mathbf{C}_{mo}$, $\hat{\mathbf{X}}_{mo}^i = \alpha \mathbf{S}_m^i \mathbf{C}_{mo}^i$, \mathbf{S}_m contains the STDs of the model variables on the model grids, and \mathbf{C}_{mo} is a correlation matrix that contains the correlation coefficients between the model variables in the model-grid space \mathbf{X}_m and those in the $\mathbf{H}_0\mathbf{x}$ space \mathbf{X} . Details regarding \mathbf{C}_{oo} and \mathbf{C}_{mo} will be given later. As long as \mathbf{x}_m^a is obtained, we can perform the deterministic analysis computed in accordance with $\mathbf{x}^a = \mathbf{x}^f + \mathbf{x}_m^a$.

By using the hybrid and localization approaches, the rank of $\hat{\mathbf{X}}_o$ is much higher than that of \mathbf{X} of which the rank is not higher than the ensemble size. Our early test (not shown) indicates that the rank of $\hat{\mathbf{X}}_o$ is a full rank matrix in most cases.

For those rank deficient cases, the rank of $\hat{\mathbf{X}}_o$ is often greater than 97% of the full rank value. The high rank correlation matrix is expected to result in a small analysis error (Huang et al., 2019).

To use Eqs. (1) and (2), several questions need to be answered: i) How do we construct \mathbf{C}_{oo} and \mathbf{C}_{mo} ? ii) How do we calculate α ? iii) How do we solve Eq. (1) to obtain \mathbf{v}_o ? iv) How do we deal with nonlinear observation operators? To update ensemble perturbations, the current version of Local DA adopts the stochastic method (Houtekamer and Mitchell, 1998) that treats observations as random variables. This method adds random perturbations with zero mean to \mathbf{d} in Eq. (1). For an M -member ensemble, equations (1) and (2) are conducted M times to update members with perturbed observations, similar to the procedure of Li et al. (2012). These analyses share the same background error covariance but use different observations.

280 [The stochastic approach was reported to be less accurate than the deterministic approach \(e.g., Whitaker and Hamill, 2002\) because it introduces additional sampling error. At this stage, Local DA mainly concerns the deterministic analysis; further improvement of the analysis ensemble is left in future work.](#)
[Compared with the LETKF or the En4DVar of Liu et al. \(2008\), Local DA seeks the combination \(\$\mathbf{v}_0\$ \) in model space, or more specifically, the combination of the columns of a local background error correlation matrix of model variables, rather](#)
 285 [than the combination in ensemble space. Thus how to construct \$\mathbf{C}_{oo}\$ and \$\mathbf{C}_{mo}\$ is key for Local DA. Explicitly computing \$\mathbf{C}_{oo}\$ raises the question of how to solve the cost function of Local DA in the case of large-size \$\mathbf{C}_{oo}\$. In addition, how to deal with nonlinear observation operators should be determined.](#) The subsequent subsections present the answers to these questions.

2.1.1 The local background error correlation matrix

In Local DA, the actual correlation matrix $\tilde{\mathbf{C}}$ is the square of \mathbf{C}_{oo} multiplied by a rescaling parameter α^2 :

$$290 \quad \tilde{\mathbf{C}} = \alpha^2 \mathbf{C}_{oo} \mathbf{C}_{oo}^T. \quad (3)$$

By using the rescaling parameter, the trace of $\tilde{\mathbf{C}}$ is equivalent to that of \mathbf{C}_{oo} . α is computed according to

$$\alpha = \sqrt{\frac{tr(\mathbf{C}_{oo})}{tr(\mathbf{C}_{oo} \mathbf{C}_{oo}^T)}}, \quad (4)$$

where $tr(\cdot)$ denotes the calculation of the trace of a matrix. Notably, $tr(\mathbf{C}_{oo} \mathbf{C}_{oo}^T)$ is equal to the sum of squares of all elements in \mathbf{C}_{oo} . There is no need to compute $\mathbf{C}_{oo} \mathbf{C}_{oo}^T$. $\tilde{\mathbf{C}}$ and \mathbf{C}_{oo} are identical in terms of [Eigenvectors](#) and the
 295 trace of the matrix (total variance). The eigenvalues of $\tilde{\mathbf{C}}$ are the squares of the corresponding [Eigenvalues](#) of \mathbf{C}_{oo} multiplied by α^2 . Therefore, $\tilde{\mathbf{C}}$ is an approximation of \mathbf{C}_{oo} . [Storto and Andriopoulos \(2021\)](#) proposed a hybrid DA scheme that also used the rescaling parameter to tune the trace of a matrix (see their Eq. (15)), but they constructed the background error covariance in a way differing from ours.

\mathbf{C}_{oo} is a $K \times K$ matrix, where K is the number of model variables associated with the [operators of all ambient observations to be assimilated](#). K is computed according to

$$300 \quad K = \sum_{i=1}^{N_t} (N_o(i) N_{op}(i)), \quad K = \sum_{i=1}^{N_t} [N_o(i) N_{op}(i)], \quad (5)$$

where N_t is the number of observation types, such as the zonal wind from soundings and/or the radial velocity from radars, $N_o(i)$ is the number of observations of the i th type, and $N_{op}(i)$ is the number of [analysis model](#) variables used [in by](#) the observation operator of the i th type. [For instance, if radar reflectivity is the only available observation type and there are 100 observations, \$K\$ is equal to 300 \(\$100 \times 3\$ \) in the case of using the observation operator of Gao and Stensrud \(2012\) because the operator requires three hydrometeors \(\$q_r\$, \$q_s\$, and \$q_e\$ \).](#) Now we are going to give an example of \mathbf{C}_{oo} . Assuming there are

three available observations (two zonal wind observations and a surface pressure observation), the background error correlation matrix is

$$\mathbf{C}_{oo} = \begin{pmatrix} c_{u1u1} & c_{u1u2} & c_{u1ps1} \\ c_{u2u1} & c_{u2u2} & c_{u2ps1} \\ c_{ps1u1} & c_{ps1u2} & c_{ps1ps1} \end{pmatrix}, \quad \mathbf{C}_{oo} = \begin{pmatrix} c_{u1u1} & c_{u1u2} & c_{u1ps1} \\ c_{u2u1} & c_{u2u2} & c_{u2ps1} \\ c_{ps1u1} & c_{ps1u2} & c_{ps1ps1} \end{pmatrix}, \quad (6)$$

where c is the correlation coefficient between the model variables projected onto observation-associated grids in the space of \mathbf{X}_o and the subscripts “ $u1$ ”, “ $u2$ ”, and “ $ps1$ ” represent the two zonal wind observations and the surface pressure observation, respectively. If the model variables to be updated are the zonal wind (u), potential temperature (θ), and water vapor mixing ratio (q) located where observation “ $u1$ ” is, the corresponding \mathbf{C}_{mo} is Correspondingly, the STD matrix \mathbf{S}_o can be written as

$$\mathbf{C}_{mo} = \begin{pmatrix} c_{\theta1u1} & c_{\theta1u2} & c_{\theta1ps1} \\ c_{q1u1} & c_{q1u2} & c_{q1ps1} \\ c_{u1u1} & c_{u1u2} & c_{u1ps1} \end{pmatrix}, \quad \mathbf{S}_o = \begin{pmatrix} s_{u1} \\ s_{u2} \\ s_{ps1} \end{pmatrix}, \quad (7)$$

where the subscripts “ $\theta1$ ” and “ $q1$ ” indicate that variables are on the same grid as observation “ $u1$ ”. For \mathbf{C}_{oo} , the corresponding \mathbf{S}_o is

$$\mathbf{S}_o = \begin{pmatrix} s_{u1} \\ s_{u2} \\ s_{ps1} \end{pmatrix}, \quad \text{where } s \text{ denotes the STDs of the model variables projected onto the observed grids. } \mathbf{S}_o \text{ is a } K \times K$$

matrix, but a $K \times 1$ array is sufficient to store \mathbf{S}_o . After \mathbf{C}_{oo} and \mathbf{S}_o are formed, \mathbf{v}_o can be solved. In this example, \mathbf{v}_o is in the following form:

$$\mathbf{v}_o = \begin{pmatrix} v_{u1} & v_{u2} & v_{ps1} \end{pmatrix}^T, \quad (8)$$

where s denotes subscripts “ $u1$ ”, “ $u2$ ”, and “ $ps1$ ” have the STDs of same meaning in Eqs. (6) and (7).

To obtain the model state increment \mathbf{x}^i , it is necessary to form \mathbf{C}_{mo} and the corresponding \mathbf{S}_m . If the model variables projected onto observation associated grids. \mathbf{S}_m contains the STDs to be updated are the zonal wind ($v1$), potential temperature ($\theta1$), and water vapor mixing ratio ($q1$), \mathbf{C}_{mo} is written as

$$\mathbf{C}_{mo} = \begin{pmatrix} c_{\theta1u1} & c_{\theta1u2} & c_{\theta1ps1} \\ c_{q1u1} & c_{q1u2} & c_{q1ps1} \\ c_{v1u1} & c_{v1u2} & c_{v1ps1} \end{pmatrix}, \quad (9)$$

where subscripts “ $u1$ ”, “ $u2$ ”, and “ $ps1$ ” are the same as those in Eqs. (6) and (7), while subscripts “ $v1$ ”, “ $\theta1$ ”, and “ $q1$ ” denote the model variables to be updated. \mathbf{C}_{mo} comprises the error correlation coefficients between \mathbf{X} and \mathbf{X}_o . The size of \mathbf{C}_{mo} is $N_m K$ which depends on the model grids, which are s_{u1} , number (N_m) of model variables to be updated. However, there is no need to store full \mathbf{C}_{mo} in practice because one row of \mathbf{C}_{mo} is needed to update the corresponding model variable. \mathbf{S}_m is the STD matrix of model variables, containing s_{v1} , $s_{\theta1}$, and s_{q1} for the aforementioned in this example. For convenience, a summary of the dimensions of variables involved in Local DA is listed in Table 1.

Note that the variational DA methods seek the combination of the columns of the square root of the background error covariance matrix, while Local DA combines the columns of the error correlation matrix. It is based on the consideration of computational cost because it is expensive to obtain the square root of \mathbf{C}_{oo} if the size of \mathbf{C}_{oo} is large. Moreover, modeling the square root of the background error covariance matrix, as many variational DA methods do, is also difficult for Local DA because the irregular distribution of observations makes it infeasible to utilize a recursive filter.

Additionally, note that the size of \mathbf{C}_{oo} grows rapidly as K increases. However, given that \mathbf{C}_{oe} is used for the local analysis. However, the memory requirement is still affordable, since \mathbf{C}_{oo} is only used for local analysis. For high-resolution observations, thinning can help reduce the cost, which is also necessary to ensure that the observation errors are uncorrelated (e.g., Hoeflinger et al., 2001)(e.g., Hoeflinger et al., 2001). For observations at the same place that are associated with the We use the same model variables, such as for the data observing the same grid point/column. For example, the same hydrometeor variables (q_r , q_s , and q_g) are used to compute the radar reflectivity and differential reflectivity, the same \mathbf{C}_{oe} components are used, at the same observed grid point. In this situation, the size of \mathbf{C}_{oo} does not increase with the observations. This strategy is also valid for passive microwave observations at different frequencies obtained by one satellite, because they observe the same column of the atmosphere. Therefore, the size of \mathbf{C}_{oo} is controllable. In this study, we use a simple thinning approach to control the matrix size in this study, as described in the Appendix.

2.1.2 The solution of Local DA

365 There are two ~~approaches~~ methods to solve the gradient of Eq. (1): i) matrix decomposition and ii) an iterative algorithm. The first approach is straightforward, but ~~it~~ is time-consuming and sometimes infeasible if the C_{oo} size is large. Therefore, Local DA adopts an iterative algorithm, namely, the conjugate gradient (CG) method ~~(Shewchuk, 1994)~~ (Shewchuk, 1994). Theoretically, using the CG method requires the background error covariance matrix to be positive definite. However, with the control variable transform, a positive semidefinite covariance matrix is sufficient to obtain the best linear unbiased estimate ~~(Ménardier and Auligné 2015)~~ (Ménardier and Auligné 2015). A strictly diagonally dominant matrix with nonnegative diagonal elements ~~s~~ is positive semidefinite. Performing Although a positive semidefinite covariance localization matrix is a way to generate sufficient, using a higher-rank background error covariance matrix helps obtain a lower analysis error (Huang et al., 2019). Compared with the matrix rank of $\hat{\mathbf{X}}_o$, which is not higher than the ensemble size, that of $\hat{\mathbf{X}}_o$ is much higher after C_{oo} is localized. Our early test (not shown) indicates that $\hat{\mathbf{X}}_o$ is a full rank matrix in most cases. For rank-deficient cases, the rank of $\hat{\mathbf{X}}_o$ is often greater than 97% of the full rank value. The details of this localization will be given later.

Note that Local DA performs the CG step locally, unlike other variational-based DA methods that apply the CG method globally. Therefore, it is necessary to investigate whether the local application of the CG method causes a nonnegligible spatial discontinuity, which will be discussed in Sect. 4. For computational efficiency, the maximum number of iterations is 380 100. If the error tolerance ε^2 defined in ~~(Shewchuk, 1994)~~ (Shewchuk, 1994) cannot reach 1×10^{-6} by the 100th step, the CG method is stopped.

2.1.3 The observation operator

The EnKF algorithm often approximates the linear projection ~~(\mathbf{H} in Eq. (1)) of the model variables onto the observation variables)~~, according to the departure of the observation priors from their ensemble mean. It is straightforward for Local DA 385 to use the ensemble approximation approach. However, for nonlinear observation operators, there is an alternative ~~to the ensemble mean~~, namely, the observation prior calculated by using the ensemble mean of the model variables. ~~Tang et al. (2014)~~ Tang et al. (2014) demonstrated that this alternative could lead to better results. Furthermore, ~~Yang et al. (2015)~~ Yang et al. (2015) examined the application of this alternative in radar DA and showed that the alternative approach produced smaller lower analysis errors for the model variables associated with radial velocity (three wind components) and reflectivity 390 (mixing ratios of rain, snow, and graupel). Given that remote sensing observations such as those obtained by radars and satellites are important parts of any multiscale observation network, Local DA adopts the alternative approach proposed by Tang et al. (2014) Tang et al. (2014).

Local DA approximates the linear projection $\tilde{\mathbf{Y}} = \mathbf{H}_o \hat{\mathbf{X}}_o$ $\tilde{\mathbf{Y}} = \mathbf{H}_o \hat{\mathbf{X}}_o$ according to

$$\tilde{\mathbf{Y}} \approx h(\mathbf{x}^f + \hat{\mathbf{X}}_o) - h(\mathbf{x}^f + \overline{\hat{\mathbf{X}}_o}), \quad (9)$$

$$\tilde{\mathbf{Y}} \approx h(\mathbf{x}^f + \hat{\mathbf{X}}_o) - h(\mathbf{x}^f + \overline{\hat{\mathbf{X}}_o}), \quad (10)$$

where h is the nonlinear observation operator and \mathbf{x}^f is the background model state vector. Note that Eq. (9) is written for a deterministic forecast in this study. Compared with the results using the ensemble mean of observation priors, Eq. (9) reduces the analysis error of reflectivity by approximately 2 dBZ in our early test (not shown). This result is consistent with that of Yang et al. (2015).

2.2 The multiscale localization analysis

To realize multiscale localization in model space, Local DA first performs scale decomposition with a bandpass filter. The decomposed perturbation, \mathbf{X}'_b , is

$$\mathbf{X}'_b = \sum_{l=1}^{N_b} \mathbf{X}_b^l, \quad (11)$$

where the superscript “ l ” represents the l th waveband scale and N_b is the number of bands. As a localization approach lacking cross-waveband scale covariance, Local DA computes the STD of the perturbation, s , according to

$$s(i) = \sqrt{\sum_{l=1}^{N_b} \frac{1}{N} \sum_{m=1}^N [\mathbf{X}_b^l(i, m)]^2}, \quad (12)$$

where i and m denote the i th model variable and the m th sample, respectively, and N is the sample size. Compared with the

raw STD, $\sqrt{\frac{1}{N} \sum_{m=1}^N \left[\sum_{l=1}^{N_b} \mathbf{X}_b^l(i, m) \right]^2}$, the cross influence among different scales of \mathbf{X}'_b is ignored in Eq. (12).

Nevertheless, we acknowledge the importance of the cross influence of these perturbations and plan to investigate this issue with regard to Local DA in our future work.

The multiscale correlation coefficient $c(i, j)$ is calculated according to

$$c(i, j) = \sum_{l=1}^{N_b} \frac{\text{cov}[\mathbf{X}_b^l(i), \mathbf{X}_b^l(j)]}{s(i)s(j)}, \quad (13)$$

where i and j denote the i th and j th variables, respectively. For the case of $i=j$, Eq. (13) ensures $c(i, j)=1.0$.

We perform localization for each waveband scale independently to construct the multiscale correlation matrix. In principle, our multiscale localization method trusts the correlation coefficient of each waveband scale when the distance between two variables is smaller than the lower bound of the waveband scale. For instance, for the waveband scale of 50 km – 100 km, Local DA starts the localization when the distance d is greater than 50 km. The decorrelation coefficient $r(l, i, j)$ for the l th waveband scale and $c(i, j)$ is calculated according to

$$\begin{cases} r(l, i, j) = 1.0, & d \leq d_{\min}(l) \\ r(l, i, j) = e^{-8 \left[\frac{d - d_{\min}(l)}{d_l(l)} \right]^2}, & d > d_{\min}(l) \\ r(l, i, j) = 0.0, & d > d_{\max}(l) \end{cases} \quad (43) \quad (14)$$

420 where $d_{\min}(l)$ and $d_{\max}(l)$ are the lower and upper bounds of the l th waveband-scale, respectively, and $d_l(l)$ is the localization radius for the l th waveband-scale. Note that how to optimally localize the background error covariance is still an open question; rather, Eq. (43) is simply a preliminary implementation of multiscale localization for Local DA.

In addition to Substituting equations (13) and (14) into equation (6), an example of \mathbf{C}_{oo} in equation (6) is written as:

$$\mathbf{C}_{oo} = \begin{pmatrix} \sum_{l=1}^{N_b} r(l, u1, u1) \frac{\text{cov}[\mathbf{X}_b^l(u1), \mathbf{X}_b^l(u1)]}{s(u1)s(u1)} & \dots & \dots \\ \sum_{l=1}^{N_b} r(l, u2, u1) \frac{\text{cov}[\mathbf{X}_b^l(u2), \mathbf{X}_b^l(u1)]}{s(u2)s(u1)} & \dots & \dots \\ \sum_{l=1}^{N_b} r(l, ps1, u1) \frac{\text{cov}[\mathbf{X}_b^l(ps1), \mathbf{X}_b^l(u1)]}{s(ps1)s(u1)} & \dots & \dots \end{pmatrix} \quad (15)$$

425 where i and j in equation (13) are replaced by subscripts in equation (6). For brevity, only the first column of \mathbf{C}_{oo} is listed. Obviously, applying multiscale localization in the does not change the size of \mathbf{C}_{oo} . Correspondingly, an example of \mathbf{C}_{mo} in equation (8) can be written as:

$$\mathbf{C}_{mo} = \begin{pmatrix} \sum_{l=1}^{N_b} r(l, v1, u1) \frac{\text{cov}[\mathbf{X}_b^l(v1), \mathbf{X}_b^l(u1)]}{s(v1)s(u1)} & \dots & \dots \\ \sum_{l=1}^{N_b} r(l, \theta1, u1) \frac{\text{cov}[\mathbf{X}_b^l(\theta1), \mathbf{X}_b^l(u1)]}{s(\theta1)s(u1)} & \dots & \dots \\ \sum_{l=1}^{N_b} r(l, q1, u2) \frac{\text{cov}[\mathbf{X}_b^l(q1), \mathbf{X}_b^l(u1)]}{s(q1)s(u1)} & \dots & \dots \end{pmatrix} \quad (16)$$

430 Because the sizes of \mathbf{C}_{oo} and \mathbf{C}_{mo} do not change, there is no modification for \mathbf{v}_o , \mathbf{x}^i , \mathbf{x}^f , and \mathbf{x}^a . The only modification to realize multiscale localization in model-variable space is to store the error sample of each scale and compute the corresponding correlation coefficient. Therefore, realizing multiscale analysis within the Local DA framework is easy.

The multiscale localization proposed in this subsection gradually diminishes the contribution of small-scale covariance as the distance between two variables increases while retaining that of large-scale covariance until the distance is very large. Table 2 shows an example of multiscale localization. In this example, there are two arbitrary variables of which the error samples are decomposed into three scales. The values of covariance between the two variables are C_1 , C_2 , and C_3 at three scales.

435

When the two variables are close (8 km), the localization coefficients of C_2 and C_3 are 1.0, according to the first formula in equation (14). As the distance increases to 300 km, the localization coefficients of C_1 and C_2 become nearly zero, and the total covariance is mainly attributable to C_3 .

In addition to multiscale localization in the model space, Local DA can perform localization in the observation-variable space, similar to the LETKF. Observation-space localization is conducted by enlarging the observation error as the distance between variables increases. The localization coefficient in the observation space is calculated according to the second formula of Eq. (4314), but $d-d_{\min}(l)$ and $d_{\min}(l)$ are replaced by d and d_o , respectively, where d_o is the localization radius that varies among different observation types. In practice, it is possible for C_{oo} to be zero. Because C_{oo} and R are independently localized, Local DA can perform localization in both the model space and the observation space synchronously. Although performing localization in both spaces may result in a double penalty, it would be interesting to note the performance of the double-space localization approach, which has not yet been investigated. The related experiments and results are given in the following sections.

2.3 The hybrid analysis covariance

The current version of Local DA calculates a simple “static” correlation matrix by using the second formula of Eq. (4314), except that $d-d_{\min}(l)$ and $d_{\min}(l)$ are replaced by d and d_s , respectively, where d_s is a fixed localization preset radius. For the i th and j th variables, the hybrid correlation coefficient $c(i,j)$ in C_{oo} is computed according to

$$c(i, j) = \gamma \sum_{l=1}^{N_b} r(l, i, j) \frac{\text{cov}[\mathbf{X}_b^l(i), \mathbf{X}_b^l(j)]}{s(i)s(j)} + (1 - \gamma) e^{-8 \left[\frac{d}{d_s} \right]^2}, \quad (4417)$$

where γ is the weight of the dynamic correlation. The hybrid $c(i,j)$ in C_{mo} is also computed according to Eq. (4417), but $\mathbf{X}_b^l(i)$ and $s(i)$ store represent the variables-variable at a the model grid point. In the case where the i th and j th variables are different types of variables, such as a wind component variable and a temperature variable, the second term on the right hand side of Eq. (14) is forced to zero. In other words, the current version of Local DA suppresses the cross-variable covariance when the hybrid analysis is performed. To prevent $s(i)$ and $s(j)$ in Eq. (4417) from being forced to zero (as which often occurs for convective-related variables such as the mixing ratios of rainwater, snow, and graupel), we add small, random perturbations with an STD of 1×10^{-7} to the variables for which the STDs are smaller than 1×10^{-7} .

Note that the static part of equation (17) represents merely a distant correlation. It is valid for the univariate correlation rather than the cross-variable scenario. Therefore, the static part of equation (17) is forced to zero if the i th and j th variables are different types of variables. In other words, the cross-variable correlation is contributed only by the ensemble part. The authors acknowledge that the cross-variable correlation is important for DA, but the static cross-variable correlation must be carefully modeled, such as the correlation between wind components and geopotential height, or between the stream function and potential temperature. The modeling work is in progress.

2.4 The workflow of Local DA

Here, we present a step-by-step description of how the hybrid and multiscale analyses described in the previous sections are performed for all the model variables. ~~Note that~~ There is a way for Local DA ~~can to~~ perform the analysis in a much faster way; we will discuss this method later.

- 1) Apply a bandpass filter to ~~generate filtered samples on~~ \mathbf{X}'_b into N_b scales ~~from~~ \mathbf{X}'_b .
- 2) Store the initial condition, ~~filtered perturbation~~ \mathbf{X}'_b samples, and observations in separate arrays denoted by \mathbf{x}^f , \mathbf{X}'_b , and \mathbf{y}^o , respectively.
- 3) For each model variable to be updated, search its ambient observations according to their scales and store these observations in array $\hat{\mathbf{y}}^o$; for example, search for sounding data within 300 km while searching for radar data within 15 km. In addition, according to the observation operators of $\hat{\mathbf{y}}^o$, store the observation-associated model variables that have been projected onto ~~observation associated~~ $\hat{\mathbf{x}}^f$ grids or columns into arrays denoted $\hat{\mathbf{x}}^f$ and $\hat{\mathbf{X}}'_b$, respectively.
- 4) Calculate the vector \mathbf{d} in Eq. (1) with $\hat{\mathbf{y}}^o$ and $\hat{\mathbf{x}}^f$.
- 5) Use $\hat{\mathbf{X}}'_b$ to generate \mathbf{S}_o , \mathbf{C}_{oo} , \mathbf{S}_m , and \mathbf{C}_{mo} according to Eqs. (44), (43), (15), and (44).
- 6) Compute α for \mathbf{C}_{oo} by using Eq. (4).
- 7) Compute $\hat{\mathbf{X}}_o = \alpha \mathbf{S}_o \mathbf{C}_{oo} \hat{\mathbf{X}}_o = \alpha \mathbf{S}_o \mathbf{C}_{oo}$.
- 8) Calculate $\mathbf{Y} = \mathbf{R}^{-0.5} \mathbf{H}_o \hat{\mathbf{X}}_o$ by using Eq. (9).
- 9) Use the CG method to solve $(\mathbf{I} + \mathbf{Y}^T \mathbf{Y}) \mathbf{v}_o = \mathbf{Y}^T \mathbf{R}^{-0.5} \mathbf{d}$ and obtain \mathbf{v}_o .
- 10) Compute the model state increment \mathbf{x}_m according to Eq. (2).

In step 1), there are many ways to realize the bandpass filter. In this study, the difference between two low-pass analyses defines the bandpass field (Maddox, 1980), where the low-pass filter is the Gaussian filter. An example of a bandpass field is shown in Figure 2. For convenience, the radius of the Gaussian filter is used to represent the scale in this study. For the scale of 0 km - 20 km (Figure 2a), the small-scale feature prevails and corresponds to convection in the simulated typhoon. As the radius increases (Figure 2b), larger-scale information is extracted. A large-scale anticyclonic shear is observed when the radius is greater than 200 km (Figure 2c). The results (Figure 2d-f) also show that the contribution of the small-scale ensemble spread is often less than 10% out of the convective area, while in most areas of the forecast domain, the contribution of the large-scale (> 200 km) spread is greater than 20%.

Steps 5) to 9) contribute the most to the computational cost of Local DA. Computing C_{oo} requires MK^2 operations, which is not less than N_o^2 , where M represents the size of the ensemble, and N_o denotes the number of observations to be assimilated. Step 7) requires $2K^2$ operations. To calculate step 8), N_oK^2 operations are needed. For each iteration step of the CG method, the number of operations is slightly larger than $2N_oK$. N_i iteration steps require $2N_iN_oK$ operations.

As mentioned above, Step 9) can also be solved through eigenvalue decomposition as the LETKF does. However, \mathbf{Y} in Local DA has more columns than the LETKF. In the LETKF, \mathbf{Y} has M columns, while the corresponding value is K in Local DA. Therefore, Local DA has to deal with a K by K matrix, while the LETKF only needs to solve an M by M matrix. M is often smaller than 10^2 , thus, $\mathbf{I} + \mathbf{Y}^T \mathbf{Y}$ can be handled efficiently by eigenvalue decomposition. In contrast, K could be 10^3 or higher, thus, the CG method is more suitable.

Despite the large amount mentioned above, we do not have to do that many operations in practice. For example, step 8) requires just N_o^2 operations if only scalar observations are available. Notably, for a 3-D domain containing N_g grid points and N_v variables, the total number of operations will be as N_gN_v times that of one local analysis. However, it is possible to reduce the cost.

Considering that \mathbf{S}_m , \mathbf{C}_{mo2} and \mathbf{x}_m can be applied to all variables influenced by $\hat{\mathbf{y}}^o$, it is not necessary to compute \mathbf{C}_{oo} for each model variable. ~~In the current version of Local DA~~ Moreover, \mathbf{S}_m , \mathbf{C}_{mo2} and \mathbf{x}_m may contain all the model variables at a model grid point, in more than one vertical column, or in 5 neighboring columns (N -column analysis). ~~For~~ The total number of operations in an N -column analysis, ~~$\hat{\mathbf{y}}^o$ contains ambient observations at all vertical~~ is reduced to $N_g/(NN_z)$ times as one local analysis, where N_z is the number of levels in one column. Due to using the same \mathbf{C}_{oo} for neighboring columns, the $5N$ -column analysis is slightly rasterized (not shown), leading to slightly larger/higher errors than the 1-column analysis. However, the extent of this degeneration is acceptable. ~~On the other hand, the~~ as long as N is not too large (<9). The wall clock time of the $5N$ -column analysis is close to $1/5$ of that N of the 1-column analysis. ~~In this study, all~~ All Local DA results are generated using a 5-column analysis in this study. A similar N -column analysis approach is the weighted interpolation technique in the LETKF (Yang et al., 2009) (Yang et al., 2009), which performs the LETKF analysis, ~~for example,~~ every 3 grid points in both the zonal direction and the meridional direction.

3 Experimental design

3.1 The simulated typhoon

The third typhoon of the 2021 western Pacific season, In-Fa, is selected for the OSSEs performed herein. The true simulation, starting at 00 UTC on 25 July 2021 and ending at 18 UTC on 26 July 2021, simulates the stage in which In-Fa approaches China. The Weather Research and Forecast (WRF, Skamarock et al., 2018) (WRF, Skamarock et al., 2018) model V3.9.1 is used for the simulation. The central latitude and longitude of the forecast domain are 30.5° and 122.0° , respectively. The size of the domain size is 201 grids \times 201 grids \times 34 levels with a horizontal resolution of 5 km and a model

top pressure of 50 hPa. The physical parameterization schemes are as follows. The WRF single-moment 6-class ice scheme (Hong and Lim, 2006) is adopted for microphysical processes. For longwave and shortwave radiation, the rapid radiative transfer model (RRTM) scheme (~~Mlawer et al., 1997~~)(Mlawer et al., 1997) and ~~the~~ Dudhia scheme (Dudhia, 1989), respectively, are used. The Yonsei University (YSU) scheme (Hong et al., 2006) is employed for the planetary boundary layer simulation. For the cumulus parameterization, the Kain–Fritsch (new Eta) scheme (~~Kain, 2004~~)(Kain, 2004) is enabled. The unified Noah land surface model is used to simulate the land surface. We adopt the global forecast system (GFS) analysis at 00 UTC on 25 July 2021 as the initial condition of the ~~true~~Truth simulation.

3.2 The multiscale observation network

~~The~~ According to Hoffman and Atlas (2016), a criterion for reasonable OSSEs is that true simulation agrees with the real atmosphere. The typhoon central pressure in the Truth simulation gradually increases from 968 hPa to 980 hPa by 18 UTC on 26 July 2021 (not shown), which is consistent with the real observation obtained from the China Meteorological Administration (CMA), except that the observed pressure increases more rapidly, reaching 985 hPa by 18 UTC on 26 July 2021. The simulated typhoon’s central location also agrees with the CMA observation. Therefore, the Truth simulation is eligible for OSSEs.

3.2 Multiscale observation network

The simulated multiscale observation network (~~Figure 3~~Figure 13) comprises ~~simulated~~ sounding, wind profiler, PWV, and radar ~~data~~ observations. Soundings are available at 00 UTC and 12 UTC on 26 July 2021, whereas the other types of observations are available hourly on 26 July 2021.

For each sounding, we simply extract the perturbed model variables, u , v , θ , and q_v , every 2 model levels as the observations. The simulated soundings also ~~include records of record~~ the perturbed surface pressure, ps . The sounding perturbations follow a Gaussian distribution with zero mean. The perturbation STDs are 0.5 m s^{-1} , 5 m s^{-1} , 0.5 K , $5 \times 10^{-5} \text{ kg kg}^{-1}$, and 10 Pa for u , v , θ , q_v , and ps , respectively. To better reflect ~~the~~ reality, no simulated soundings are available over the ocean, and the horizontal resolution of each sounding is 100 km.

The simulated wind profiler provides data on horizontal wind components, u and v , at all model levels. The perturbations added to the wind profiler data follow a Gaussian distribution with zero mean and an STD of 0.5 m s^{-1} . The wind profilers, the data from which have a horizontal resolution of 50 km, provide data only on land.

The PWV observations are computed according to

$$PWV = \frac{1}{g} \int_{p1}^{p2} q_v dp, \quad (4518)$$

where g is the gravitational constant of acceleration and $p1$ and $p2$ represent the bottom and top of a model column, respectively. Perturbations with zero mean and an STD of 0.5 kg m^{-2} are added to the PWV observations. Because the PWV

is observed by satellites, this type of observation is available for the whole forecast domain, and the horizontal observation interval is 50 km in both the x and ~~the~~ y directions.

~~The radar data to be assimilated are radial velocity and reflectivity measurements. We adopt Eq. (3) of Xiao and Sun (2007)~~The radar data to be assimilated are radial velocity and reflectivity. We adopt Eq. (3) of Xiao and Sun (2007) to compute the radial velocity, but we ignore the terminal velocity in ~~the OSSE. For reflectivity, the operator proposed by Gao and Stensrud (2012)~~OSSEs. For reflectivity, the operator proposed by Gao and Stensrud (2012) is employed. Three radars located ~~at~~ approximately ~~at~~ Shanghai (121.48 ° E, 31.23 N), Hangzhou (120.16 ° E, 30.28 N), and Ningbo (121.55 ° E, 29.88 N) are simulated with a maximum observation range of 230 km. The simulated radars work on the volume coverage pattern (VCP) 11 mode, which has 14 elevation levels from 0.5 ° to 19.5 °. Radar data are created on volume-scan elevations, but they are on model grids in the horizontal direction, as shown in ~~Xue et al. (2006)~~Xue et al. (2006). The radial velocity and reflectivity observation errors are 1.0 m s⁻¹ and 2.0 dBZ, respectively. The horizontal resolution of the radar data is identical to the model grid spacing.

In total, 2795 simulated soundings, 400 PWV data points, 5332 wind profiler observations, and 391618 radar observations (including radial velocity and reflectivity) are utilized in this study.

3.3 ~~The~~ DA experiments

In this study, ~~we design several~~two sets of experiments ~~for Local DA to investigate its performance in~~are designed. The first set of experiments consists of single deterministic analyses and ~~is used~~ to examine the ~~impacts~~impact of the hybrid ~~and covariance, the~~ multiscale ~~analysis approaches. We also run~~localization in model space, and the double-space localization. The other set of experiments comprises several cycling ~~DA experiments for Local DA, but the results of these cycling experiments are used only for reference because the current version of Local DA does not update~~analyses, mainly focusing on the ~~ensemble perturbations and does not seriously consider the cross-variable analysis~~balance during/after the (in terms of surface pressure tendency) and the impact of Local DA on cycling analysis, ~~which are important for cycling DA experiments (e.g., Zeng et al., 2021).~~ To perform the ~~hybrid~~analysis ~~with ensemble covariance~~, it is necessary to generate the ensemble first. Therefore, in this subsection, we first describe the ~~generation of the~~ ensemble and then introduce the experimental design.

3.3.1 ~~The time-lagged ensemble~~Ensemble perturbations

~~The~~For the single deterministic analysis, the time-lagged approach (e.g., Branković et al., 1990) is employed to generate the ensemble perturbations, which are created by using deterministic forecasts with different initial times and varying GFS data. For example, the first sample at 00 UTC on 26 July 2021 stores the difference between two deterministic forecasts initialized at 06 UTC on 25 July 2021 and 12 UTC on 25 July 2021. To distinguish these forecasts from the forecasts of the DA experiments, the forecasts used to produce ensemble members are referred to as sample forecasts. The sample forecasts used in this study are shown in ~~Figure 4~~Figure 24-a. Note that some sample forecasts are initialized by the 3-h or 6-h GFS forecast

data (highlighted by the thick tick marks in [Figure 4](#)). Two ensembles differing in size are created: the large ensemble has 36 members and is employed; it combines 96 sample forecasts according to $C(9, 2) = \frac{9!}{2!7!}$, while the small ensemble excludes sample forecasts initialized at 03 UTC and 06 UTC on 25 July 2021. $C(6, 2) = \frac{6!}{2!4!}$ and thus has 15 members ($C(6, 2) = \frac{6!}{2!4!}$).

Compared with the root mean square error (RMSE) of the initial condition, the spreads of both ensembles are deficient, particularly at lower levels (Figure 3) for u , v , w , θ , and q_v . The 36 member ensemble has a larger spread than the 15 member ensemble, but the difference between the two is not distinct even though the ensemble size of the large ensemble is twice that of the small ensemble. This result implies that many members in the ensembles are similar, leading to a small ensemble spread. Therefore, we emphasize that the aforementioned time-lagged ensemble is only valid for the purpose of the deterministic analysis in this study. For a general ensemble-based algorithm, let alone for the cycling DA experiments, the above ensemble may not be good enough.

Focusing on the result of a small size ensemble is based on two concerns. First, Local DA is designed as a flexible scheme for hybrid analysis; hybrid analysis is often beneficial in the presence of a small ensemble or a poor ensemble. In the case of using a well sampled ensemble, the pure ensemble DA is preferred. Second, the available computational resources are not always sufficient to support a large size ensemble. The authors have tested a larger ensemble with 36 members and obtained lower analysis errors than the 15-member counterpart. For brevity, the results with the 36-member ensemble are not shown. For the cycling analysis, the first analysis uses the time-lagged 15-member ensemble. In the remaining cycles, the ensemble forecast initialized from the previous analysis ensemble provides the ensemble perturbations. The analysis ensemble is created by performing Local DA 15 times with perturbed observations. The perturbations are added to Ctrl so that the ensemble center on Ctrl. The Ctrl in the first cycle is obtained using GFS analysis at 00 UTC on 26 July 2021. [Figure 4b](#) shows the flowchart of the cycling DA.

3.3.2 The DA configurations

Two sets of experiments are designed: one for the single deterministic analysis at 00 UTC on 26 July 2021 and one for the cycling analysis from 00 UTC to 18 UTC on 26 July 2021 with a cycling interval of 6 h. For the single deterministic analysis, we first study the influences of the hybrid covariance and multiscale localization on Local DA. Experiment LDA_ctrl is conducted with only the dynamic covariance and fixed localization, whereas LDA_HBC_MSL is the experiment using the hybrid covariance (HBC) and multiscale localization (MSL) simultaneously, and LDA_HBC disables multiscale localization. Second, we investigate the impacts of the localization space. Compared with LDA_HBC_MSL, experiment LDA_DS adopts double space localization (DS). LDA_OS uses observation space localization (OS) and disables

615 the static covariance to exclude the impact of horizontal model-space localization. Moreover, due to the use of 5-column analysis in LDA_OS, the observation space localization is valid only in the horizontal direction, while in the vertical direction, the localization is in the model variable space.

Given that LDA_OS disables the static covariance and performs observation space localization, we seek to evaluate whether LDA_OS produces a deterministic analysis similar to or close to that yielded by the LETKF. Therefore, a LETKF test, called LETKF_OS, is run for this purpose. Because Local DA approximately follows the LETKF procedure, it is not difficult to 620 implement the LETKF for a deterministic analysis within the Local DA framework.

LDA_HBC_MSL_cyc, LDA_ctrl_cyc, and LDA_DS_cyc are the cycling DA experiments that use the same configurations of their counterparts named without the suffix “_cyc”. These experiments perform cycling DA at 00 UTC, 06 UTC, 12 UTC, and 18 UTC on 26 July 2021. A shorter cycling interval has been tested (not shown), and the resulting forecast errors of most 625 variables during the cycling are large, as expected. The shock to the model is simply a cause, as will be shown in Sect. 4. Again, we emphasize that the cycling DA experiments of Local DA are just for reference.

The aforementioned experiments are conducted with the 15 member ensemble. Thus, to examine the sensitivity of Local DA to the ensemble size, we rerun LDA_HBC_MSL, LDA_OS, and LETKF_OS with the 36 member ensemble, and the rerun experiments are referred to as LDA_HBC_MSL_36m, LDA_OS_36m, and LETKF_OS_36m, respectively. In addition, 630 LDA_DS is rerun with only the static correlation matrix to discern the contribution of static information to Local DA; the experiment is named LDA_DS_noENS. For convenience, all experiments are listed in Table 1, where “M” and “O” denote the model variable and observation variable spaces, respectively.

The model variables to be updated A total of 14 experiments for deterministic analyses at 00 UTC on 26 July 2021 are examined. The first three experiments investigate the influence of using the pure ensemble covariance (Ens noFLTR), distant correlation covariance (Static_BE), and hybrid covariance (Hybrid_noFLTR) on the Local DA analysis. The model 635 variables to be analyzed are the three wind components (u , v , w), potential temperature (θ), water vapor mixing ratio (q_v), dry-air mass in column (mu), and hydrometeor mixing ratios (q_c , q_r , q_i , q_s , and q_g). The DA-related parameters are listed as follows. The A fixed localization radius is of 200 km. Multiscale is used for most variables. For ps and hydrometeor variables (q_c , q_r , q_i , q_s , and q_g), the fixed influence radii are 1000 km and 20 km, respectively. These values are tuned for the 640 case in which Typhoon In-Fa made landfall in this study and are only used for static correlation and experiments without multiscale localization (e.g., Ens noFLTR). The background error covariance is empirically inflated by 50%. For Hybrid_noFLTR, the weight between the dynamic and static covariances is 0.5.

Then, the impact of model-space multiscale localization is evaluated through 6 experiments with/without the hybrid covariance. Ens_2band, Ens_3band, and Ens_5band use the pure ensemble covariance, but the ensemble is decomposed into 2, 3, and 5 scales, respectively. The 2-band experiment uses five bands of samples: <20 km, 20 km—50 with a scale of 0 km, - 200 km and a scale greater than 200 km. In this experiment, the contribution of a scale greater than 200 km is amplified because the localization coefficient is 1.0 until the distance between two grid points is greater than 200 km. For the 645 Ens_3band, the three scales are 0 km - 50 km—, 50 km - 200 km, and >200 km. The corresponding values for Ens_5band are

0 km - 20 km, 20 km - 50 km, 50 km - 100 km, 100 km - 200 km, and >200 km; the localization of these bands is enabled as the distance reaches 0 km, 20 km, 50 km, 100 km, and 200 km, respectively, with corresponding radii of 20 km, 50 km, 100 km, 200 km, and 500 km. For 200 km, and >200 km, respectively. Through the above three experiments, we can examine the sensitivity of Local DA to the configuration of multiscale analysis. Hybrid 2band, Hybrid 3band, and Hybrid 5band use the same ensemble covariance as Ens 3band, and Ens 5band, respectively; the ensemble covariance and static covariance weight equally in the hybrid covariance.

The last five experiments are designed to discuss the impact of the localization space. Ens noFLTR OL performs localization in observation-space localization, the horizontal radii are 360 km, 150 km, 120 km, and 15 km for sounding, wind profiler, PWV, and radar data, respectively. The vertical radius for all observations is 5 km. The vertical location of a PWV observation is assumed to be 4 km above sea level, which is used in LETKF_OS. For Local DA, we specifically assign fixed localization radii of 1000 km and 20 km for the model variable ps and the reflectivity related variables, respectively. These values are tuned for the case in which Typhoon In Fa made landfall in this study. The other DA parameters are 0.5 for the hybrid parameter γ and 1.5 for covariance inflation; both are empirically assigned. Notably, Ens noFLTR OL performs vertical localization in model space, identical to Ens noFLTR. Ens LETKF uses the LETKF algorithm and the same horizontal localization radii as Ens noFLTR OL. The vertical radius for all observations is 5 km, where the PWV observations are supposed to be available at 4000 m for LETKF localization. Ens noFLTR DSL performs localization in both the model and observation space. In the model space, a fixed localization radius is used, as in Ens noFLTR, while the localization parameters of Ens noFLTR OL are adopted for observation-space localization. By using 5-band samples, Ens noFLTR DSL becomes Ens 5band DSL. Adding hybrid covariance to Ens 5band DSL yields Hybrid 5band DSL. For convenience, all single deterministic analysis experiments are listed in Table 3, where “M” and “O” denote the model and observation spaces, respectively.

For experiments with cycling analysis, we examine Local DA in the cases of i) using the ensemble covariance without multiscale localization and ii) using hybrid covariance and multiscale localization. The DA configuration of Ens noFLTR is employed for the first scenario, while that of Hybrid 5band DSL is adopted for the second scenario. Cycling intervals of 3-h and 6-h are examined, where we mainly focus on the experiments with the 6-h interval. The experiment with a 3-h cycle interval is used to show the impact of imbalance analysis to forecast. A total of three experiments are examined, namely, Ens noFLTR 6h, Hybrid 5band DSL 6h, and Hybrid 5band DSL 3h, where the suffixes represent the cycling intervals. During cycling, sounding observations are available at 00 UTC and 12 UTC, while other observation types are available hourly. Fifteen sets of perturbed observations are created to update 15 members in cycling DA. The standard deviations of observation perturbations are identical to the observation errors mentioned in sect. 3.2. The covariance inflation factor is also 1.5 for cycling analysis.

4 Results and discussion

4.1 The convergence of minimization

We examine the minimization convergence by using the data extracted from [LDA_HBC_MSLHybrid_5band](#). [Figure 5Figure-45](#) shows the number of iterations and the ratio of the final value of the cost function (J_{final}) to the initial value (J_{initial}). Fewer than 100 iterations ~~indicates~~[indicate](#) that the tolerance ϵ^2 reaches 1×10^{-6} within 100 steps. If the minimization does not converge within 100 steps, the CG iteration is stopped by the program. The number of iterations is large near the center of the forecast domain but decreases rapidly outward. According to the distribution of observations ([Figure 3Figure-43](#)), the results ([Figure 5Figure-45a](#)) indicate that the minimization converges more slowly as the number of observations to be assimilated increases.

Although the minimization fails to converge within 100 steps in the area where the observation density is high, the cost function is ~~still~~[reduced](#) by 70% or 80% ([Figure 5Figure-45b](#)). In contrast, near the northeastern and southeastern corners of the domain, where the minimization converges within 10 steps, the final value of the cost function is ~~larger~~[greater](#) than 70% of its initial value. However, in those areas ~~of the domain~~, the initial cost function is small, implying no need for a large ~~extent of~~ correction. The results also indicate that no ~~serious~~[severe](#) discontinuity occurs in [LDA_HBC_MSLHybrid_5band](#), which is desired. Similar to the LETKF, ~~the use of~~[using](#) slightly different C_{oo} between neighboring columns does not yield remarkably different analyses.

Further investigation (for data within the yellow rectangle plotted in [Figure 5Figure-45a](#)) indicates that approximately 25% ~~of~~ minimizations fail to converge within 100 steps ([Figure 6Figure-56a](#)), all associated with the application of radar data. Therefore, we rerun [LDA_HBC_MSLHybrid_5band](#) using only radar data and observe that only 4% of all minimizations require more than 100 steps to converge. In the case of setting the maximum number of iterations to 500 for [LDA_HBC_MSLHybrid_5band](#), all minimizations converge within 300 iteration steps. The results also show that assimilating only radar data produces a smaller ratio of J_{final} to J_{initial} than the case using all observations ([Figure 6Figure-56b](#)). ~~Therefore, we speculate that it may be difficult for the current version of Local DA to converge within a few iteration steps when multiple types of observations are ingested. Nevertheless, despite this difficulty~~[b](#)). [According to previous studies \(e.g., Wang and Wang, 2017\), the inefficient minimization may be caused by the assimilation of radar reflectivity due to the use of the mixing ratios as state variables. Too small hydrometeor mixing ratio values can lead to an overestimated cost function gradient. Nevertheless, despite the slow convergence](#), Local DA reduces the cost function by more than 70% within 100 iteration steps in most cases ([Figure 6Figure-56b](#)). Further suppressing the error may require a better background error covariance, which we plan to seek in future work.

4.2 The ~~DA performance~~[single deterministic analysis](#)

~~The RMSE is used to evaluate the analysis quality. For the horizontal wind components, all experiments using the 15-member ensemble produce an analysis error smaller than the background error from the lower level to the upper level~~

(Figure 6a, b). Moreover, the RMSEs of the experiments using the hybrid method (LDA_HBC_MSL, LDA_HBC, and LDA_DS) are consistently smaller than those of the experiments without the static covariance (LDA_ctrl, LDA_OS, and LETKF_OS). The RMSE profiles of LDA_HBC_MSL and LDA_HBC are similar, implying that the hybrid method plays a more important role than multiscale localization. Huang et al. (2019) has demonstrated that the high-rank ensemble transform Kalman filter is insensitive to the localization length scale, thus the high-rank background correlation matrix, C_{oe} , is likely another cause of the relatively small impact of the multiscale localization. Using double space localization (LDA_DS) further decreases the RMSE of LDA_HBC_MSL at approximately all levels, which is an indicator of using a poor ensemble in the analysis because performing localization in the model variable space alone is insufficient to suppress spurious correlations. These results highlight the necessity of using the hybrid covariance when the ensemble is poor. Similar results can be observed for hydrometeor variables (Figure 6f i). Although multiscale localization does not produce distinctly different wind components between LDA_HBC_MSL and LDA_HBC, it does result in a smaller RMSE for the hydrometeor variables in LDA_HBC_MSL. Thus, multiscale localization is beneficial for the analysis performance. For other variables (w , θ , and q_v), LDA_DS produces consistently smaller errors than the other experiments, while the differences between the other experiments are not as distinct. In most cases, LDA_ctrl exhibits the worst performance. Using a fixed radius of 200 km and a poor ensemble are the main causes of the poor performance of LDA_ctrl.

To qualitatively assess the analysis error, we compute the difference in total energy (DTE, Meng and Zhang, 2007). LDA_ctrl (Figure 7 d f) decreases the large background errors (Figure 7 a c) at 850 hPa and 500 hPa but generates many spurious increments over the ocean, increasing the error there; this problem is more pronounced at 200 hPa. Accordingly, LDA_ctrl fails to substantially reduce the error for the entire domain. Because the spurious increment is a result of using a poor ensemble, utilizing the hybrid method that suppresses the impact of the ensemble yields smaller errors (LDA_HBC_MSL, Figure 7 g i) from the lower to the upper levels. The spurious increment is further reduced in LDA_DS, especially at 850 hPa and 500 hPa, corresponding to the smallest analysis error in Figure 6. For LDA_OS and LETKF_OS, we consider mainly whether their analyses are similar. According to the results shown in Figure 8, the two experiments produce similar analyses, but the Local DA analysis is noisier, which implies that the LETKF is better than Local DA as a stand-alone ensemble-based algorithm.

For the perturbation of the dry air mass in column (mu), although LDA_ctrl corrects the overestimate of the central pressure, it severely underestimates mu in the typhoon center (Figure 9b), leading to a larger RMSE after DA. In addition, the analysis of LDA_ctrl is noisy, which is attributable to the unreliable error correlation estimated by the ensemble because LDA_HBC_MSL and LDA_DS (Figure 9c, d), which weaken the impact of the ensemble, generate smaller analysis errors and less noise. Many spurious increments are still observed in LDA_HBC_MSL and LDA_DS, which may require a better covariance or a static constraint to resolve. The analysis errors of mu in LDA_OS and LETKF_OS (Figure 9e, f) do not differ substantially, as expected. In general, Local DA with the hybrid method and multiscale localization is able to reduce the surface pressure error, but the results are not good enough in terms of the spurious increment.

Figure 10 shows the evolutions of the forecast error for the aforementioned experiments. All the DA experiments produce smaller forecast errors than the experiment without DA (BAK) throughout the 18 h forecast in terms of the observation variables. For nearly all investigated variables, the experiments using the hybrid covariance produce smaller errors than the experiments using only the ensemble-based covariance. This finding is consistent with the results in Figure 6. LDA_DS often yields the smallest forecast errors for the wind-related variables (radial velocity and wind profiler observations) because its analysis errors for u and v are the smallest. Despite the small forecast errors yielded by all the DA experiments, the shock to the model cannot be ignored, particularly for Z and ps (Figure 10b, f). For this issue, the noisy and imbalanced mu analysis is one contributor; the other contributor is likely the lack of a cross-variable balance adjustment after DA (e.g., Zeng et al., 2021). The spin up time for the shock is approximately 3 h; thus, the current version of Local DA cannot perform hourly cycling DA. Although the forecast results are encouraging, we emphasize that these results are obtained assuming a perfect model; hence, we plan to conduct experiments with an imperfect model or using real observations in future work to further assess the capabilities of Local DA.

4.2.1 The sensitivity to the ensemble size

Since the 15 member ensemble has large sampling errors that degrade the Local DA analysis quality, in this subsection, we investigate whether the 36 member ensemble is helpful for reducing the analysis error. Specifically, LDA_HBC_MSL, LDA_OS, and LETKF_OS are rerun by using the 36 member ensemble. Figure 11 shows comparisons between the experiments using the 15 member and 36 member ensembles. For u , v , q_e , q_s , and q_i (Figure 11a, b, f, g, and h), the positive impact of using a large size ensemble is notable. The reduction in the analysis error is larger in LDA_OS_36m and LETKF_OS_36m than in LDA_HBC_MSL_36m; a straightforward reason for this distinction is that the impact of the ensemble is reduced by 50% in LDA_HBC_MSL_36m due to the use of the hybrid covariance. Additionally, even though the analysis errors of the aforementioned variables are substantially reduced in LDA_OS_36m and LETKF_OS_36m, the errors are still larger than or comparable to those in LDA_HBC_MSL, further indicating the importance of utilizing the hybrid covariance. For the other variables, the impacts of using the 36 member ensemble are relatively small and inconsistent.

The forecast results shown in Figure 12 are consistent with the analysis results in Figure 11; namely, the errors in LDA_HBC_MSL_36m, LDA_OS_36m, and LETKF_OS_36m are smaller than their counterparts using the 15 member ensemble for all the investigated variables. For V_r , Z , u , v , and ps , the forecast errors of LDA_HBC_MSL_36m are often the smallest (Figure 12). Although the analysis error difference between LDA_HBC_MSL_36m and LDA_HBC_MSL is not large, the difference becomes distinct by the end of the 18 h forecast. Moreover, the shock to the model is alleviated in LDA_HBC_MSL_36m in terms of Z and ps , indicating that the large sampling error is a contributor to the imbalanced analysis. In general, Local DA can utilize a large ensemble size to improve the analysis.

4.2.2 The impact of static covariance

The difference between LDA_ctrl and LDA_HBC highlights the importance of blending the static covariance, even though the static covariance is composed only of distance correlation information. In this subsection, we assess the performance of Local DA in the case of using the static covariance only. To achieve this goal, we rerun LDA_DS with the weight of static covariance being 1.0 (LDA_DS_noENS). For brevity, only the forecast results are shown in Figure 13, revealing that LDA_DS yields smaller analysis errors for all the evaluated variables than does LDA_DS_noENS; again, this finding highlights the importance of hybrid DA. However, the main contributor to the small analysis error is the static covariance. Without the ensemble-based covariance, the analysis error of LDA_DS_noENS is not much larger than that of LDA_DS. For *PWV* and *ps*, the forecast errors of both experiments are much closer; this result, on the other hand, demonstrates the ability of Local DA to run without the ensemble. Nevertheless, considering the poor quality of the time-lagged ensemble used in this study, the results shown in Figure 13 do not represent the superiority of the static covariance over the dynamic covariance.

4.2.3 The cycling DA performance

In this subsection, the cycling DA performances are evaluated. For the sake of a fair comparison, the LETKF is not involved because we conduct only the single deterministic analysis and forecast. Figure 14 shows that the forecast errors at 12 UTC and 18 UTC in the cycling DA experiments are smaller than those in the forecasts with a single deterministic analysis, indicating that Local DA can be used for cycling DA. LDA_HBC_MSL_cyc and LDA_DS_cyc produce consistently smaller forecast errors than LDA_ctrl_cyc for most of the observation variables, except for the radar observations at 18 UTC; this outcome is expected because the ensemble is not updated, so the pure ensemble-based Local DA analysis cannot produce errors comparable to those of the hybrid approach through cycling DA. Given the poor ensemble used in this study, we expect that using a well-sampled and updated ensemble would yield a lower forecast error during cycling DA.

Let us have a quick look at the results. For convenience, the initial condition extracted from GFS analysis is referred to as BAK. All experiments reduce the root mean square root errors (RMSEs) in the observation space after DA, but their differences are significant (Figure 7). The experiments (Ens noFLTR, Ens noFLTR OL, Ens LETKF, and Ens noFLTR DSL) without the hybrid covariance and model-space multiscale localization produce relatively higher analysis errors than other experiments for wind components, temperature, radial velocity, and reflectivity. Using distance correlation (Static BE) results in lower errors than Ens noFLTR for most variables, while Hybrid noFLTR further suppresses the errors except for reflectivity. The benefit of using hybrid covariance is consistent with many previous studies (e.g., Wang et al., 2009; Wang et al., 2013b; Tong et al., 2020).

Model-space multiscale localization (Ens 2band, Ens 3band, and Ens 5band) is conducive to error reduction. Even with 2-scale samples, Ens 2band dramatically reduces the errors of wind-related variables, compared with Ens noFLTR. Involving more scales further improves the analysis, but the benefit is not as great as the case of comparing Ens noFLTR with

840 Ens 2band. Combining the hybrid covariance and model-space multiscale localization does not further narrow the gap between the analysis and observation.

Double-space localization does not necessarily ensure small analysis errors (Ens noFLTR DSL). However, when the localization is combined with the hybrid covariance and model-space multiscale localization (Hybrid 5band DSL and Ens 5band DSL), the analysis error can be substantially reduced, especially for PWV and reflectivity.

845 In model space, similar results can be observed (Figure 8). The hybrid covariance, model-space localization, and double-space localization are helpful for error reduction. Notably, unlike the result in the observation space, the analysis errors in some experiments are higher than that of BAK. Because the RMSE in model space counts for grid points that are not directly observed and are updated through error covariance, the error becoming higher after DA is likely due to the poor error covariance in model space.

850 In the following subsections, the background and analysis errors in model space are decomposed into three scales by using a Gaussian filter with radii of 50 km and 200 km, respectively, representing errors of the small scale (0 km - 50 km), middle-scale (50 km – 200 km), and large scale (>200 km). Through this decomposition, we can investigate the results in detail. The vertical velocity (w) and hydrometeor variables (q_c , q_r , q_i , q_s , and q_g) are not decomposed because their scales are often small. In addition, convective-scale DA usually computes the errors for grid points with reflectivity larger than a threshold, which is another way to investigate small-scale errors. The difference between errors in the convective area (reflectivity >10 dBZ) and the rest area is similar to that between small-scale and large-scale errors (not shown). Therefore, the errors in the convective area are not discussed in the subsequent sections.

4.2.1 Hybrid analysis

860 Figure 9 shows that the smallest scale error contributes most to the background and analysis error, while the quantities of large-scale errors are often half of their small-scale counterparts. Ens noFLTR reduces errors at all scales for horizontal wind components, where the error reduction is relatively higher at a large scale. For T , q_v , and ps , Ens noFLTR suppresses the large-scale errors but amplifies the small-scale ones. This result implies that the large-scale error covariance is likely reliable but the smaller one is not.

865 When the static correlation is enabled for Local DA (Static BE and Hybrid noFLTR), the small-scale and middle-scale errors are substantially decreased. This difference becomes much larger for ps when Ens noFLTR is compared with Static BE, even at a large scale. The analysis errors of Static BE and Hybrid noFLTR are nearly identical at all scales for u , v , T , and q_v , but the reason for this phenomenon is still unknown. We plan to determine the cause in future work. Overall, the main contribution of employing static correlation to the lower analysis errors of Static BE and Hybrid noFLTR is at a small scale. The result implies that constraining the small-scale ensemble correlation in a small radius may be conducive to the small analysis error, which is what the model-space multiscale localization does.

4.2.2 Multiscale analysis

After decomposing the ensemble samples into two parts (Ens_2band) and independently applying the localization radius for each scale, the small-scale analysis error becomes lower than that of Ens_noFLTR for all examined variables (Figure 10). Compared with Ens_2band, further decomposing the ensemble samples into more scales (Ens_3band and Ens_5band) and using smaller radii for small scales slightly reduces the analysis error for wind components and surface pressure but increases the error for q_v . This result confirms the speculation that restricting the impact of small-scale correlation in a small region is beneficial. The difference between Ens_3band and Ens_5band is small, indicating that three or five scales should be sufficient for the model-space multiscale localization in Local DA.

Experiments combining multiscale localization with hybrid covariance (Hybrid_2band, Hybrid_3band, and Hybrid_5band) produce lower analysis errors for most variables, compared with Ens_2band, Ens_3band, and Ens_5band. However, the improvement is not substantial. The small difference implies that we need more approaches to make further improvements. Employing double-space localization is one of the approaches, according to the result shown in Figure 8.

4.2.3 Double-space localization

Compared with Ens_noFLTR, Ens_noFLTR_DSL has a small but positive impact on the analysis of u , v , T , and q_v at a small scale, while its influence on larger scale errors is negligible (Figure 11). In contrast, Ens_noFLTR_DSL substantially reduces the analysis error of ps at all scales. After combining the model-space localization (Ens_5band_DSL), the analysis errors further decline at a small scale. Adding a hybrid covariance to Ens_5band_DSL (Hybrid_5band_DSL) leads to lower analysis error for most variables. The large-scale analysis error of ps is increased after using hybrid covariance, implying that the large-scale error correlation related to ps and computed by using ensemble samples is better than the distant correlation with a fixed influence radius. It is encouraging to see that Hybrid_5band_DSL and Ens_5band_DSL produce the analysis error of q_v lower than BAK at small and middle scales, while Ens_5band and Hybrid_5band yield a higher analysis error than BAK. The result indicates the benefit of double-space localization.

To qualitatively assess the analysis error, we compute the difference in total energy (DTE, Meng and Zhang, 2007). Wang et al. (2012) used the square root of the mean DTE to evaluate the error of DA to simplify the presentation. The DTE is computed in the form of the difference between the analysis and truth. Ens_noFLTR (Figure 12 d-f) decreases the background errors (Figure 12 a-c) at 850 hPa and 500 hPa but generates many spurious increments over the ocean, increasing the error there; this problem is more pronounced at 200 hPa. Accordingly, the error after Ens_noFLTR analysis is still high. The spurious increment corresponds to the large analysis error at a small scale. In contrast, utilizing the hybrid covariance and model-space multiscale localization suppresses the small-scale spurious errors (Hybrid_5band, Figure 12 g-i) from the lower to the upper levels. The spurious increment is further reduced in Hybrid_5band_DSL, especially at 850 hPa and 500 hPa.

4.2.4 The similarity between Local DA with observation space localization and the LETKF

Considering that Local DA can perform observation space localization only as in the LETKF, it is interesting to see if their analyses are similar. Note that Ens noFLTR OL and Ens LETKF merely share the same horizontal localization configuration; they differ in vertical localization. Figure 13 shows that the difference in analysis error between Ens noFLTR OL and Ens LETKF is small for all variables and at all scales. Figure 14 gives an intuitive comparison between the Ens noFLTR OL and Ens LETKF analyses. The overlarge negative-increment in both experiments is constrained in a much smaller area than Ens noFLTR (marked by red rectangles in Figure 14). They also suppress the small-scale noise in the Ens noFLTR analysis, corresponding to the lower error in Figure 13e. Overall, in the case of using observation-space localization, Local DA can produce an analysis similar to the LETKF.

In addition, the small-scale error of q_v yielded by Ens noFLTR OL is lower than that of Ens noFLTR (Figure 13d). The result is similar to the difference between Ens noFLTR DSL and Ens noFLTR, indicating that the improvement of Ens noFLTR DSL on q_v analysis compared with Ens noFLTR is mainly attributable to observation-space localization.

4.2.5 Error and ensemble spread

For a well-sampled ensemble, a criterion is that the spatial distribution of the ensemble spread is similar to that of RMSE. In addition, the amplitudes of the ensemble spread must be close to the RMSE. The relationship is shown in Figure 15 for the time-lagged ensemble at 00 UTC on 26 July 2021. For u , v , and ps , the ratio of ensemble spread to RMSE ascends as the error scale increases, indicating that the quality of the time-lagged ensemble is rational at a large scale. This relationship is also valid for the spatial distribution (Figure 15b), but the correlation coefficient does not vary from small scale to large scale too much for most variables, except for ps . The correlation coefficient for ps is nearly 1.0 at a large scale, while it is approximately 0.6 at a small scale. This large difference explains why the hybrid covariance and multiscale localization can substantially reduce the error at a small scale for ps . For q_v , the small-scale spread is greater than the large-scale spread; the correlation coefficients at all scales are close. This result implies that suppressing the small-scale error covariance does not necessarily improve the analysis quality of q_v . Therefore, it is not irrational for Ens 5band and Hybrid 5band to produce a higher analysis error for q_v than Ens 2band.

An example related to the ensemble spread and RMSE of ps is shown in Figure 16. The RMSE is smooth at a small scale, and there is a maximum near the typhoon center. Although the ensemble spread also has a maximum near the typhoon center, there is a large bias concerning the location. Moreover, the ensemble spread is much noisier than the RMSE, which is a cause of the noisy analysis shown in Figure 14b. In contrast, the large-scale ensemble spread matches the error well, which is conducive to error reduction. Therefore, even with a large localization radius, the surface pressure analysis of Ens noFLTR at a large scale is not much worse than that of the other experiments.

4.3 The cycling DA

Because ensemble DA approaches often take several cycles to obtain a reasonable analysis, it is worth seeing if Ens_noFLTR produces a better analysis after some cycles and if Hybrid_5band_DSL maintains the advantage in cycling DA. Before looking at the RMSE evolution during cycling, the ps tendency is examined as it is a metric of dynamic imbalance (Zeng et al., 2021). If the unphysical ps tendency is large, the analysis may be degenerated, and the forecast could be unstable. Although it is better to analyze the ps tendency at each time step, in this study, the hourly ps tendency is sufficient to demonstrate the impact of imbalance analysis. The forecast from GFS analysis is referred to as BAK in this subsection.

4.3.1 The tendency of ps

The ps tendency in the truth simulation is selected as a criterion as it is assumed to be in balance status after a 24-h forecast. The balanced tendency is approximately 20 Pa h^{-1} (Figure 17), which is reached by BAK in 3 h. After the first DA cycle, the ps tendency becomes much larger than that of BAK, no matter the DA configuration. The large ps tendency after the first DA cycle is not surprising because the landing typhoon is not fully observed by the simulated observation network, especially for the wind field, causing an imbalance between the corrected part and the rest of the analyzed typhoon. A similar phenomenon was discussed by Wang et al. (2012) in a simulated supercell case. They concluded that such an imbalance shocks the model forecast and increases the forecast error.

After a 6-h forecast, the ps tendencies in Hybrid_5band_DSL_6h and Ens_noFLTR_6h are close to the balance status. As expected, the ps tendency increases again after the second DA cycle. However, Hybrid_5band_DSL_6h produces a much smaller ps tendency than Ens_noFLTR_6h, indicating that Hybrid_5band_DSL_6h has a more balanced analysis. The peaks of ps tendency in Hybrid_5band_DSL_6h and Ens_noFLTR_6h gradually decline as the number of cycles increases. By 18 UTC, Hybrid_5band_DSL_6h reaches the balance status while Ens_noFLTR_6h does not. The above result indicates that using the hybrid covariance and multiscale localization is beneficial for cycling DA.

Note that the advantage of Hybrid_5band_DSL_6h has a precondition that the cycling interval is sufficiently long for the model to spin up. When the cycling interval becomes shorter (Hybrid_5band_DSL_3h), the ps tendency cannot be effectively suppressed as Hybrid_5band_DSL_6h does.

4.3.2 The performance of cycling DA

We only discuss the results of u , v , q_{v2} , and ps in this subsection for brevity. For u and v , all experiments reduce the forecast error compared with BAK (Figure 18a and b). However, the error evolutions of these experiments substantially differ. Ens_noFLTR_6h fails to decrease the forecast error after the second cycle, while Hybrid_5band_DSL_6h successively reduces the forecast and analysis error as the number of cycles increases. For Hybrid_5band_DSL_3h, an oscillation in error evolution is observed, which is likely associated with the imbalance analysis and the insufficient cycle

interval for spinup. Despite the oscillation, the forecast and analysis errors of Hybrid 5band DSL 3h are comparable to those of Hybrid 5band DSL 6h for wind components.

However, in regard to water vapor and surface pressure (Figure 18c and d), Hybrid 5band DSL 6h becomes better than Hybrid 5band DSL 3h. Hybrid 5band DSL 6h also outperforms Ens noFLTR 6h; the latter fails to suppress the forecast error of q_v and produces a higher ps error after analysis. Figure 19 shows the spatial distribution of forecast error at 18 UTC for Hybrid 5band DSL 6h and Ens noFLTR 6h. The area of large error in Hybrid 5band DSL 6h is much lower than that of Ens noFLTR 6h for both v and ps . The large error in Ens noFLTR 6h corresponds to a weak cyclonic rotation and weak low pressure. The above result confirms the benefit of using the hybrid covariance and multiscale localization.

4.3.3 The evolution of the relationship between ensemble spread and RMSE

For Hybrid 5band DSL 6h, the initial ensemble spread is smaller than the RMSE at all scales (Figure 20a) for both u and ps . As the number of cycles increases, the ratio of ensemble spread to RMSE increases. By 18 UTC, the ensemble spread is comparable to or greater than the corresponding RMSE at all scales for u . The underestimation of RMSE by the ensemble spread is alleviated for ps (Figure 20b). For the spatial distribution, the relationship between the ensemble spread and RMSE does not vary much for u at all scales (Figure 20c). In contrast, the relationship becomes better for ps at a small scale (Figure 20d). Overall, the ensemble is improved in Hybrid 5band DSL 6h.

For Ens noFLTR 6h, the ensemble spread of u and ps at the small-scale remains smaller than the corresponding RMSE during the cycling DA. In contrast, the ensemble spread at the large scale dramatically increases after the second cycle. The amplitude of the large-scale ensemble spread is even higher than that of the small-scale spread, leading to a severe overestimation of the large-scale error. Meanwhile, the correlation between ensemble spread and RMSE at the small scale is not improved during cycling. In general, the ensemble in Ens noFLTR 6h does not become better after four cycles, which explains why Ens noFLTR 6h produces a large analysis error.

4.4 The computational cost and efficiency

The computational cost and efficiency of Local DA are discussed in this subsection. All tests are conducted on a 36-core workstation with an Intel Xeon Gold 6139 CPU (the maximum frequency is set to 2.30 GHz) and 48 gigabytes of available memory. Heretofore, we have implemented the parallel Local DA with OpenMP, which is not suitable for large-scale parallel computing; however, for the purpose of this study, OpenMP is sufficient. The parallel efficiency is examined first. LDA_HBC_MSL is selected as an example. Figure 21 shows the wall clock time as a function of the number of cores. The wall clock time covers Local DA steps 3) through 9) (as described in Sect. 2d). As expected, the wall clock time is reduced by approximately 50% upon doubling the number of cores, which is valid if the number of cores is not greater than 16. In contrast, increasing the number of cores from 16 to 32 does not shorten the wall clock time; this is attributable to the fact that OpenMP is suitable only when the number of processors is small (<16) (Hoeflinger et al., 2001) (Hoeflinger et al., 2001). Given that no messages need to be passed between the cores for steps 3) through 9), the parallel efficiency of

1025 Local DA is likely insensitive to the number of cores. In general, the results demonstrate that Local DA can be highly parallelized.

In addition to its parallelization, the computational speed of Local DA is also investigated. [LDA_HBC_MSLHybrid_5band](#) takes 225 s to complete all local analyses when 16 cores are used. Note that the number of horizontal grid points within the forecast domain is 40000, and more than 200000 observations are assimilated. Given that the processors work at a frequency of 2.30 GHz, the computational speed of Local DA is acceptable. On average, nearly 70% of the computational time is used to compute C_{oo} and C_{mo} ; for the minimization using the CG method, the corresponding percentage is approximately 18%.

We also assess the memory consumption of Local DA. To complete Local DA steps 3) through 9), [LDA_HBC_MSLHybrid_5band](#) uses approximately 4 gigabytes when 16 cores are engaged to store C_{oo} and the associated matrices. [ByIn](#) contrast, the LETKF uses only hundreds of megabytes. For each 5-column analysis, the C_{oo} size [approximately](#) varies from 2000×2000 to 4500×4500 , which is affordable. However, for a much larger size, such as 9000×9000 , OpenMP is insufficient; under these circumstances, the MPI-OpenMP hybrid scheme is likely a viable solution for both the computational speed and the memory consumption, which is [what we are working on in progress](#). In addition to C_{oo} , [the model-space multiscale localization requires large memory](#). Memory consumption is proportional to the number of scales. For example, [Ens_3band requires three times as much memory as Ens_noFLTR to store the decomposed perturbations](#). In general, the total computational cost of Local DA is high, but the cost of each local analysis is affordable. [With proper data thinning and parallelization, it is possible for Local DA to be used in the assimilation of real observations](#).

5 Summary and conclusions

This study proposed a local data assimilation scheme (Local DA) that can utilize [the](#) hybrid covariance and multiscale localization [simultaneously](#). Local DA explicitly computes a local background error correlation matrix and uses the correlation matrix to construct a local error sample matrix. [After localization, the](#) The error sample matrix [with proper localization](#) allows Local DA to adopt the conjugate gradient (CG) method to solve the cost function. The constructed matrix also [allows renders](#) Local DA to [perform analyses by using only static correlation information](#). [be a flexible hybrid analysis scheme](#). Local DA is [assessed assuming evaluated in](#) a perfect model [and by using scenario that includes a](#) simulated multiscale [observations of observation network for](#) a typhoon case. We [examine examined the impacts of the hybrid covariance and multiscale localization on Local DA and evaluated](#) the performance of [Local DA in both a single deterministic forecast and](#) cycling DA. [Only deterministic analyses and forecasts are considered](#). Several conclusions can be drawn from the results of the DA experiments:

- i) Applying the CG method independently for each column group does not result in a [serious severe](#) discontinuity in the Local DA analysis;
- ii) Explicitly computing the background correlation matrix projected onto observation-associated grids/columns is computationally affordable if the observations have been properly thinned;

iii) Local DA can effectively utilize the hybrid covariance to produce a better analysis ~~with a small ensemble size compared with an~~ than the analysis using ensemble ~~error information only~~ covariance with a fixed localization radius;

iv) ~~In the case of using a poor ensemble, the hybrid covariance plays a more important role than does~~ The model-space multiscale localization; in such a scenario, performing localization in both the model-variable space and the observation-variable space can further decrease can reduce the analysis error ~~compared with Local DA featuring only~~ at a small scale; combining the hybrid covariance with the multiscale localization ~~of the model-variable space~~ yields a small improvement; adding double-space localization to the combination can further reduce the analysis error;

v) Local DA requires a large amount of memory, but its computational efficiency is acceptable.

As the first study to present Local DA, this paper focuses on describing its idea and basic formulation ~~and algorithm~~. Future efforts to enhance the algorithm will include developing an MPI-OpenMP hybrid parallel scheme, a static covariance scheme that objectively determines the error variance and scales, and a better multiscale localization scheme. Furthermore, the current version of Local DA introduces a strong shock to the model, which limits the applicability of Local DA in cycling DA. Therefore, we plan to add a cross-variable balance procedure after Local DA to improve the cycling DA performance.

Moreover, many parameters of Local DA have yet to be tested; hence, the sensitivity of Local DA to each of these parameters will also be discussed in a future investigation.

Code and data availability

The code of Local DA v1.0 and the scripts for running the experiments in this study is available at the following link: <https://doi.org/10.5281/zenodo.6609906> or by contacting the corresponding author via e-mail. The GFS data are available at <https://www.ncdc.noaa.gov/data-access/model-data/model-datasets/global-forecast-system-gfs>.

Author contributions

Shizhang Wang performed the coding and designed the data assimilation experiments. Xiaoshi Qiao analyzed the experimental results. Both authors contributed to the writing of the paper.

Competing interests

The authors declare that they have no conflicts of interest.

Acknowledgments

This work is jointly sponsored by the National Science and Technology Major Project of the Ministry of Science and Technology of China (2021YFC3000902) and the National Natural Science Foundation of China (41875129, 41505090, and 42105006).

Appendix

This section provides an example of the procedure used to thin the observations (as mentioned in Sect. 2b). The observations are thinned horizontally, whereas thinning does not occur in the vertical direction. First, we set several rings with different radii at the center point or column of the model variables to be updated. For the 5-column analysis, the center coordinates of the variable-radius rings are the mean latitude and mean longitude of the 5 columns. The radius of the outer ring is the observation search radius mentioned in Sect. 2d (e.g., 300 km for sounding data and 15 km for radar data). From small to large, the radii of the rings are denoted $rr_1, rr_2, \dots, rr_{Nr}$, where Nr is the number of rings. We successively search the observations from the inner ring to the outer ring. Within the smallest ring, all ambient observations are selected; this is equivalent to no thinning. For the observations located between two rings (between rr_i and rr_{i+1}), we select one observation for each quadrant of the space between the two rings. There are four quadrants: the upper-right, lower-right, lower-left and upper-left quadrants (numbered I, II, III, and IV, respectively). A schematic plot is shown in [Figure A1](#). If no observation is available in the smallest ring, the second ring is treated as the first ring.

Because no thinning occurs in the smallest ring, in a 1-column analysis, we still utilize all observations throughout the forecast domain when Local DA is conducted at a single point. In the 5-column analysis, the thinning approach discards some observations and slightly increases the analysis error relative to the 1-column analysis. Our early test (not shown) indicates that Local DA becomes very time-consuming when the thinning process is disabled, as expected. Moreover, the resulting analysis error increases because the assumption of observation errors being uncorrelated is not valid, which is not desired.

References

- Bonavita, M., Trénolet, Y., Holm, E., Lang, S. T., Chrast, M., Janisková M., Lopez, P., Laloyaux, P., de Rosnay, P., and Fisher, M.: A strategy for data assimilation, European Centre for Medium Range Weather Forecasts Reading, UK2017.
- Branković, Č., Palmer, T., Molteni, F., Tibaldi, S., and Cubasch, U.: Extended-range predictions with ECMWF models: Time-lagged ensemble forecasting, *Quarterly Journal of the Royal Meteorological Society*, 116, 867-912, 1990.
- Brousseau, P., Berre, L., Bouttier, F., and Desroziers, G.: Background-error covariances for a convective-scale data-assimilation system: AROME–France 3D-Var, *Quarterly Journal of the Royal Meteorological Society*, 137, 409-422, 2011.
- Brousseau, P., Berre, L., Bouttier, F., and Desroziers, G.: Flow-dependent background-error covariances for a convective-scale data assimilation system, *Quarterly Journal of the Royal Meteorological Society*, 138, 310-322, 2012.
- Buehner, M.: Evaluation of a spatial/spectral covariance localization approach for atmospheric data assimilation, *Mon Weather Rev*, 140, 617-636, 2012.

- 1115 Buehner, M. and Shlyayeva, A.: Scale-dependent background-error covariance localisation, *Tellus A: Dynamic Meteorology and Oceanography*, 67, 28027, 2015.
Caron, J.-F. and Buehner, M.: Scale-dependent background error covariance localization: Evaluation in a global deterministic weather forecasting system, *Mon Weather Rev*, 146, 1367-1381, 2018.
- 1120 Caron, J.-F., Michel, Y., Montmerle, T., and Arbogast, É.: Improving background error covariances in a 3D ensemble-variational data assimilation system for regional NWP, *Mon Weather Rev*, 147, 135-151, 2019.
Dudhia, J.: Numerical study of convection observed during the winter monsoon experiment using a mesoscale, two-dimensional model, *J. Atmos. Sci.*, 46, 3077-3107, 1989.
Etherton, B. J. and Bishop, C. H.: Resilience of hybrid ensemble/3DVAR analysis schemes to model error and ensemble covariance error, *Mon Weather Rev*, 132, 1065-1080, 2004.
- 1125 ~~Evensen, G.: Sequential Data Assimilation with a Nonlinear Quasi-Geostrophic Model Using Monte Carlo Methods to Forecast Error Statistics, *J Geophys Res Oceans*, 99, 10143-10162, 1994.~~
Gao, J. and Stensrud, D. J.: Assimilation of reflectivity data in a convective-scale, cycled 3DVAR framework with hydrometeor classification, *Journal of the Atmospheric Sciences*, 69, 1054-1065, 2012.
Hamill, T. M. and Snyder, C.: A hybrid ensemble Kalman filter-3D variational analysis scheme, *Mon Weather Rev*, 128, 2905-2919, 2000.
- 1130 Hoefflinger, J., Alavilli, P., Jackson, T., and Kuhn, B.: Producing scalable performance with OpenMP: Experiments with two CFD applications, *Parallel Computing*, 27, 391-413, 2001.
[Hoffman, R. N. and Atlas, R.: Future Observing System Simulation Experiments, *Bulletin of the American Meteorological Society*, 97, 1601-1616, 10.1175/bams-d-15-00200.1, 2016.](#)
- 1135 Hong, S.-Y. and Lim, J.-O. J.: The WRF single-moment 6-class microphysics scheme (WSM6), *Asia-Pacific Journal of Atmospheric Sciences*, 42, 129-151, 2006.
Hong, S.-Y., Noh, Y., and Dudhia, J.: A new vertical diffusion package with an explicit treatment of entrainment processes, *Mon Weather Rev*, 134, 2318-2341, 2006.
[Houtekamer, P. L. and Mitchell, H. L.: Data assimilation using an ensemble Kalman filter technique, *Mon. Wea. Rev.*, 126, 796-811, 1998.](#)
- 1140 Huang, B., Wang, X., and Bishop, C. H.: The High-Rank Ensemble Transform Kalman Filter, *Mon Weather Rev*, 147, 3025-3043, 10.1175/mwr-d-18-0210.1, 2019.
Huang, B., Wang, X., Kleist, D. T., and Lei, T.: A simultaneous multiscale data assimilation using scale-dependent localization in GSI-based hybrid 4D-EnVar for NCEP FV3-based GFS, *Mon Weather Rev*, 149, 479-501, 2021.
- 1145 Hunt, B. R., Kostelich, E. J., and Szunyogh, I.: Efficient data assimilation for spatiotemporal chaos: A local ensemble transform Kalman filter, *Physica D*, 230, 112-126, DOI 10.1016/j.physd.2006.11.008, 2007.
Johnson, A., Wang, X., Carley, J. R., Wicker, L. J., and Karstens, C.: A comparison of multiscale GSI-based EnKF and 3DVar data assimilation using radar and conventional observations for midlatitude convective-scale precipitation forecasts, *Mon Weather Rev*, 143, 3087-3108, 2015.
- 1150 Kain, J. S.: The Kain-Fritsch convective parameterization: an update, *Journal of applied meteorology*, 43, 170-181, 2004.
Kalnay, E. and Yang, S. C.: Accelerating the spin-up of Ensemble Kalman Filtering, *Quart. J. Roy. Meteor. Soc.*, submitted, 2008.
Kleist, D. T. and Ide, K.: An OSSE-based evaluation of hybrid variational-ensemble data assimilation for the NCEP GFS. Part I: System description and 3D-hybrid results, *Mon Weather Rev*, 143, 433-451, 2015.
- 1155 Lei, L., Wang, Z., and Tan, Z.-M.: Integrated Hybrid Data Assimilation for an Ensemble Kalman Filter, *Mon Weather Rev*, 149, 4091-4105, 2021.
[Li, Y., Wang, X., and Xue, M.: Assimilation of radar radial velocity data with the WRF hybrid ensemble-3DVAR system for the prediction of Hurricane Ike \(2008\), *Mon Weather Rev*, 140, 3507-3524, 2012.](#)
[Liu, C., Xiao, Q., and Wang, B.: An ensemble-based four-dimensional variational data assimilation scheme. Part I: Technical formulation and preliminary test, *Mon Weather Rev*, 136, 3363-3373, 2008.](#)
- 1160 Lorenc, A.: The potential of the ensemble Kalman filter for NWP - a comparison with 4D-Var, *Quart. J. Roy. Meteor. Soc.*, 129, 3183-3204, 2003.
Ménardier, B. and Auligné T.: An Overlooked Issue of Variational Data Assimilation, *Mon Weather Rev*, 143, 3925-3930, 10.1175/mwr-d-14-00404.1, 2015.

- 1165 [Maddox, R. A.: An Objective Technique for Separating Macroscale and Mesoscale Features in Meteorological Data, Mon Weather Rev, 108, 1108-1121, 10.1175/1520-0493\(1980\)108<1108:aotfsm>2.0.co;2, 1980.](#)
Meng, Z. Y. and Zhang, F. Q.: Tests of an ensemble Kalman filter for mesoscale and regional-scale data assimilation. Part II: Imperfect model experiments, Mon. Wea. Rev., 135, 1403-1423, Doi 10.1175/Mwr3352.1, 2007.
- 1170 Mlawer, E. J., Taubman, S. J., Brown, P. D., Iacono, M. J., and Clough, S. A.: Radiative transfer for inhomogeneous atmospheres: RRTM, a validated correlated-k model for the longwave, Journal of Geophysical Research: Atmospheres, 102, 16663-16682, 1997.
~~[Parrish, D. F. and Derber, J. C.: The National Meteorological Center's spectral-statistical interpolation analysis system, Mon Weather Rev, 120, 1747-1763, 1992.](#)~~
Penny, S. G.: The hybrid local ensemble transform Kalman filter, Mon Weather Rev, 142, 2139-2149, 2014.
- 1175 Shewchuk, J. R.: An introduction to the conjugate gradient method without the agonizing, Edition, School of Computer Science, Carnegie Mellon University,
Skamarock, W. C., Klemp, J. B., Dudhia, J., Gill, D. O., Barker, D. M., Duda, M. G., Huang, X.-Y., Wang, W., and Powers, J. G.: A description of the advanced research WRF version 3, National Center For Atmospheric Research Boulder CoNCAR/TN-475+STR, 91, 2018.
- 1180 Storto, A. and Andriopoulos, P.: A new stochastic ocean physics package and its application to hybrid-covariance data assimilation, Quarterly Journal of the Royal Meteorological Society, 147, 1691-1725, 2021.
Tang, Y., Ambandan, J., and Chen, D.: Nonlinear measurement function in the ensemble Kalman filter, Advances in Atmospheric Sciences, 31, 551-558, 2014.
- 1185 [Tong, C. C., Jung, Y., Xue, M., and Liu, C.: Direct Assimilation of Radar Data With Ensemble Kalman Filter and Hybrid Ensemble-Variational Method in the National Weather Service Operational Data Assimilation System GSI for the Stand-Alone Regional FV3 Model at a Convection-Allowing Resolution, Geophysical Research Letters, 47, e2020GL090179, 2020.](#)
Wang, S., Xue, M., and Min, J.: A four-dimensional asynchronous ensemble square-root filter (4DEnSRF) algorithm and tests with simulated radar data, Quarterly Journal of the Royal Meteorological Society, DOI:10.1002/qj.1987, 10.1002/qj.1987, 2012.
- 1190 Wang, S., Xue, M., Schenkman, A. D., and Min, J.: An iterative ensemble square root filter and tests with simulated radar data for storm-scale data assimilation, Quarterly Journal of the Royal Meteorological Society, 139, 1888-1903, [2013](#)[2013a](#).
Wang, X., Barker, D. M., Snyder, C., and Hamill, T. M.: A hybrid ETKF-3DVAR data assimilation scheme for the WRF model. Part I: Observing system simulation experiment, Mon Weather Rev, 136, 5116-5131, 2008.
- 1195 Wang, X., Hamill, T. M., Whitaker, J. S., and Bishop, C. H.: On the theoretical equivalence of differently proposed ensemble - 3DVAR hybrid analysis scheme, Mon. Wea. Rev., 135, 1055-1076, 2007.
Wang, X., Hamill, T. M., Whitaker, J. S., and Bishop, C. H.: A comparison of the hybrid and EnSRF analysis schemes in the presence of model errors due to unresolved scales, Mon Weather Rev, 137, 3219-3232, 2009.
- 1200 Wang, X., [Parrish, D., Kleist, D., and Whitaker, J.: GSI 3DVar-based ensemble-variational hybrid data assimilation for NCEP Global Forecast System: Single-resolution experiments, Mon Weather Rev, 141, 4098-4117, 2013b.](#)
[Wang, X.,](#) Chipilski, H. G., Bishop, C. H., Satterfield, E., Baker, N., and Whitaker, J. S.: A multiscale local gain form ensemble transform Kalman filter (MLGETKF), Mon Weather Rev, 149, 605-622, 2021.
- 1205 [Wang, Y. and Wang, X.: Direct Assimilation of Radar Reflectivity without Tangent Linear and Adjoint of the Nonlinear Observation Operator in the GSI-Based EnVar System: Methodology and Experiment with the 8 May 2003 Oklahoma City Tornadoic Supercell, Mon Weather Rev, 145, 1447-1471, 10.1175/mwr-d-16-0231.1, 2017.](#)
[Whitaker, J. S. and Hamill, T. M.: Ensemble data assimilation without perturbed observations, Mon. Wea. Rev., 130, 1913-1924, 2002.](#)
Xiao, Q. and Sun, J.: Multiple-radar data assimilation and short-range quantitative precipitation forecasting of a squall line observed during IHOP_2002, Mon Weather Rev, 135, 3381-3404, 2007.
- 1210 Xue, M., Tong, M. J., and Droegemeier, K. K.: An OSSE framework based on the ensemble square root Kalman filter for evaluating the impact of data from radar networks on thunderstorm analysis and forecasting, J. Atmos. Oceanic Technol., 23, 46-66, 2006.
Yang, C., Min, J., and Tang, Y.: Evaluation of two modified Kalman gain algorithms for radar data assimilation in the WRF model, Tellus A: Dynamic Meteorology and Oceanography, 67, 25950, 2015.

- 1215 Yang, S. C., Kalnay, E., Hunt, B., and E. Bowler, N.: Weight interpolation for efficient data assimilation with the local ensemble transform Kalman filter, *Quarterly Journal of the Royal Meteorological Society: A journal of the atmospheric sciences, applied meteorology and physical oceanography*, 135, 251-262, 2009.
- Zeng, Y., de Lozar, A., Janjic, T., and Seifert, A.: Applying a new integrated mass-flux adjustment filter in rapid update cycling of convective-scale data assimilation for the COSMO model (v5. 07), *Geoscientific Model Development*, 14, 1295-1307, 2021.
- 1220 Zhang, F., Weng, Y., Sippel, J. A., Meng, Z., and Bishop, C. H.: Cloud-resolving hurricane initialization and prediction through assimilation of Doppler radar observations with an ensemble Kalman filter, *Mon Weather Rev*, 137, 2105-2125, 2009.

1225

Table 1 ~~DA experiment configurations~~ The dimensions of variables in Local DA

Experiment names	DA scheme	Static covariance	Dynamic covariance	Localization	Variable space	Multiscale localization	Variable type	Cycling DA dimension	Ensemble size			
LDA_ctrl x^f				Local DA	Model	No	Model variable	Yes/No	M	No	No	15
					space			$m \times 1$				
LDA_HBC_MSL X				Local DA	Model	Yes	Model	Yes/No	M	Yes	No	15
					space		variable	$m \times M$		s		
LDA_HBC $x_0 = H_j x^f$				Local DA	Observed	Yes	Model	Yes/K	M	No	No	15
					grids/columns		variable	$\times 1$				
LDA_DS $X_0 = H_j X$				Local DA	Observed	Yes	Model	Yes/K	M+	Yes	No	15
					grids/columns		variable	$\times M$	\emptyset	s		
LDA_OSC C_{00}				Local DA	Observed	No	Model variable	Yes/K	\emptyset	Yes	No	15
					grids/columns			$\times K$		s		
LETKF_OS v_0				LETKF	Observed	No	Model variable	Yes/K	\emptyset	Yes	No	15
					grids/columns			$\times 1$		s		
LDA_HBC_MSL_eye S_0				Local DA	Observed	Yes	Model	Yes/K	M	Yes	Yes	15
					grids/columns		variable	$\times 1$		s	s	
LDA_ctrl_eye C_{mo}				Local DA	Cross	No	Model variable	Yes/No	M	No	Yes	15
					space			$m \times K$			s	
LDA_DS_eye S_m				Local DA	Model	Yes	Model	Yes/No	M+	Yes	No	15
					grid space		variable	$m \times 1$	\emptyset	s		
LDA_HBC_MSL_36md				Local DA	Observation	Yes	Observation	Yes/No	M	Yes	Yes	36
					DA	Observation	variable	$\times 1$		s	s	
					space							
LDA_OS_36m	Local DA	No	Yes	\emptyset	Yes	No	36					
LETKF_OS_36m	Local DA	No	Yes	\emptyset	Yes	No	36					
LDA_DS_noENS	Local DA	Yes	No	M+ \emptyset	Yes	No	15					

1235
1240
1245
1250
1255

M denotes the ensemble size, N_m is the total number of analysis variables, and K is proportional to the number of observations (N_o)

Table 2 Examples of applying the model-space multiscale localization

<u>Case</u>	<u>Distance between two variables</u>	<u>Variable name</u>	<u>Scale 0 km -20 km</u>	<u>Scale 20 km -200 km</u>	<u>Scale >200km</u>	<u>Multiscale covariance</u>
<u>1</u>	<u>8 km</u>	<u>Localization coefficient</u>	<u>0.5</u>	<u>1</u>	<u>1</u>	
		<u>Localized Covariance</u>	<u>0.5C₁</u>	<u>C₂</u>	<u>C₃</u>	<u>0.5C₁+C₂+C₃</u>
<u>2</u>	<u>80 km</u>	<u>Localization coefficient</u>	<u>0.01</u>	<u>0.5</u>	<u>1</u>	
		<u>Localized Covariance</u>	<u>0.01C₁</u>	<u>C₂</u>	<u>C₃</u>	<u>0.01C₁+0.5C₂+ C₃</u>
<u>3</u>	<u>300 km</u>	<u>Localization coefficient</u>	<u>0.0</u>	<u>0.05</u>	<u>0.5</u>	
		<u>Localized Covariance</u>	<u>0</u>	<u>0.05C₂</u>	<u>0.5C₃</u>	<u>0.05C₂+0.5C₃</u>

C₁, C₂, and C₃ represent the covariance of the small scale (0 km -20 km), middle scale (20 km -200 km), and large scale (>200 km), respectively.

Table 3 DA experimental configurations.

<u>Experiment names</u>	<u>DA scheme</u>	<u>Static</u> <u>covariance</u>	<u>Dynamic</u> <u>covariance</u>	<u>Localization</u> <u>space</u>	<u>Multiscale</u> <u>localization</u>
<u>Ens_noFLTR</u>	<u>Local DA</u>	<u>No</u>	<u>Yes</u>	<u>M</u>	<u>No</u>
<u>Static_BE</u>	<u>Local DA</u>	<u>Yes</u>	<u>No</u>	<u>M</u>	<u>No</u>
<u>Hybrid_noFLTR</u>	<u>Local DA</u>	<u>Yes</u>	<u>Yes</u>	<u>M</u>	<u>No</u>
<u>Ens_2band</u>	<u>Local DA</u>	<u>No</u>	<u>Yes</u>	<u>M</u>	<u>Yes</u>
<u>Ens_3band</u>	<u>Local DA</u>	<u>No</u>	<u>Yes</u>	<u>M</u>	<u>Yes</u>
<u>Ens_5band</u>	<u>Local DA</u>	<u>No</u>	<u>Yes</u>	<u>M</u>	<u>Yes</u>
<u>Hybrid_2band</u>	<u>Local DA</u>	<u>Yes</u>	<u>Yes</u>	<u>M</u>	<u>Yes</u>
<u>Hybrid_3band</u>	<u>Local DA</u>	<u>Yes</u>	<u>Yes</u>	<u>M</u>	<u>Yes</u>
<u>Hybrid_5band</u>	<u>Local DA</u>	<u>Yes</u>	<u>Yes</u>	<u>M</u>	<u>Yes</u>
<u>Ens_noFLTR_OL</u>	<u>Local DA</u>	<u>No</u>	<u>Yes</u>	<u>O</u>	<u>Yes</u>
<u>Ens_LETKF</u>	<u>LETKF</u>	<u>No</u>	<u>Yes</u>	<u>O</u>	<u>Yes</u>
<u>Ens_noFLTR_DSL</u>	<u>Local DA</u>	<u>No</u>	<u>Yes</u>	<u>M+O</u>	<u>Yes</u>
<u>Hybrid_5band_DSL</u>	<u>Local DA</u>	<u>Yes</u>	<u>Yes</u>	<u>M+O</u>	<u>Yes</u>
<u>Ens_5band_DSL</u>	<u>Local DA</u>	<u>No</u>	<u>Yes</u>	<u>M+O</u>	<u>Yes</u>

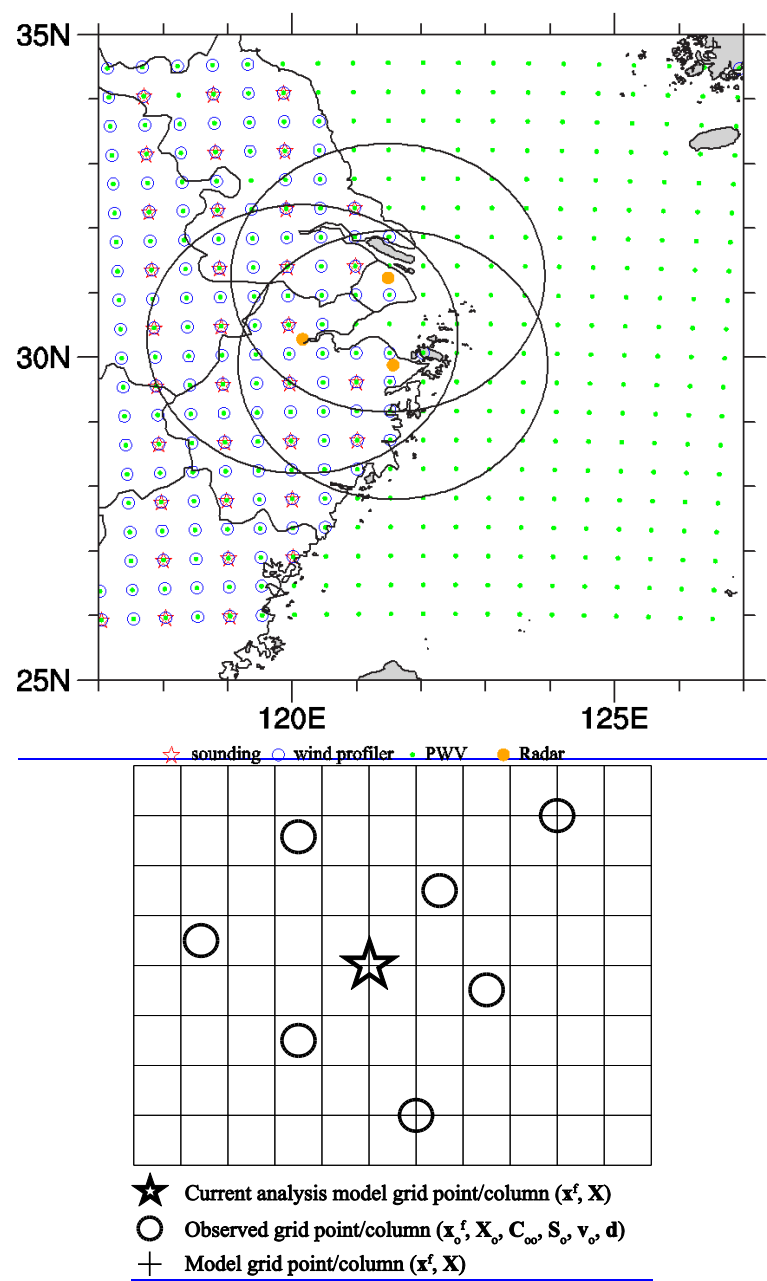


Figure 1 [The spatial distribution of different kinds of variables in Local DA](#)

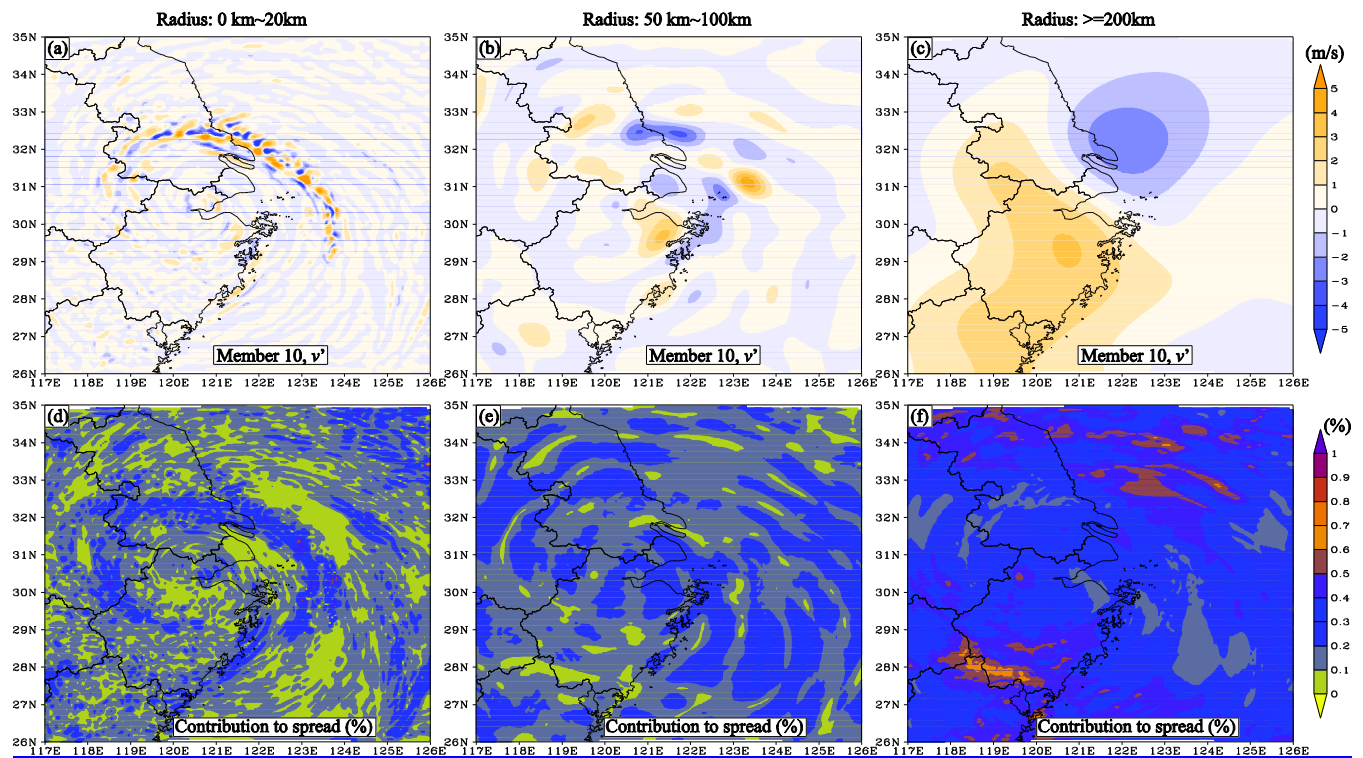


Figure 2 An example of scale decomposition for scales of (a,d) 0 km - 20 km, (b,e) 50 km – 100 km, and (c,f) greater than 200 km. The upper panels show the decomposed v perturbation (m s^{-1}), while the lower panels show the contribution of each scale to the ensemble spread in terms of percentage.

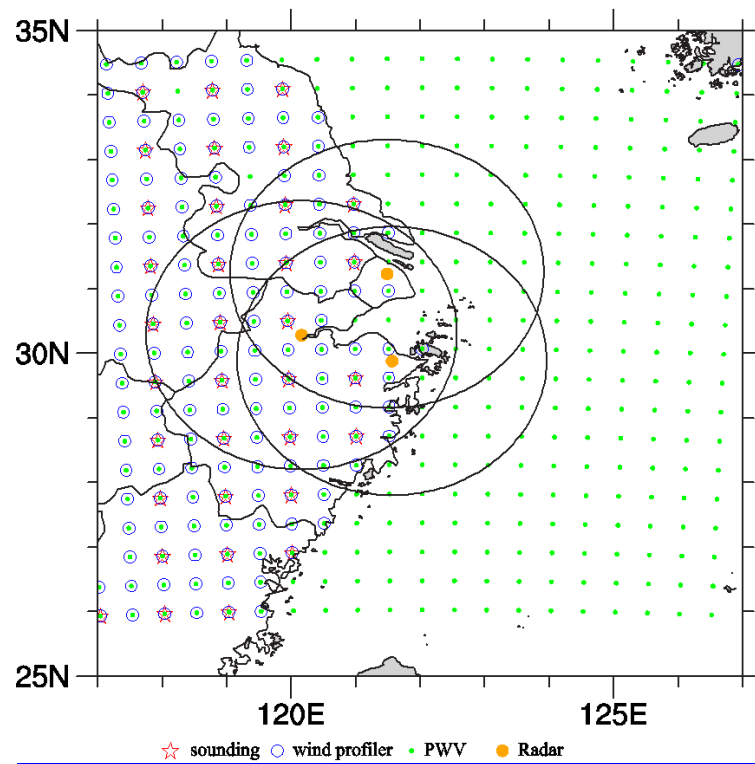
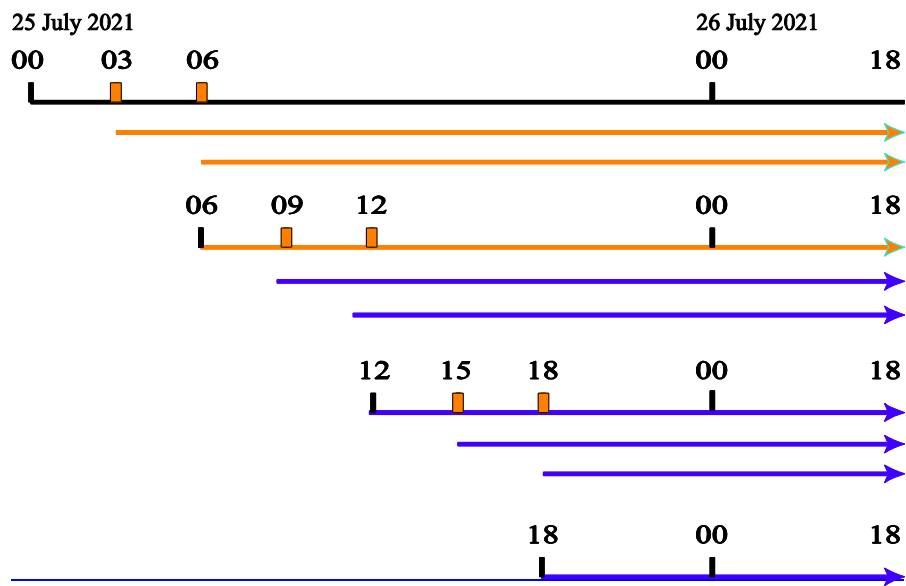


Figure 3 The distribution of simulated observations, where the black rings denote the maximum observation ranges of radars.



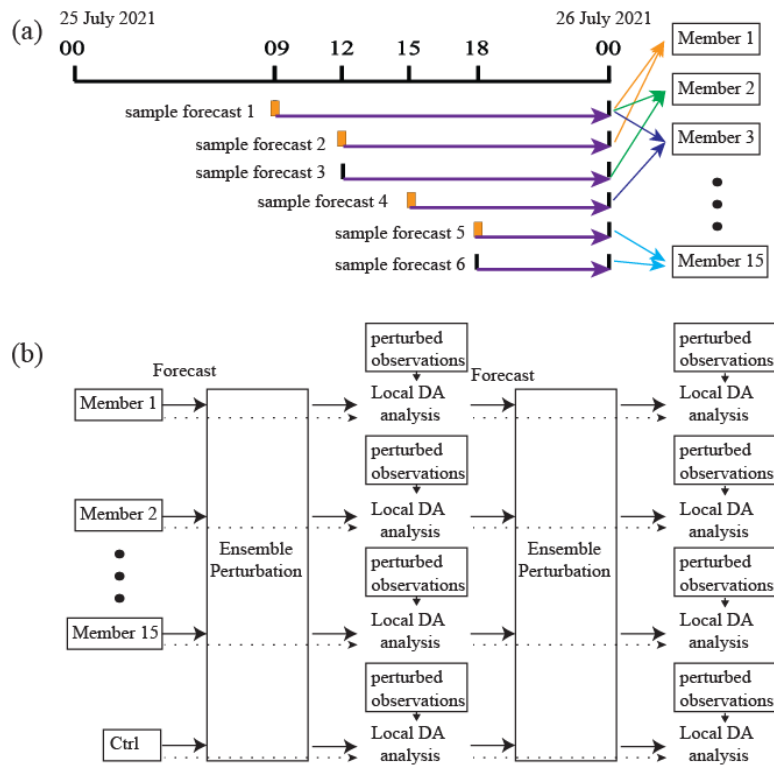


Figure 424 A(a) The flow chart of the time-lagged ensemble generation, where the colored-thick blue arrows represent the sample forecasts used by the 36-member ensemble. The 15-member ensemble excludes the forecasts shown with orange arrows. The sample forecasts initialized by using the GFS forecast data are highlighted with orange tick marks. The ensembles Sample forecasts used to form a member are available at 00 UTC, 06 UTC, 12 UTC, and 18 UTC on 26 July 2021.

1290

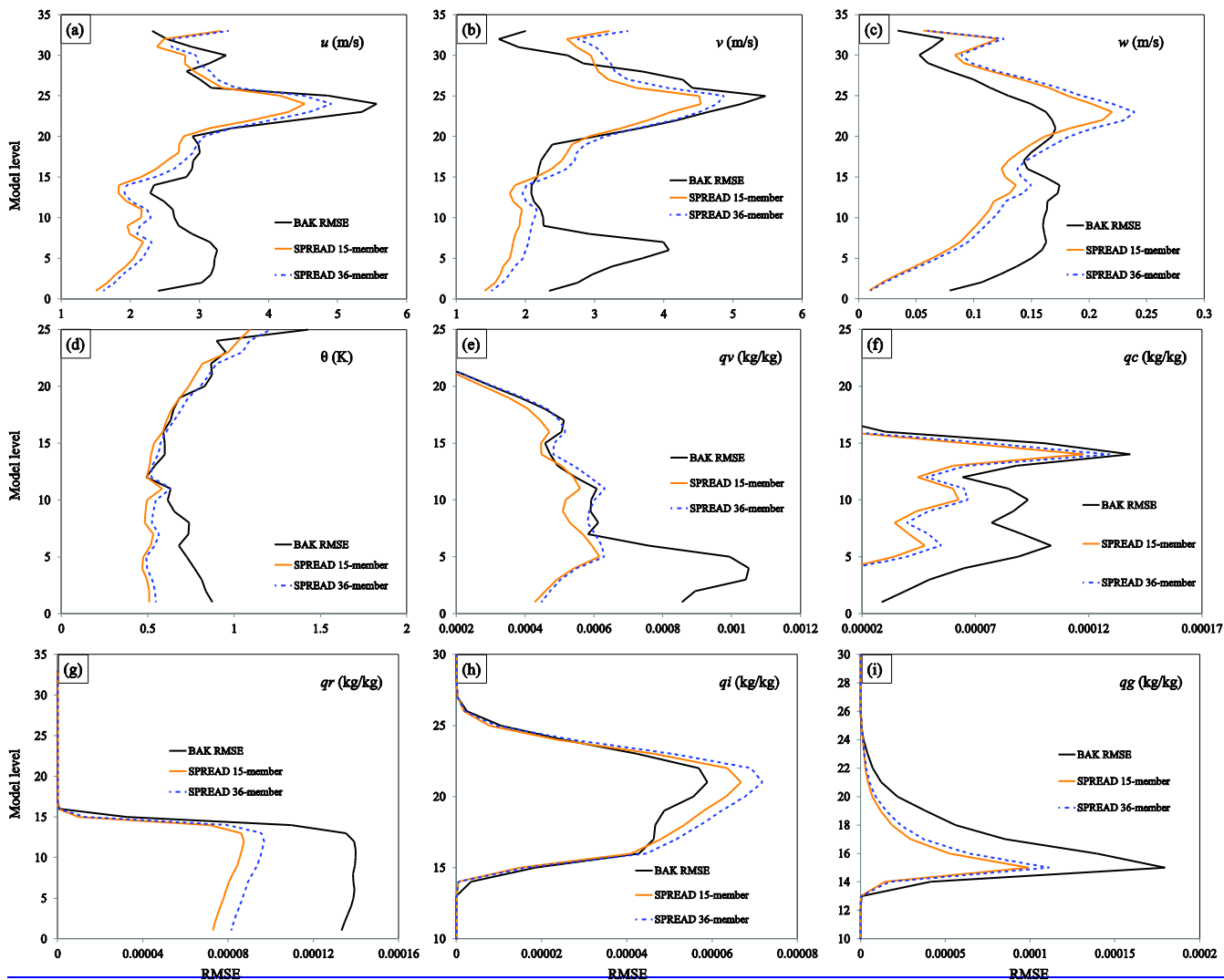
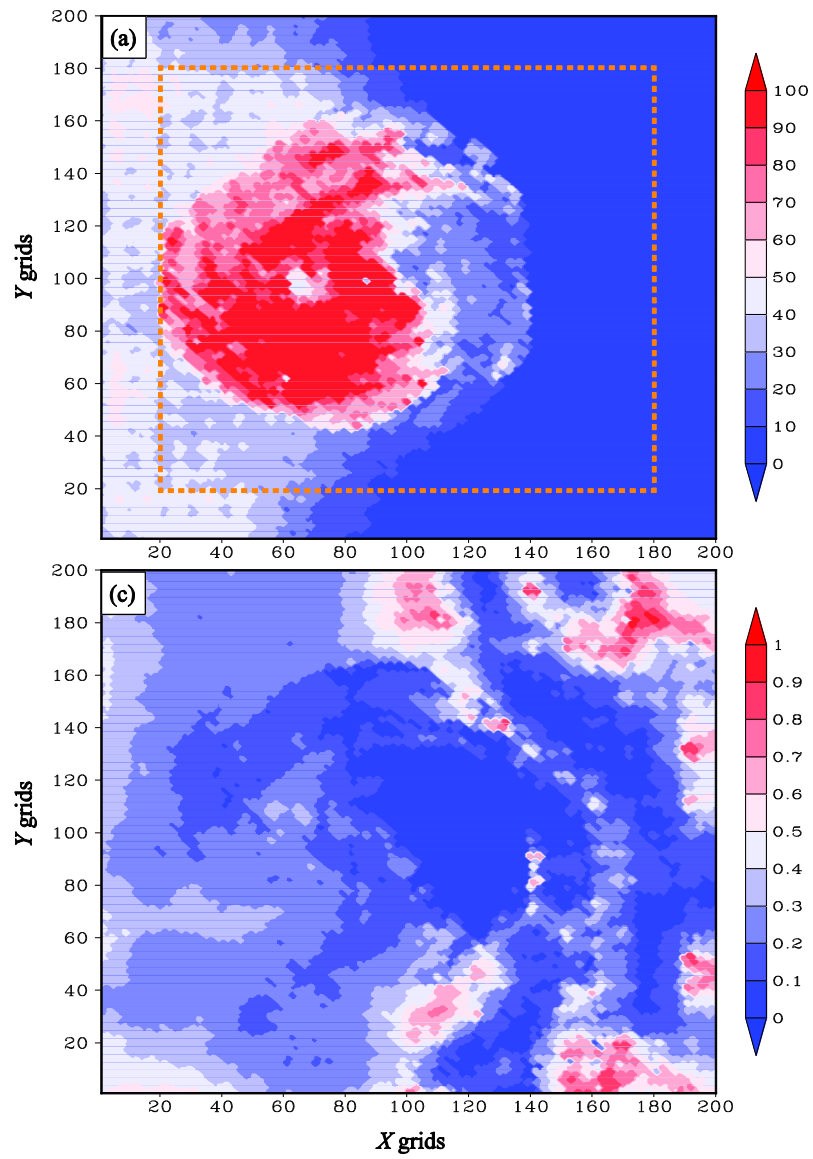
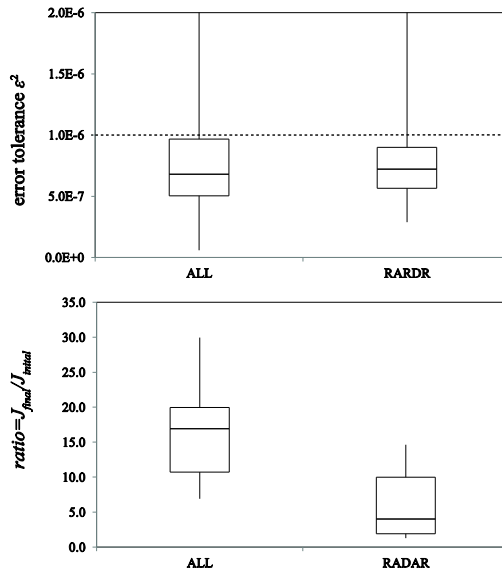


Figure 3 The ensemble spread profiles for the 15-member ensemble (orange lines) and the 36-member ensemble (dashed blue lines), where the model levels denoted by colored thin arrows. (b) The flow chart of some plots are truncated to highlight the differences. “BAK” (black lines) denotes the RMSE cycling DA. Each member assimilates the observations containing a different set of the initial condition without DA perturbations.



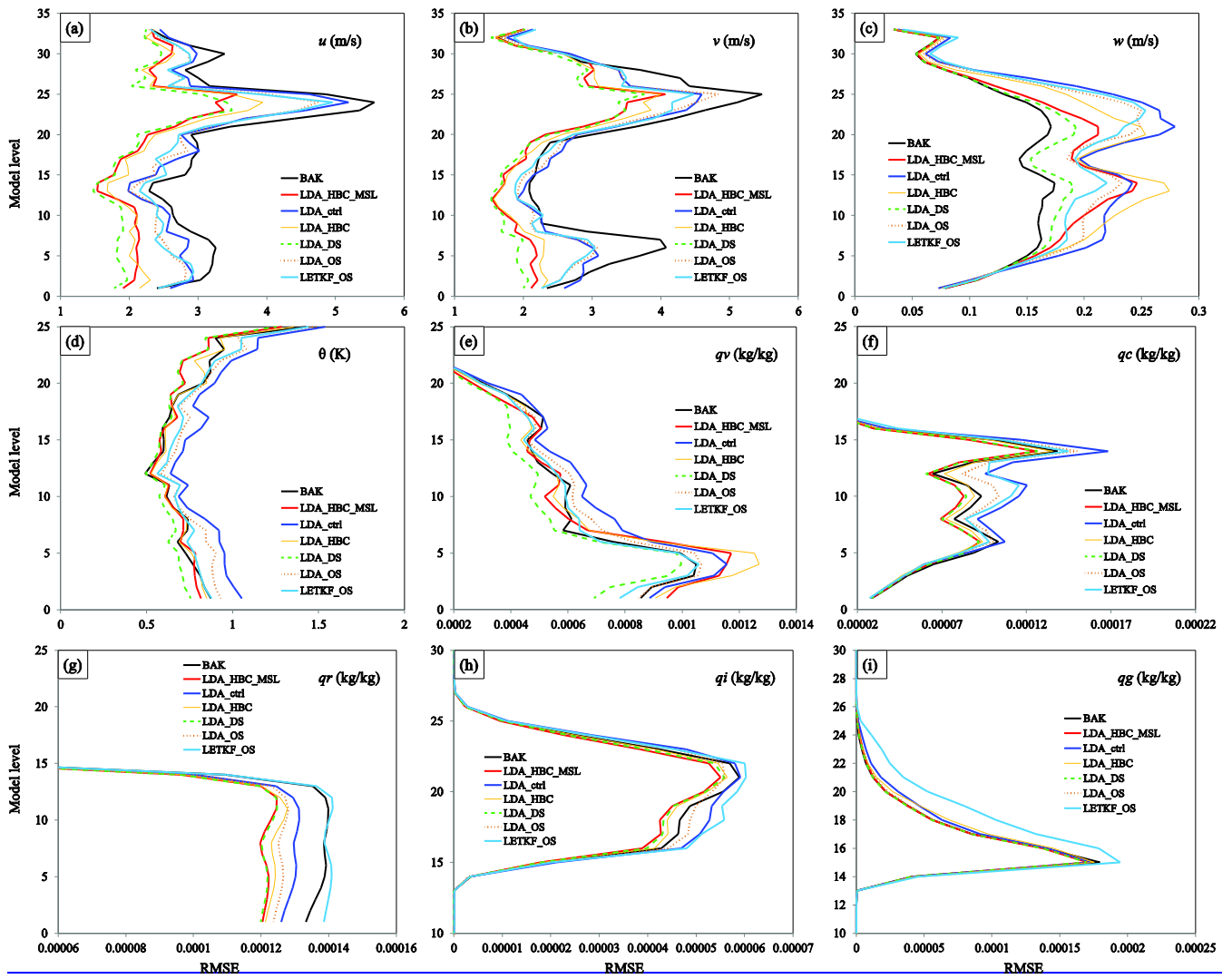
1300

Figure 545 The spatial distributions of (a) the number of iterations and (b) the ratio of the final value of the cost function to the initial value.



1305 | Figure 656 The boxplots of (a) ε^2 and (b) the ratio of the final J to the initial J in the dashed rectangle area shown in Figure 3, where “ALL” denotes the DA using all observations and “RADAR” corresponds to the DA using radar data only. The upper and lower bounds of the boxes are the 75th and 25th percentiles, respectively. The middle line indicates the median.

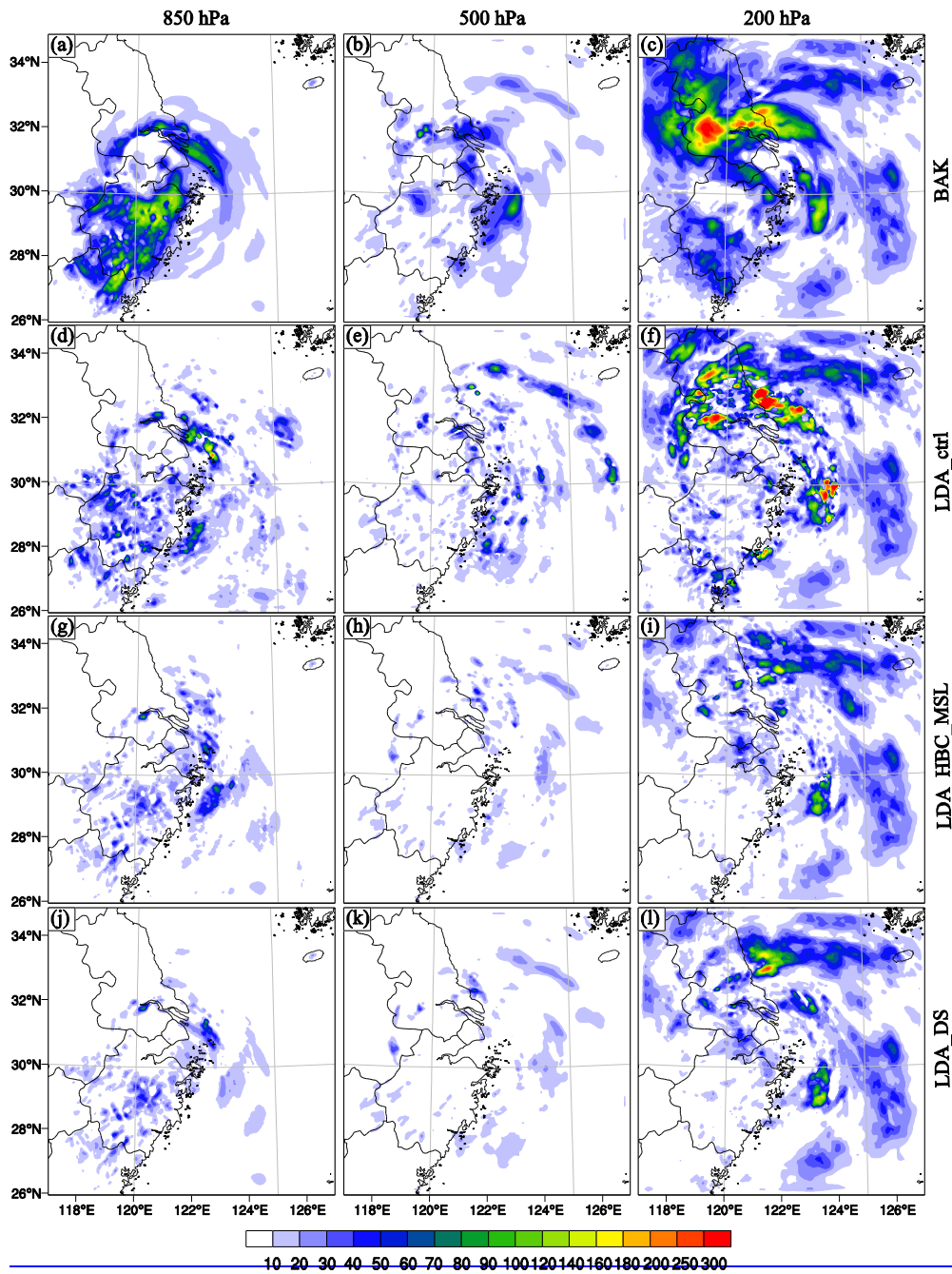
1310 |



	U(SND)	V(SND)	T	QV	PS	U(PRO)	V(PRO)	PWV	RV	RF
BAK	3.39	3.35	1.37	3.50E-04	70.19	3.16	3.42	2.03	4.43	25.70
Ens_noFLTR	1.49	1.60	1.11	1.90E-04	35.38	1.61	1.71	1.09	2.46	17.78
Static_BE	1.16	1.35	0.86	1.30E-04	39.51	1.48	1.55	0.97	2.03	14.78
Hybrid_noFLTR	0.97	1.15	0.84	1.10E-04	27.70	1.25	1.29	0.87	1.95	15.68
Ens_2band	0.72	0.79	0.87	1.00E-04	28.74	0.94	0.90	0.73	1.83	14.94
Ens_3band	0.63	0.66	0.80	8.00E-05	27.66	0.81	0.83	0.73	1.67	14.68
Ens_5band	0.64	0.67	0.81	8.00E-05	29.96	0.79	0.79	0.68	1.65	14.39
Hybrid_2band	0.74	0.86	0.74	9.00E-05	26.16	1.09	1.03	1.07	1.77	14.22
Hybrid_3band	0.71	0.79	0.73	8.00E-05	31.33	1.01	1.03	1.05	1.74	14.72
Hybrid_5band	0.80	0.86	0.79	9.00E-05	33.05	1.04	1.05	0.95	1.77	14.71
Ens_noFLTR_OL	1.58	1.73	1.10	1.90E-04	24.76	1.71	1.77	1.00	2.67	15.30
Ens_LETKF	1.82	2.04	1.04	2.10E-04	40.17	2.22	2.18	1.17	2.82	16.81
Ens_noFLTR_DSL	1.40	1.50	1.09	1.80E-04	21.99	1.47	1.53	0.95	2.41	15.45
Hybrid_5band_DSL	0.66	0.72	0.72	8.00E-05	19.42	0.88	0.90	0.53	1.74	13.25
Ens_5band_DSL	0.60	0.62	0.77	8.00E-05	18.12	0.67	0.68	0.57	1.68	12.81
	(m/s)	(m/s)	(K)	(kg/kg)	(Pa)	(m/s)	(m/s)	(mm)	(m/s)	(dBZ)

1
2
3
4
5
6
7
8
9
10
12
13
14
15

Figure 767 The RMSE analysis profiles for experiments LDA_HBC_MSL (red lines), LDA_ctrl (blue lines), LDA_HBC (thin yellow lines), LDA_DS (dashed green lines), LDA_OS (dot brown lines), and LETKF_OS (cyan lines), where the model levels of some plots are truncated to highlight the main differences among the experiments. “BAK” (black lines) denotes the initial condition without DA.



The RMSEs in observation space for all single deterministic analyses, where BAK represents the background error, SND denotes the sounding observation, and PRO corresponds to profile observation. The values of 1 and 15 in the legend represent the smallest and the largest error among all experiments, respectively.

	U	V	T	QV	W	QC	QR	QI	QS	QG	PS	
BAK	3.24	3.19	1.32	5.25E-04	0.14	5.71E-05	8.87E-05	2.54E-05	8.46E-05	4.47E-05	82.07	
Ens_noFLTR	2.98	2.90	1.47	5.85E-04	0.20	6.72E-05	8.31E-05	2.70E-05	8.32E-05	4.49E-05	103.62	
Static_BE	2.39	2.57	1.23	5.72E-04	0.19	5.71E-05	7.87E-05	2.54E-05	8.19E-05	4.44E-05	55.77	
Hybrid_noFLTR	2.40	2.49	1.28	5.75E-04	0.19	5.50E-05	7.98E-05	2.43E-05	8.24E-05	4.63E-05	80.76	1
Ens_2band	2.49	2.56	1.36	5.19E-04	0.16	5.62E-05	7.98E-05	2.41E-05	8.07E-05	4.30E-05	65.92	2
Ens_3band	2.36	2.47	1.35	5.50E-04	0.15	5.35E-05	7.94E-05	2.36E-05	7.97E-05	4.31E-05	58.69	3
Ens_5band	2.35	2.44	1.35	5.77E-04	0.15	5.29E-05	7.80E-05	2.33E-05	7.96E-05	4.30E-05	58.24	4
Hybrid_2band	2.31	2.39	1.29	6.44E-04	0.18	5.30E-05	7.63E-05	2.39E-05	8.08E-05	4.31E-05	55.40	5
Hybrid_3band	2.25	2.35	1.27	6.33E-04	0.18	5.26E-05	7.60E-05	2.32E-05	8.08E-05	4.35E-05	51.48	6
Hybrid_5band	2.27	2.34	1.28	6.14E-04	0.18	5.21E-05	7.59E-05	2.31E-05	8.07E-05	4.31E-05	48.18	7
Ens_noFLTR_OL	2.83	2.84	1.39	5.44E-04	0.18	6.08E-05	8.11E-05	2.56E-05	8.24E-05	4.41E-05	53.00	8
Ens_LETKF	2.85	2.80	1.41	5.16E-04	0.18	6.24E-05	9.00E-05	2.76E-05	9.30E-05	5.81E-05	54.53	9
Ens_noFLTR_DSL	2.81	2.82	1.42	5.42E-04	0.19	6.53E-05	8.06E-05	2.66E-05	8.17E-05	4.39E-05	67.51	10
Hybrid_5band_DSL	2.15	2.26	1.21	4.83E-04	0.16	5.23E-05	7.54E-05	2.35E-05	8.01E-05	4.25E-05	49.72	11
Ens_5band_DSL	2.26	2.40	1.29	5.08E-04	0.15	5.31E-05	7.66E-05	2.35E-05	7.94E-05	4.26E-05	52.78	12
	(m/s)	(m/s)	(K)	(kg/kg)	(m/s)	(kg/kg)	(kg/kg)	(kg/kg)	(kg/kg)	(kg/kg)	(Pa)	13
												14
												15

Figure 878 As in Figure 7, but for the RMSEs in model space.

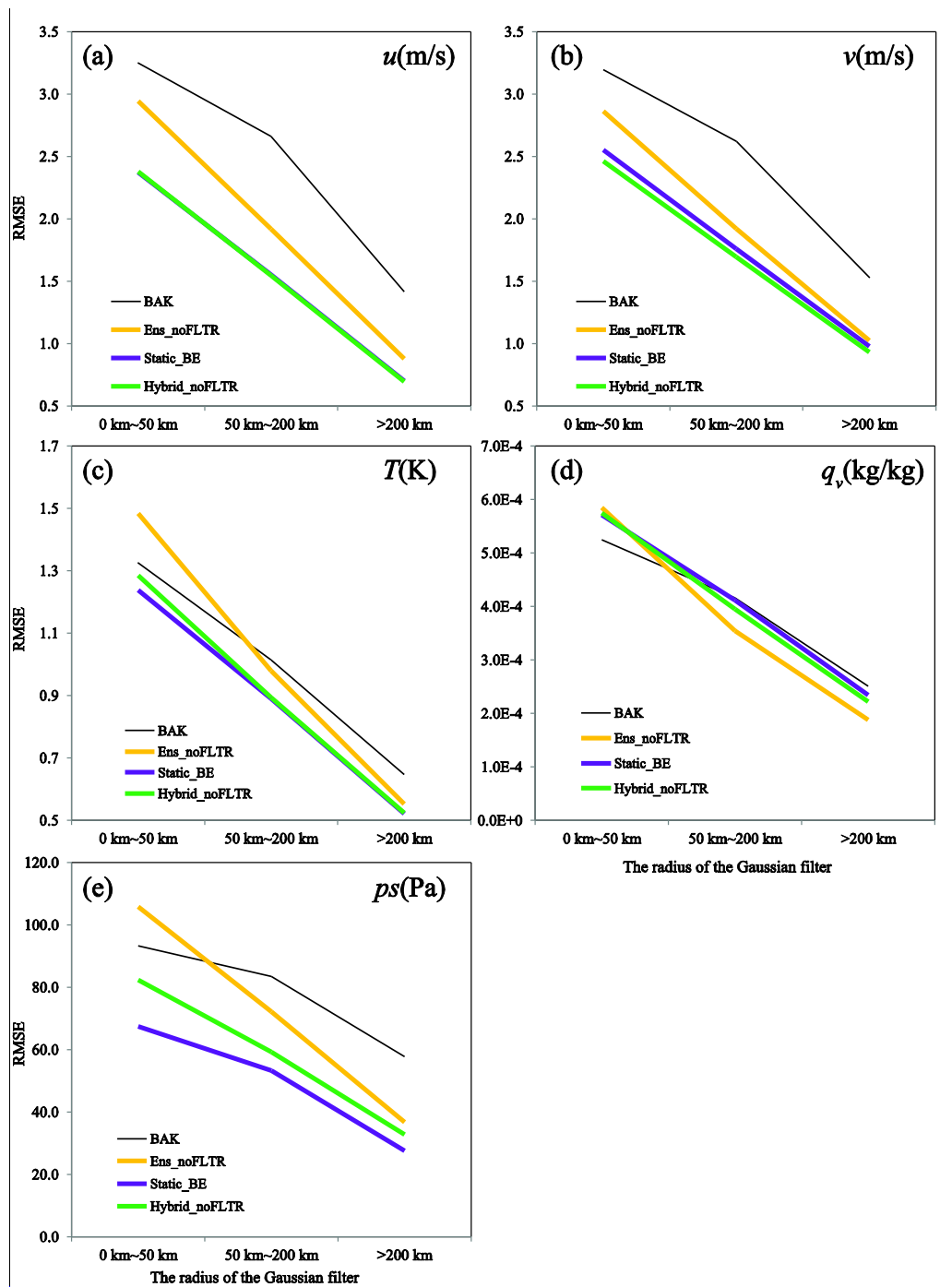


Figure 9 The analysis error decomposed into scales of 0 km - 50 km, 50 km – 200 km, and greater than 200 km (shown on the x-axis), where BAK represents the initial condition before DA.

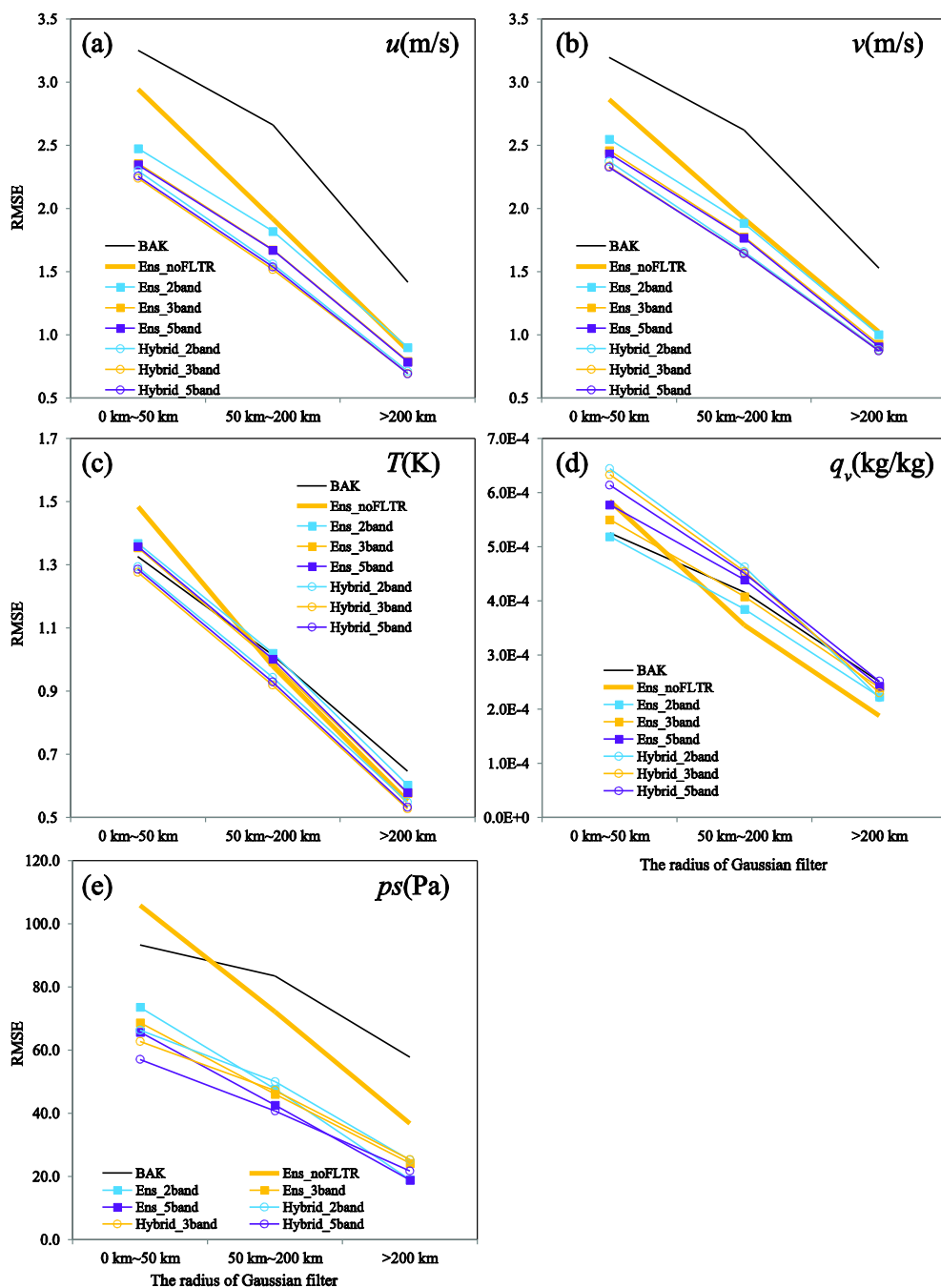


Figure 10 As in **Figure 9**, but for Ens 2band, Ens 3band, Ens 5band, Hybrid 2band, Hybrid 3band, and Hybrid 5band, where BAK and Ens noFLTR are duplicated for comparison.

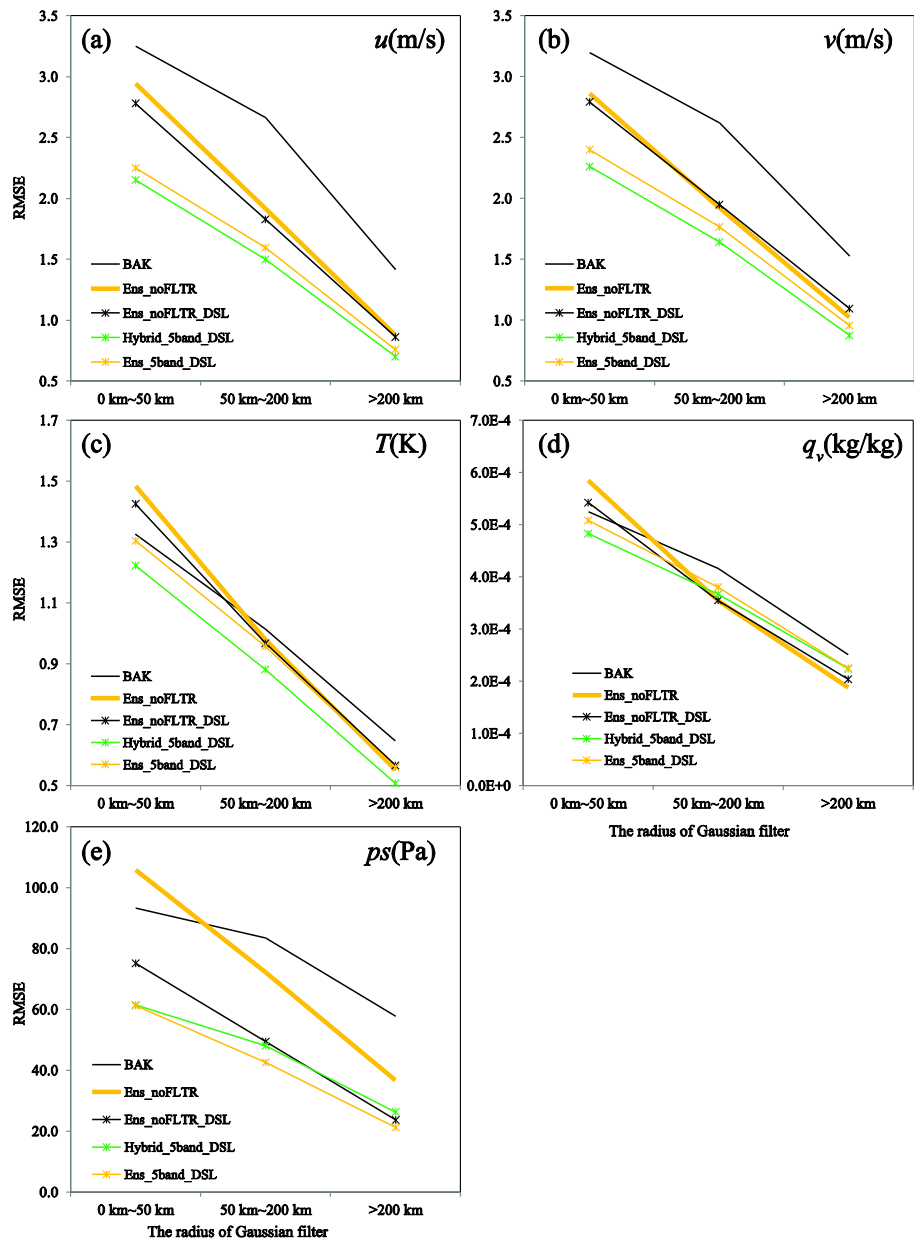


Figure 11 As in **Figure 9**, but for Ens_noFLTR_DSL, Hybrid_5band_DSL, and Ens_5band_DSL, where BAK and Ens_noFLTR are duplicated for comparison.

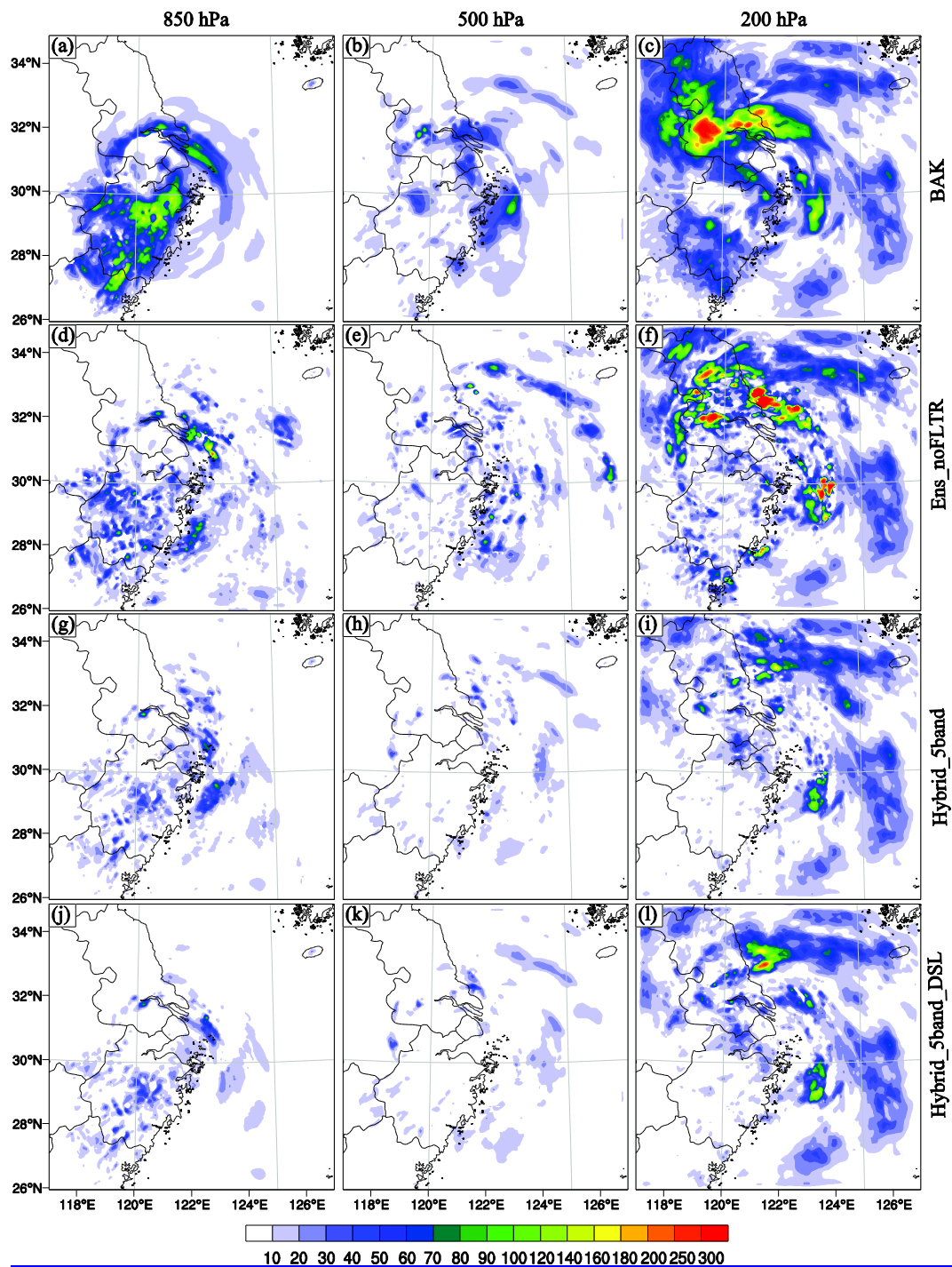
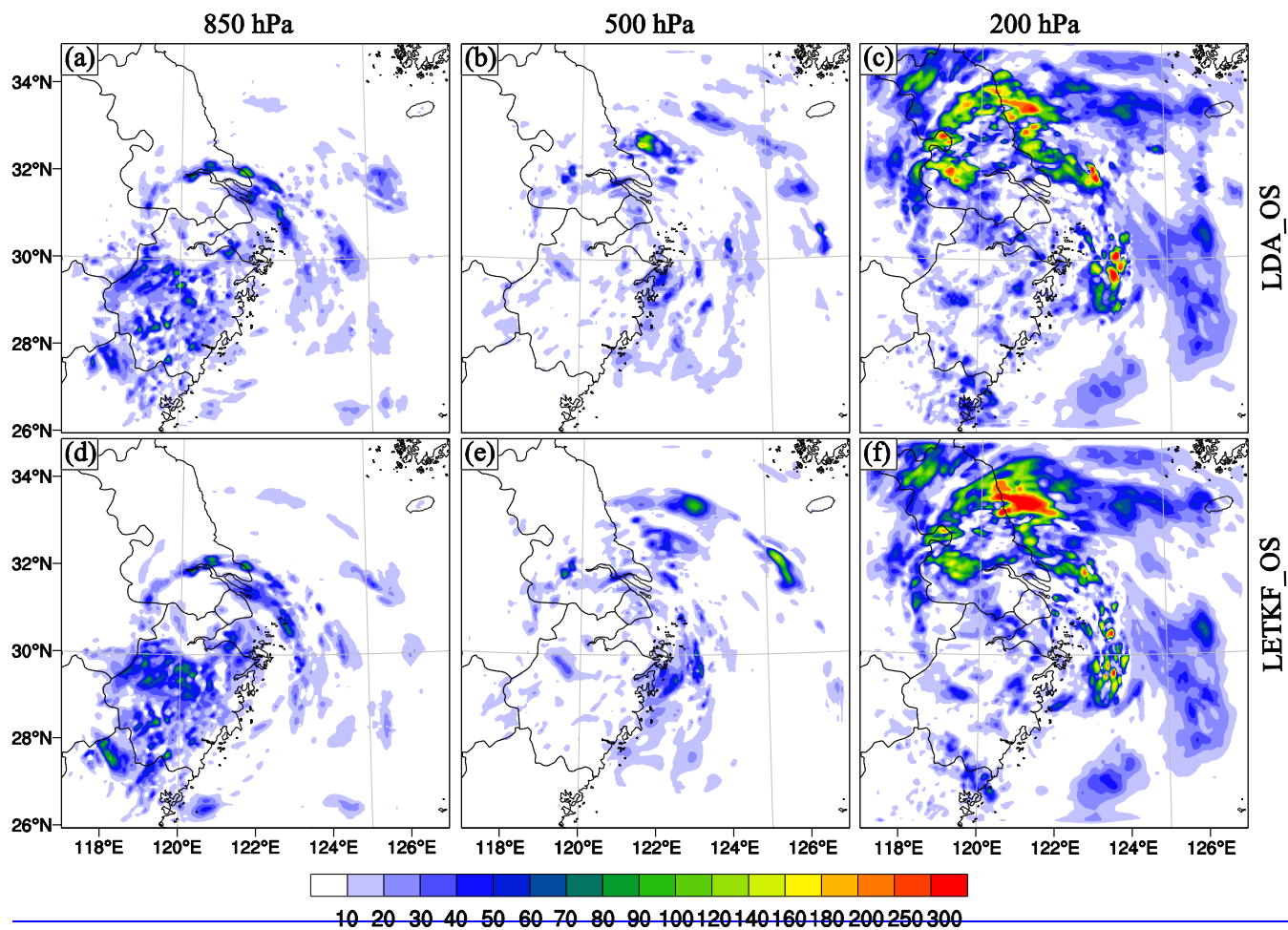


Figure 12 The DTE at 850 hPa (left column), 500 hPa (middle column), and 200 hPa (right column) for (a-c) BAK, (d-f) LDA_etrEns_noFLTR, (g-i) LDA_HBC_MSLHybrid_5band, and (j-l) LDA_DSHybrid_5band DSL.



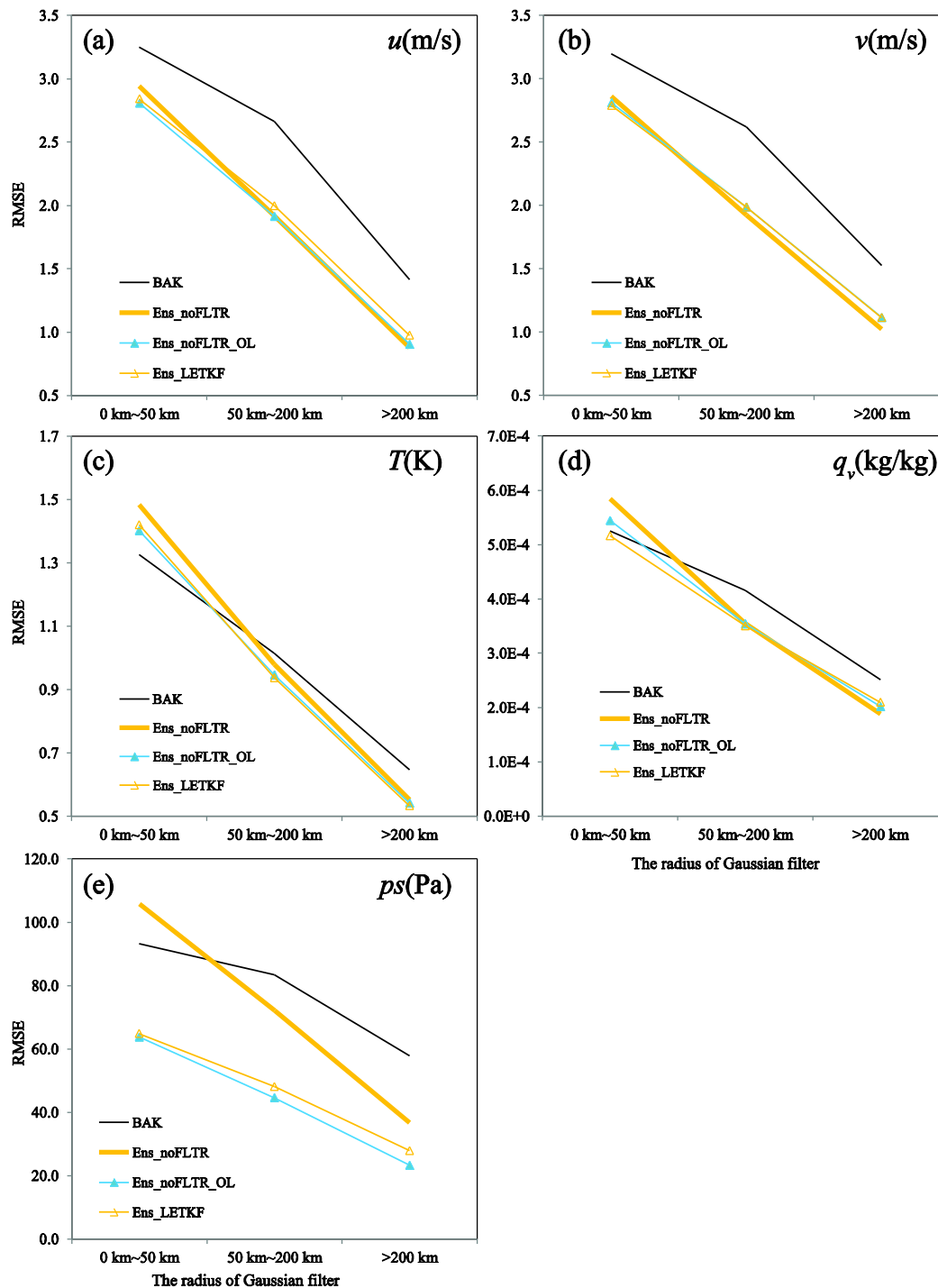
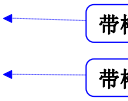
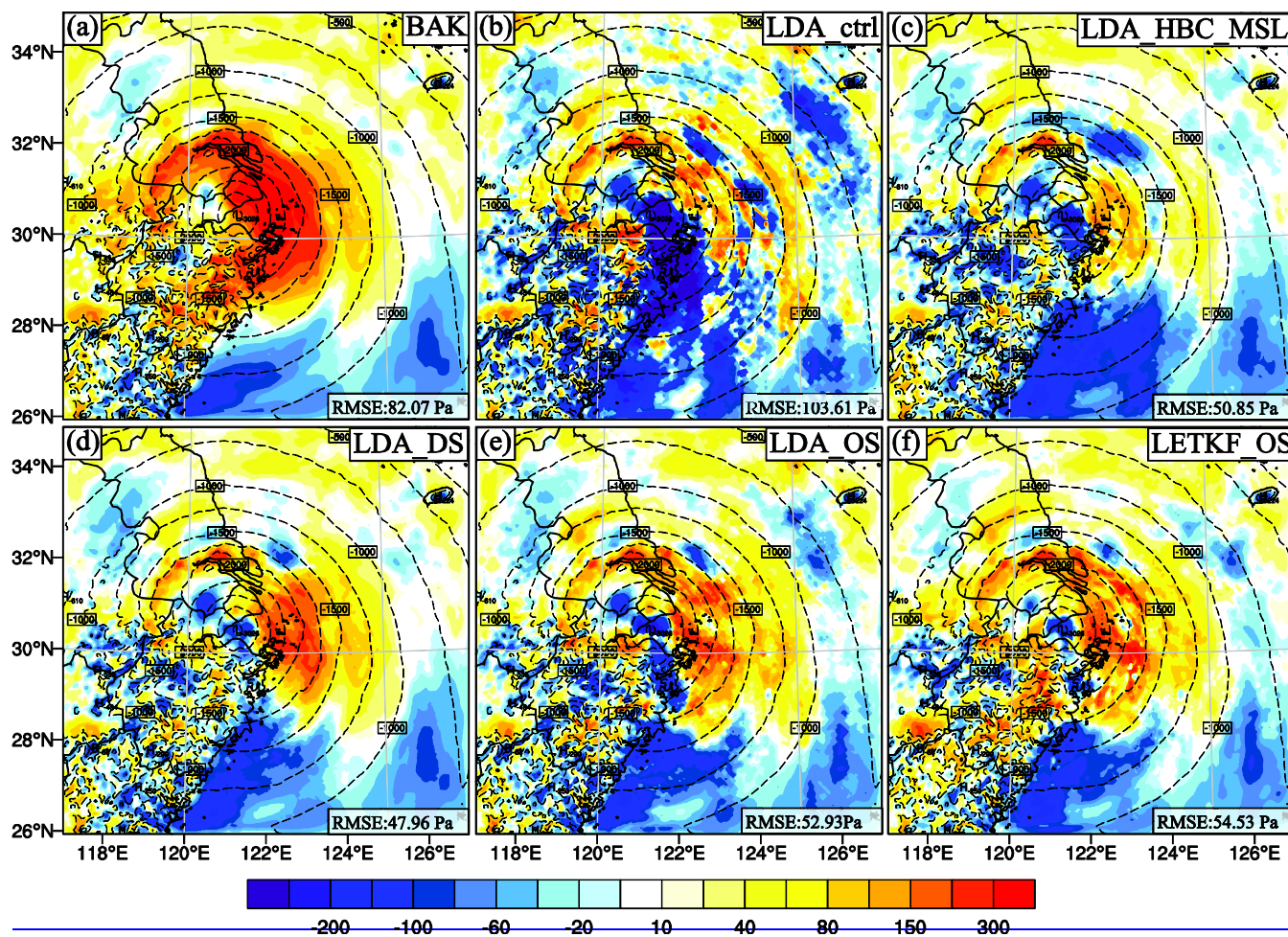


Figure 13813 The same as As in Figure 7 Figure 9, but for (a-e) LDA_OSEns_noFLTR_OL and (d-f) Ens_LETKF_OS, where BAK and Ens_noFLTR are duplicated for comparison.

1365 |





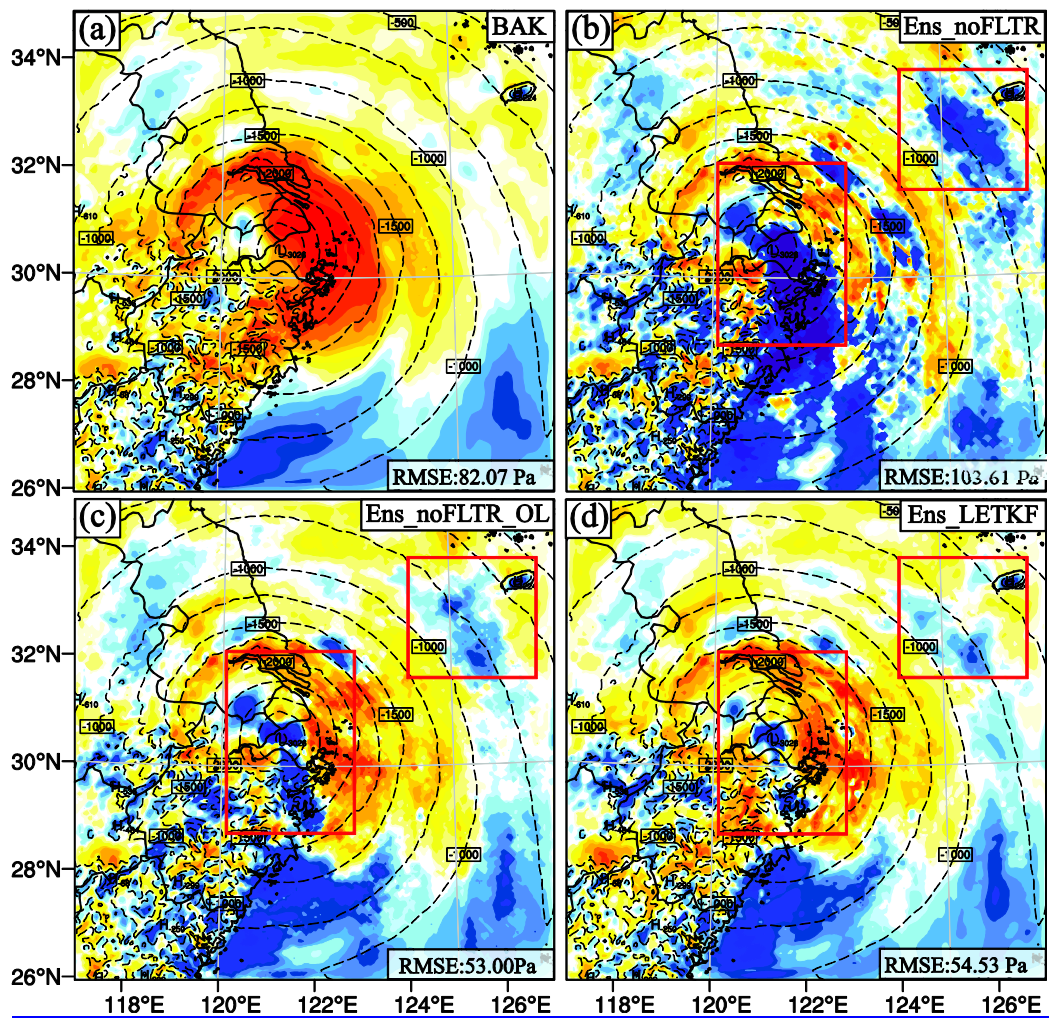
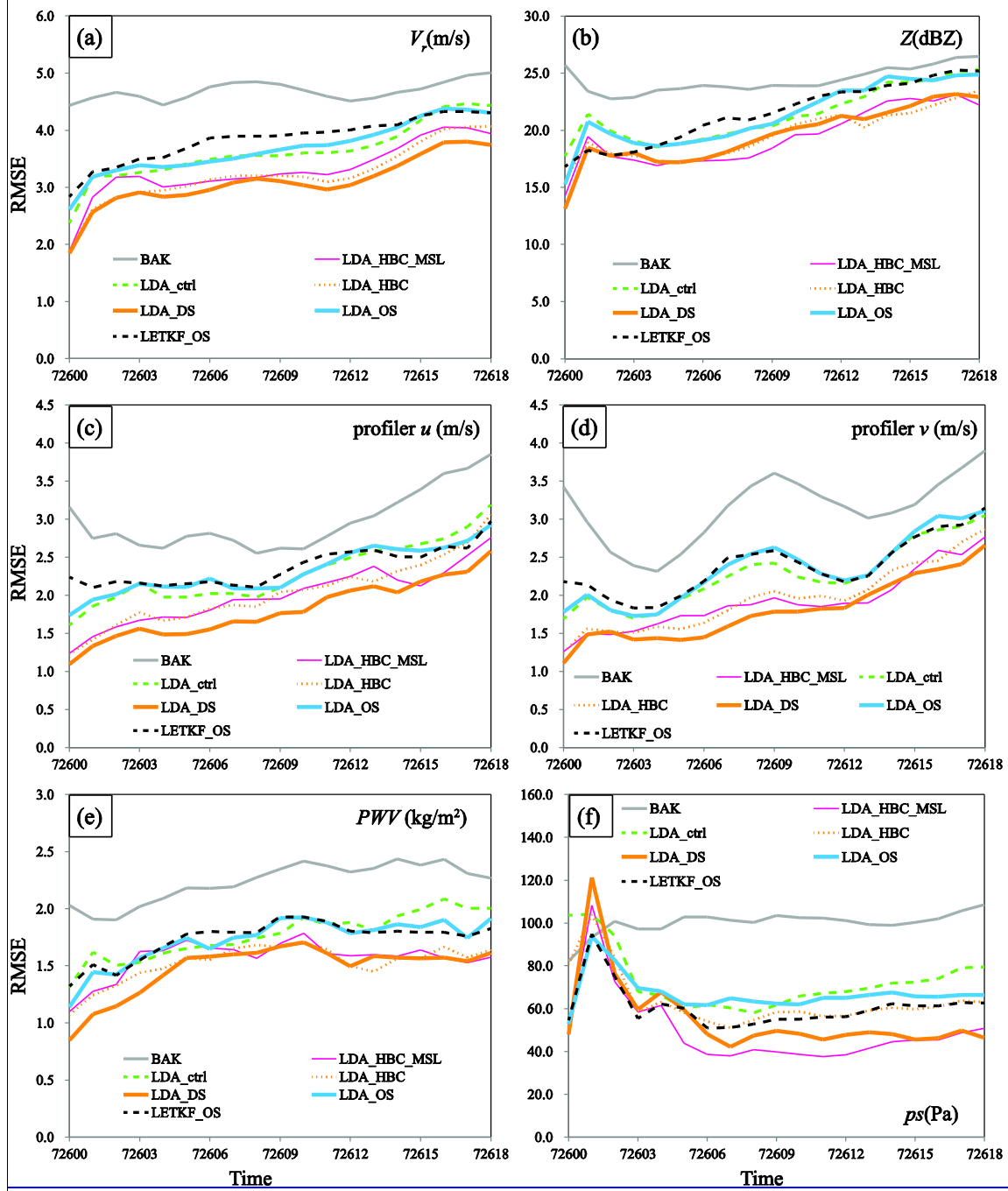


Figure 14914 The difference in the dry-air mass in column (μ) between the truth (contours) and analysis (shading) for (a) BAK, (b) LDA_ctrl, (c) LDA_HBC_MSL, (d) LDA_DS, (e) LDA_OS, and (f) Ens noFLTR OL, and (c) Ens LETKF_OS, where rectangles highlight the areas where Ens noFLTR OL and Ens LETKF analyses are similar



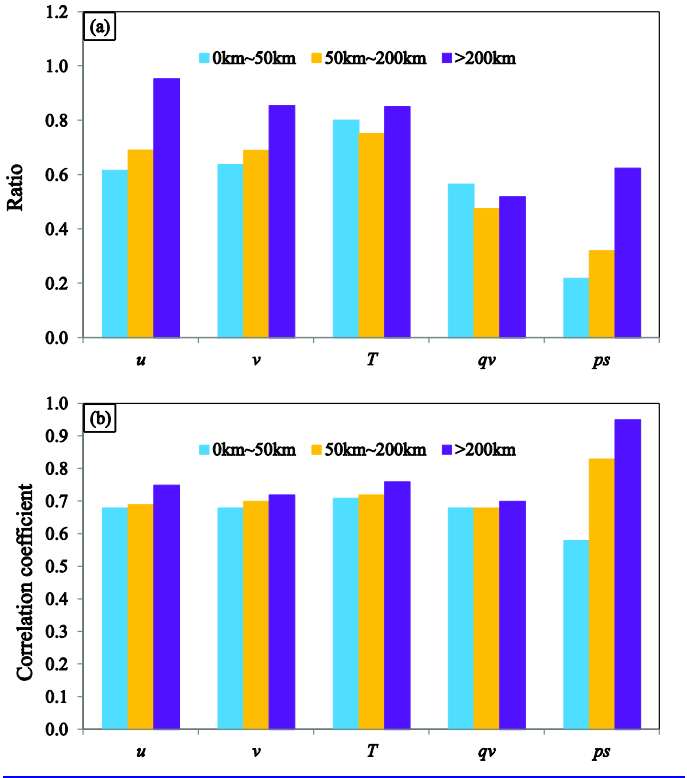
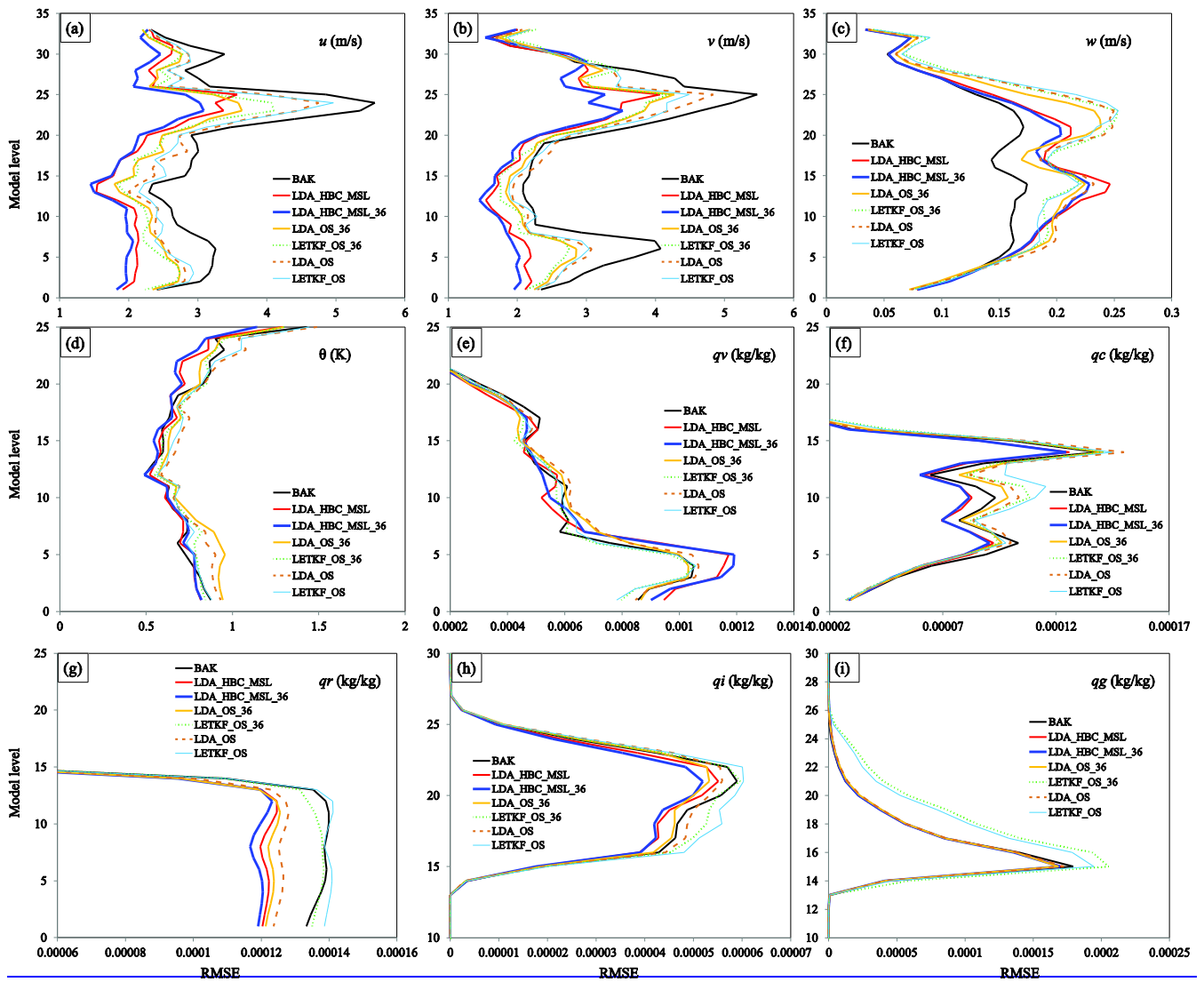


Figure 151015 The evolutions of the forecast RMSEs in terms of the (a) radial velocity, (b) reflectivity, (c) u component (wind profiler), (d) v component (wind profiler), (e) PWV , and (f) ps for BAK (gray lines), LDA_HBC_MSL (thin magenta lines), LDA_ctrl (dashed green lines), LDA_HBC (dot red lines), LDA_DS (thick orange lines), LDA_OS (cyan lines), and LETKF_OS (dashed black lines).



(a) The ratio of ensemble spread to RMSE at 00 UTC on 26 July 2021 and (b) the spatial correlation coefficient between ensemble spread and RMSE for scales of 0 km - 50 km, 50 km – 200 km, and greater than 200 km.

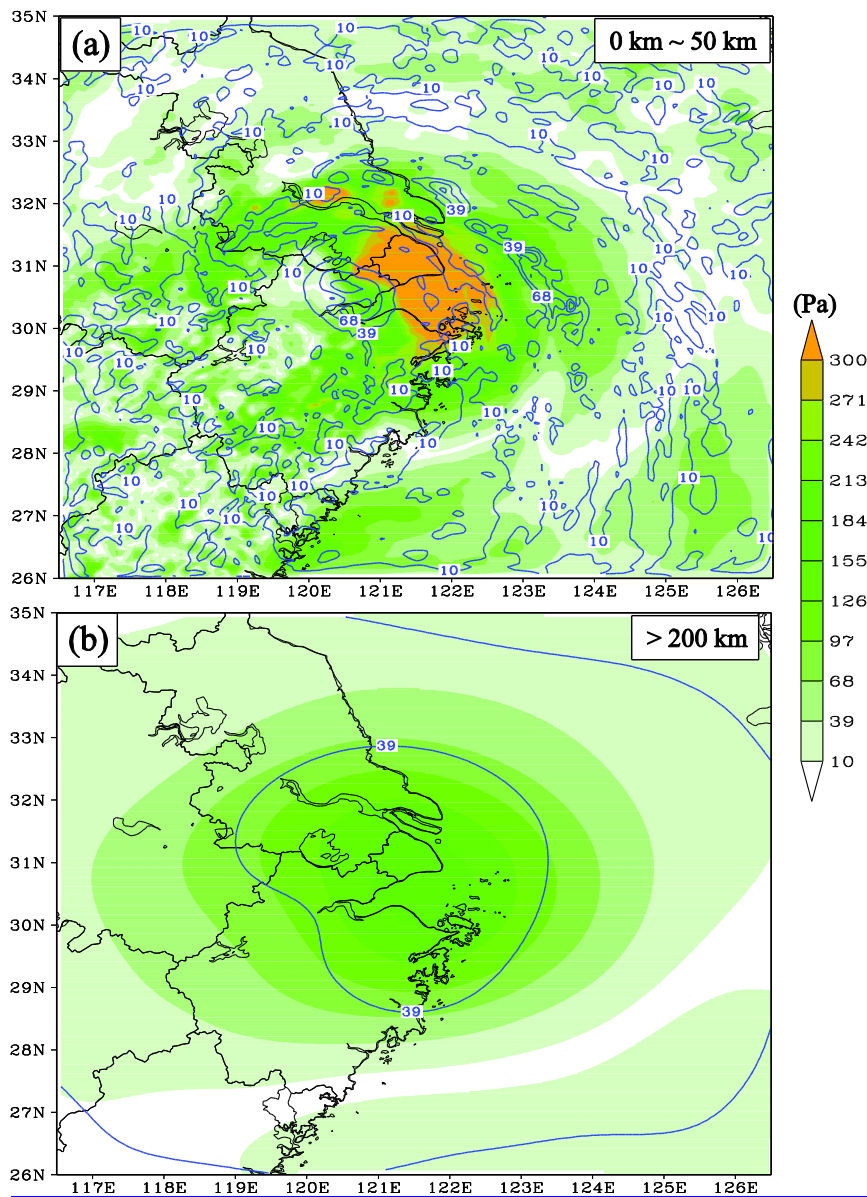
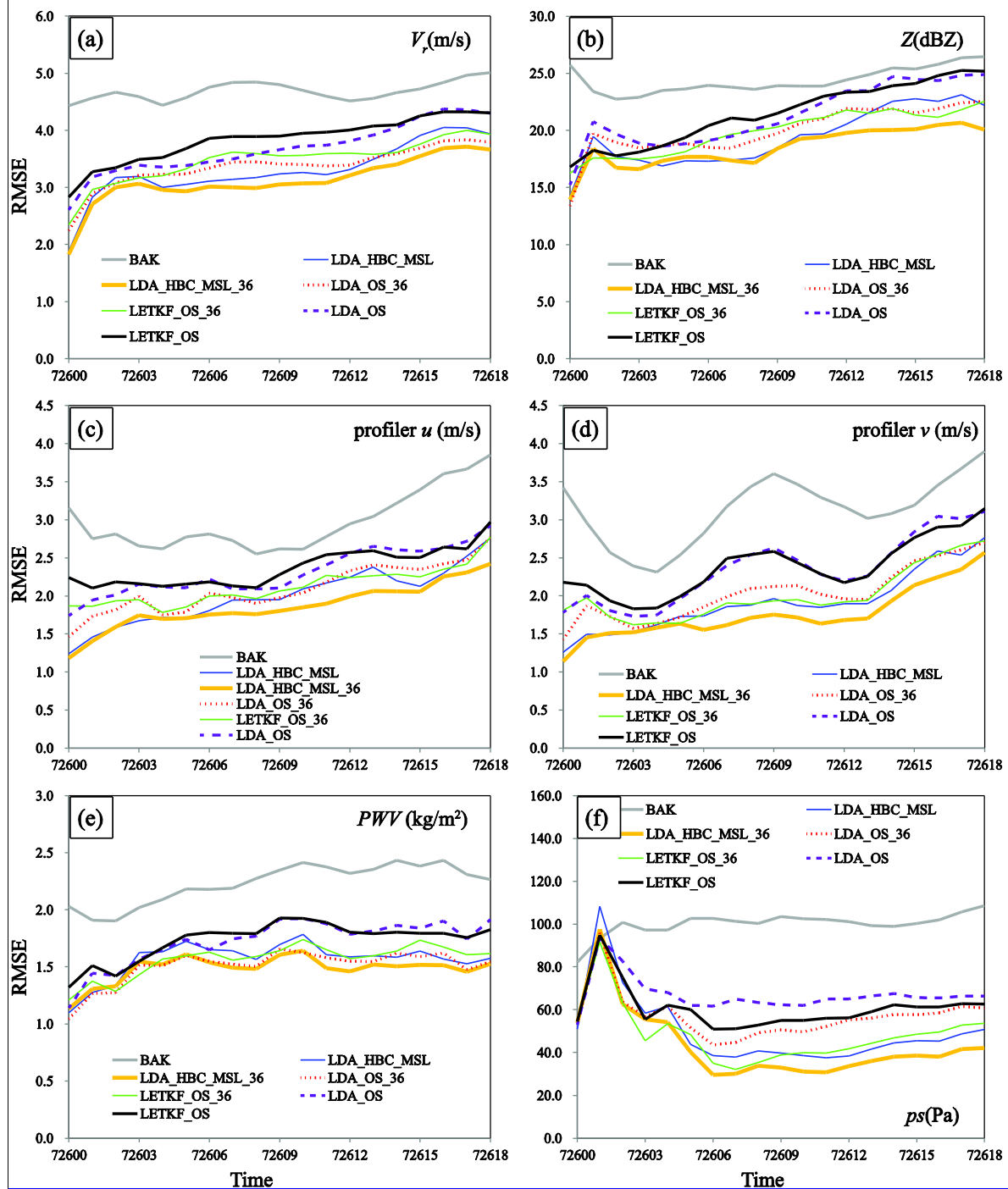


Figure 164116 The same as in Figure 6 but for LDA HBC_MSL_36m (blue lines), LDA_OS_36m (orange lines), and LETKF_OS_36m (dot green lines). The results of BAK, LDA_HBC_MSL, LDA_OS, and LETKF_OS are plotted for comparison.



The RMSE (shaded) and ensemble spread (contours) of ps decomposed into scales of (a) 0 km-50 km and (b) greater than 200 km

1410

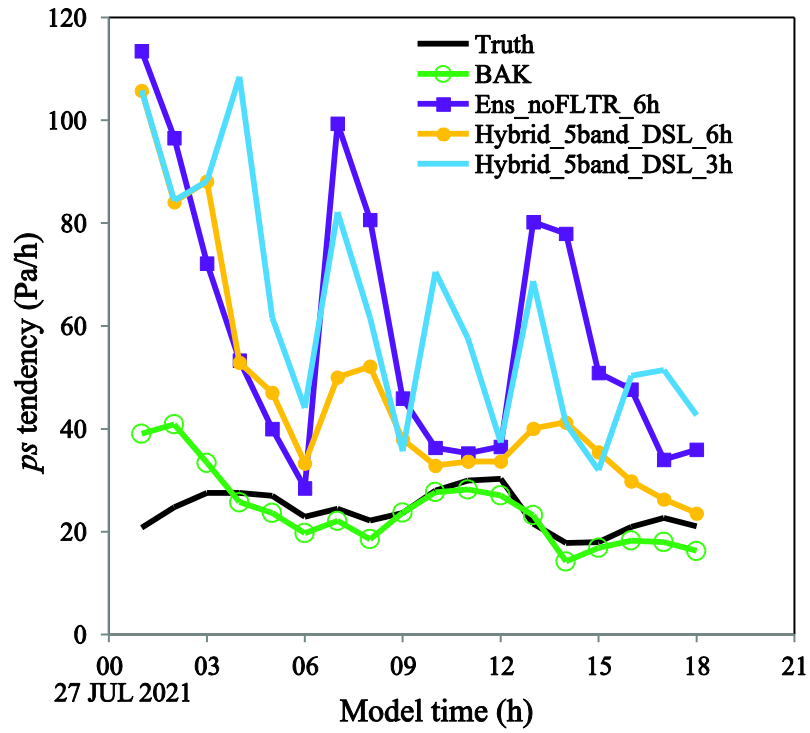


Figure 17 The tendency of surface pressure (Pa h^{-1}) for Truth (black), BAK (green), Ens_noFLTR (blue), Hybrid_5band_DSL_6h (orange), and Hybrid_5band_DSL_3h (light blue)

1415

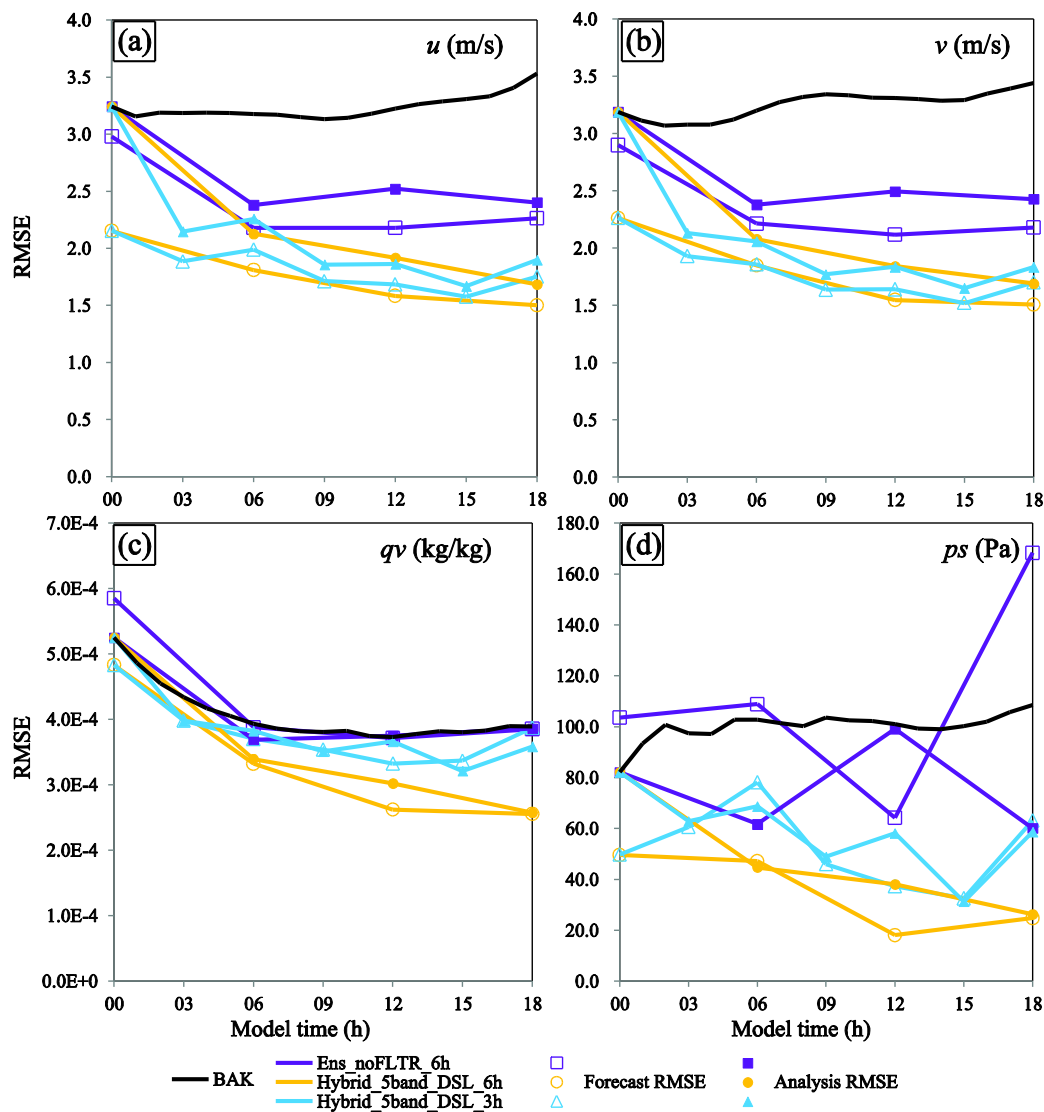


Figure 18 shows the evolution of RMSE for u (m/s), v (m/s), qv (kg/kg), and ps (Pa). The x-axis for all plots is Model time (h) from 00 to 18. The y-axis is RMSE. The legend indicates: BAK (black line), Ens_noFLTR_6h (blue line), Hybrid_5band_DSL_6h (orange line), LDA_OS_36m (dashed red line), LETKF_OS_36m (thin green line), Forecast RMSE (solid markers), and Analysis RMSE (hollow markers).

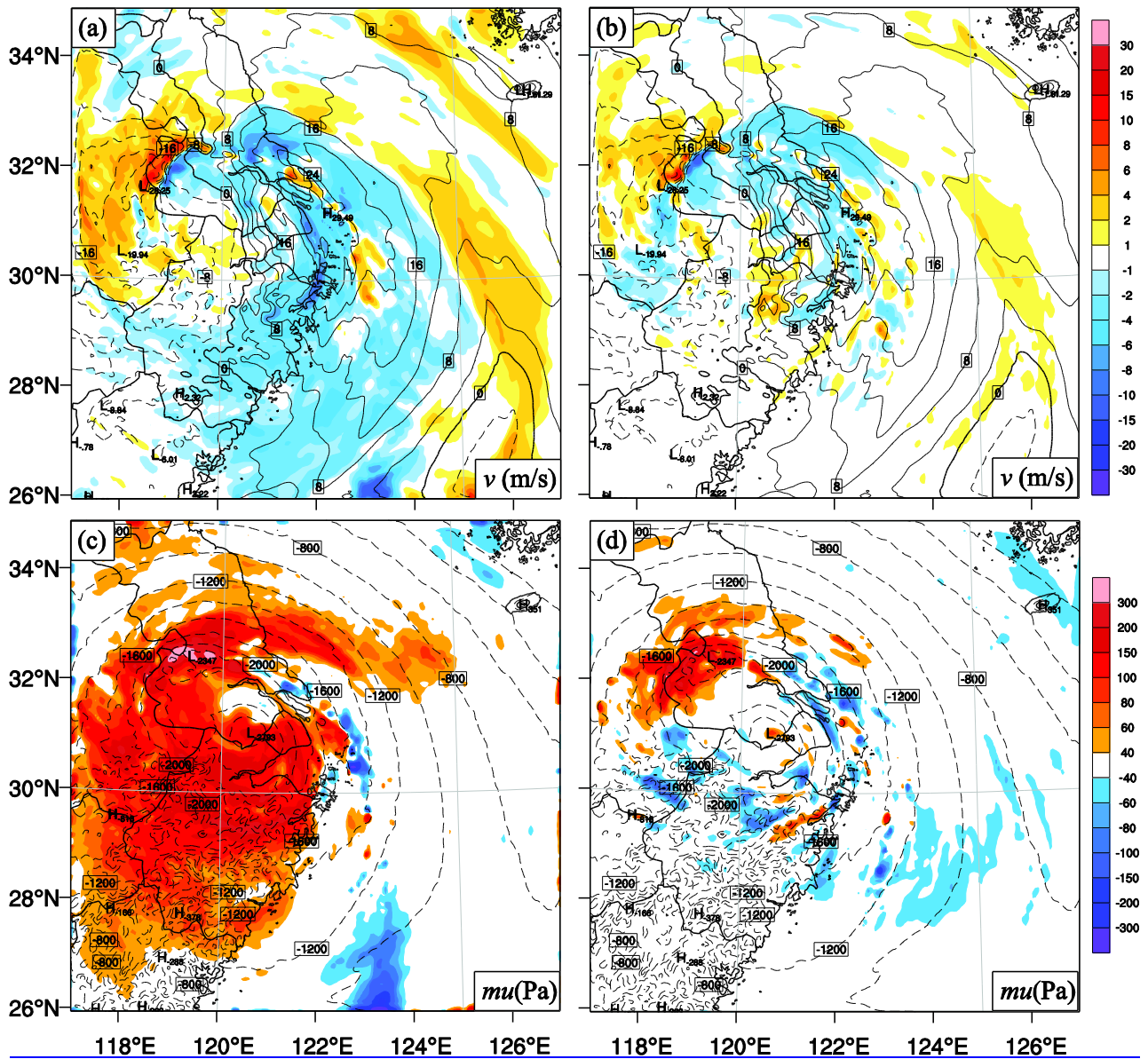
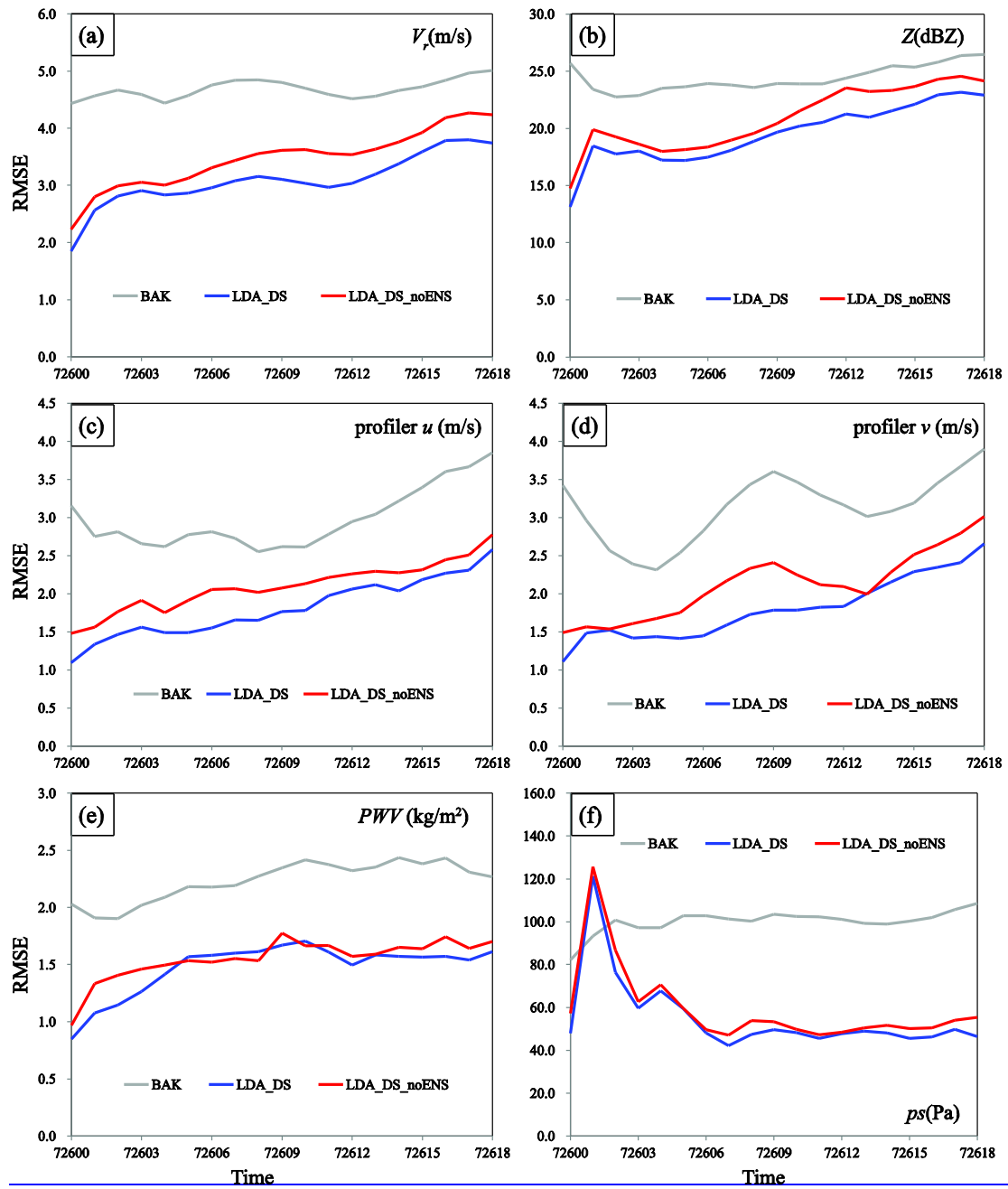


Figure 19 The results of BAK, LDA-HBC-MSL, LDA-OS, difference in (a, b) meridional wind and LETKF-OS are plotted (c, d) the dry-air mass in column (μ) between the truth (contours) and forecast (shading) at 18 UTC 26 July 2021 (the last analysis cycle) for reference (a, c) Ens noFLTR 6h and (b, d) Hybrid 5band DSL 6h.



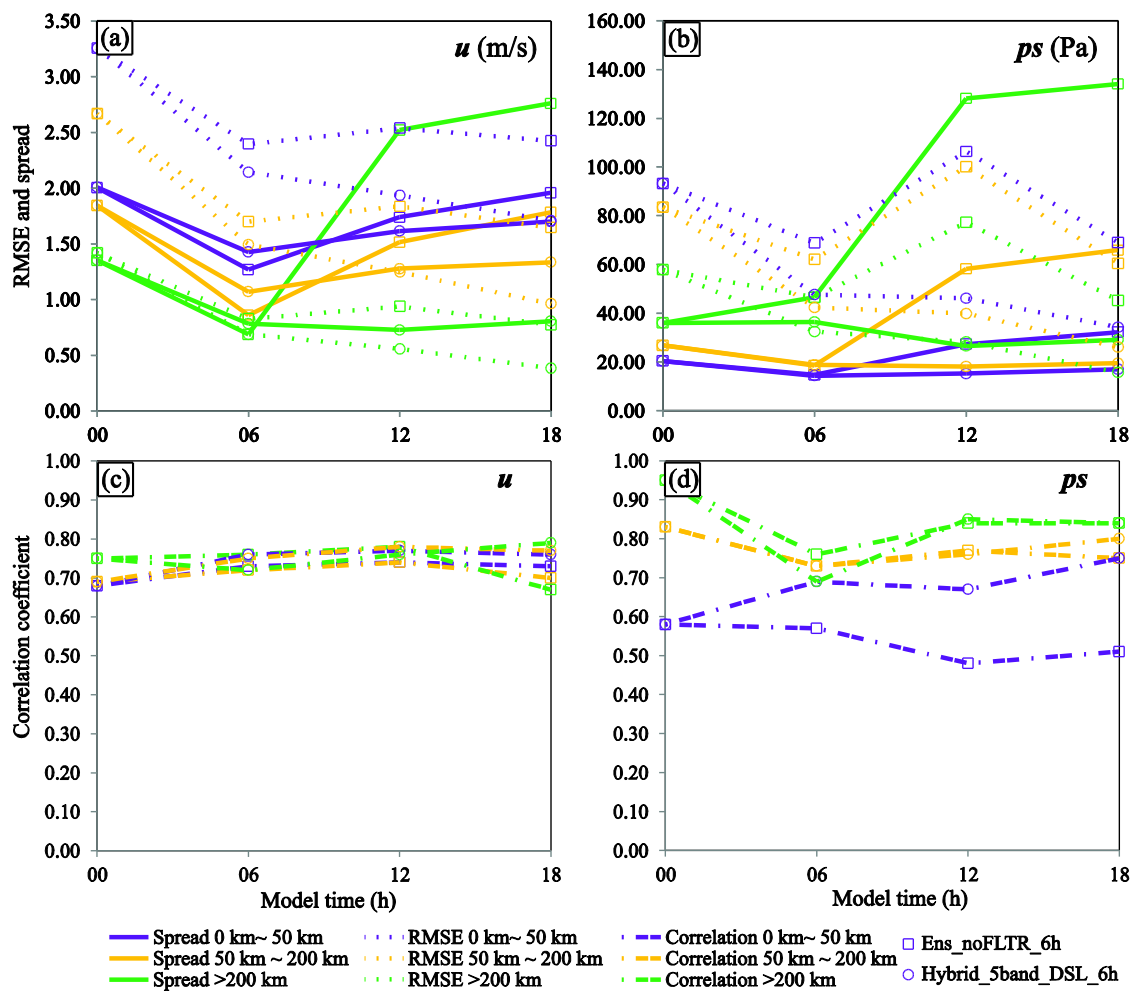


Figure 201320 The same as in Figure 10 but to compare LDA_DS_noENS (red lines) and LDA_DS (blue lines). The result of BAK is plotted for reference.

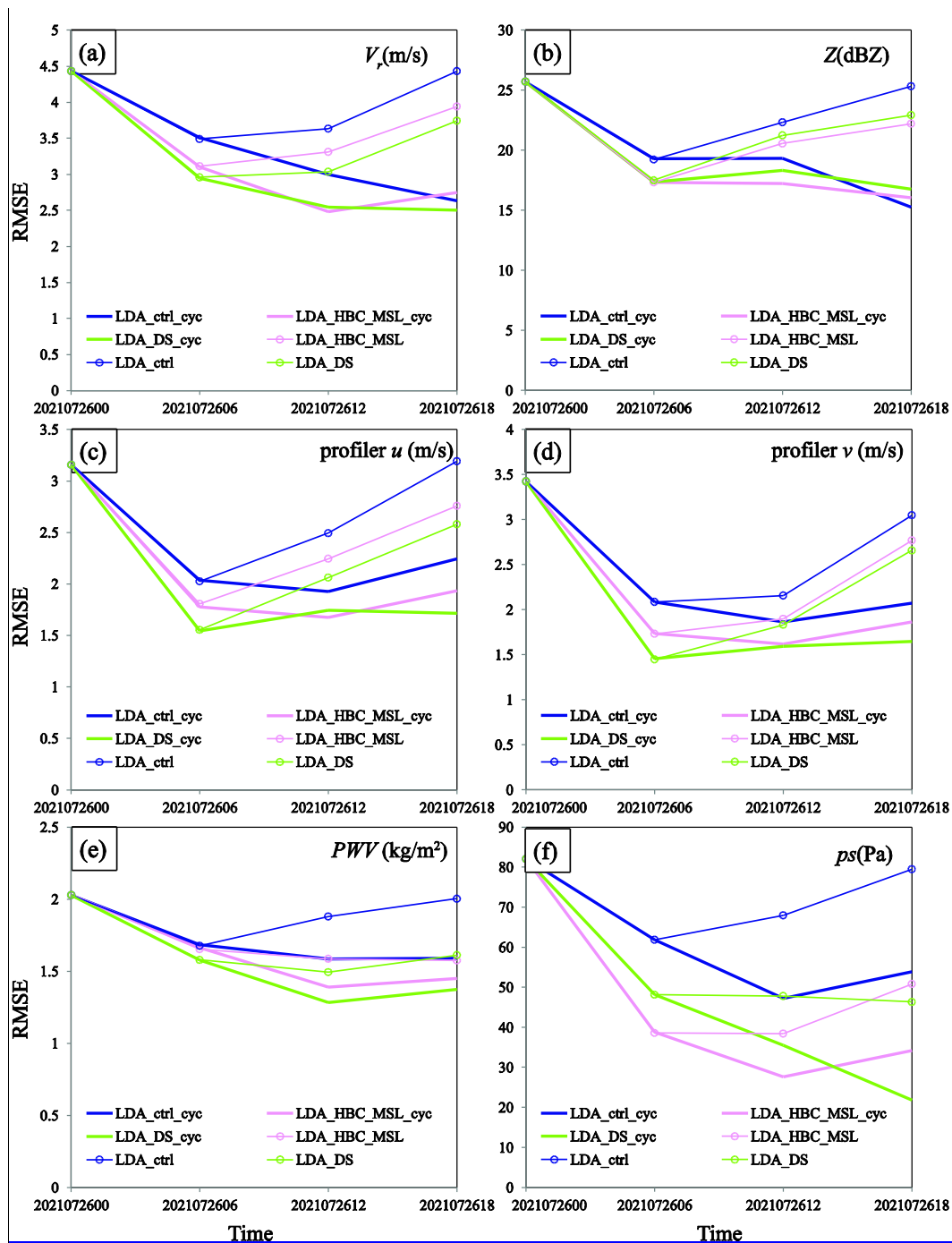


Figure 14 The evolutions of the forecast RMSE in terms of the (a) radial velocity, (b) reflectivity, (c) u component (wind profiler), (d) v component (wind profiler), (e) PWV , and (f) ps for LDA_ctrl_cyc (blue), LDA_HBC_MSL_cyc (magenta), and LDA_DS_cyc (green). The forecasts of LDA_ctrl, LDA_HBC_MSL, and LDA_DS are plotted for reference.

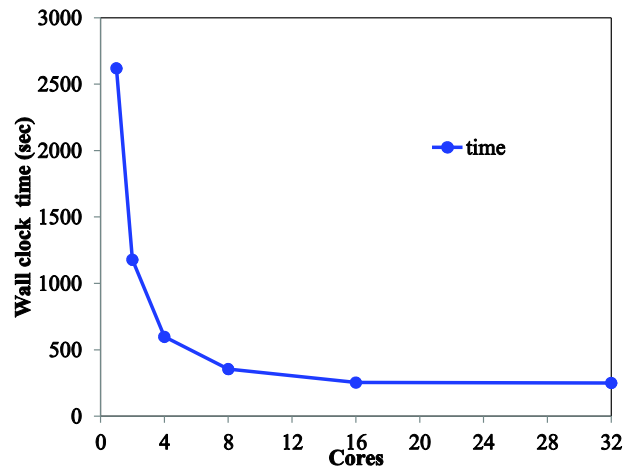


Figure-15- The ensemble spread (solid lines), RMSE (dotted lines), and correlation coefficient between spread and RMSE (dotted dash lines) in three scales for Ens_noFLTR (rectangle markers) and Hybrid_5band_DSL_6h (circle markers), where scales of 0 km-50 km, 50 km -200 km, and > 200 km are denoted by blue, orange, and light blue, respectively.

1455

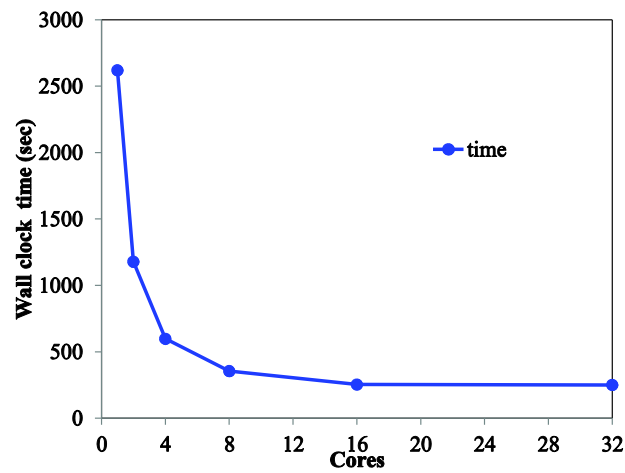


Figure 21 The wall clock time as a function of the number of cores used in the parallel test.

带精

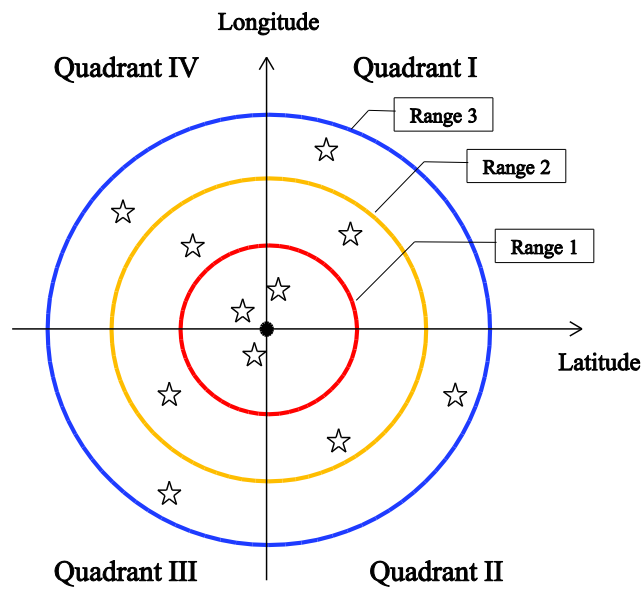


Figure A1 A schematic of the observation searching approach used in Local DA, where stars represent the selected observations near the grid point (dark solid dot) to be analyzed.

1485

1490